Untethered micro-robots integrated with stimuli-responsive hydrogel for sensing external environment

July 2021

Koki Yoshida

A Thesis for the Degree of Ph.D. in Engineering

Untethered micro-robots integrated with stimuli-responsive hydrogel for sensing external environment

July 2021

Graduate School of Science and Technology
Keio University

Koki Yoshida

Acknowledgment

As one of the founding members of the newly starting Onoe Laboratory at Keio University from spring 2014, it has been a truly remarkable journey beyond my best imagination. At the end of my brilliant years of graduate study from the beginning of the laboratory in an almost garage-like state, I feel really proud to see the well-established and productive laboratory where I can reflect many stories and memories at every single corner of it. Recalling all those wonderful days at Keio University, I first wish to express my deepest gratitude to Professor Hiroaki Onoe for everything we have done together. We together could achieve and keep doing a truly remarkable and unbelievable amount of works full of intellectual excitement and enjoyment. I have no doubt that our achievements and time would leave a long-lasting mark not only on me personally but also on the world.

I would like to all the wonderful collaborations, communications, and relationships that I had with the previous and current Onoe Group members. Daily works and interactions with the Onoe Group members have been an integral part of graduate study that tremendously helped me to grow as a better researcher, inventor, educator, and person. I wish to express special thanks to Shunsuke Nakajima and Ryo Sato for exciting collaboration on hydrogel microspring projects; Tomoki Hayashi and Shota Yamawaki for enjoyable collaboration on Marangoni swimmer with structural color hydrogel projects; Sergio Roberto Molina Ramirez for proofreading the journal paper; Shun Itai for working hard together as a colleague, a rival, and a friend.

I also wish to express my sincerest gratitude to all professors with whom I could numerous works beyond my expertise and learned so much. In particular, Professor Norihisa Miki at Keio University provide a clean room and other facilities for microfabrication; Professor Eiji Iwase at Waseda University lent a 3D printer for fabricating microfluidic device; Professor Ryuji Kawano at Tokyo University of Agriculture and Technology allowed me to explore applications of stimuli-responsive hydrogel; Associate Professor Tetsuo Kan at The University of Electro-Communications and Assistant Professor Mayu Muramatsu at Keio University gently taught me a finite element simulation; Associate Professor Kazuya

Ando at Keio University lent a Helmholtz coil; Professor Yoshitaka Kitamoto and Assistant Professor Yuta Kurashina at Tokyo Institute of Technology offered a useful discussion about a magnetic responsivity of hydrogel swimmer; Associate Professor Masahiro Takinoue kindly advised on my research.

In addition, I deeply appreciate many people in my student life. Professor Toshihiko Sugiura at Keio University was very helpful to me for my job hunting. The experience I had in Kumamoto as an engineer is an irreplaceable memory that I cannot experience in my student life. Professor Kenjiro Takemura at Keio University was always concerned about me, and his kindness encouraged me in my research. Associate professor Yuya Morimoto at Tokyo university advised me about not only the research but also the applications for awards and I could be honored with numerous awards thanks to his advice. Assistant professor Michinao Hashimoto at Singapore University of Technology and Design advised me about the research career, especially research overseas. Dr. Tomoya Koshi, Dr. Hiroki Yasuge, Dr. Kento Yamagishi, Dr. Chikahiro Imashiro, and all the senior researchers gave me advice and helped me grow as a researcher. I will continue to do my best to catch up with you.

I also greatly appreciate thesis committee members: Professor Toshihiko Sugiura, Professor Kenjiro Takemura, and Professor Norihisa Miki. Through the many opinions and discussions with thesis committee members, I was able to deepen my knowledge of my research.

My journey at Keio University could not be possible without generous supports from various funding agencies, shared facilities and managers, and mentors and services at Keio University. I wish to express my sincere thankfulness for generous support from the Japan Society for the promotion of science (JSPS) and Keio University.

Finally, I thank my family for their endless love and support. My father, my mother, and my older brother whose love, care, and life have been the greatest motivation, guidance, and energy throughout my entire Ph.D. and daily life. This dissertation may remark the last part of my graduate study at Keio University, but I am full of confidence and excitement as it will also remark the new beginning of my new grand journey.

Koki Yoshida

Abstract

Untethered micro-robots are sub-micron to centimeter scale robots without any physical restraint, and show great potential through sensing external environments for exploration of environments and in vivo treatment. However, there are many technical obstacles in an integration of conventional sensors, actuators, and processors into small-scale systems. Stimuli-responsive hydrogels, that can change their volume responding to external stimuli, are attractive candidates for novel components of micro-robots including actuators and sensors. In this research, two types of untethered micro-robots integrated with stimuli-responsive hydrogel were proposed for sensing the external environment. Specifically, by patterning stimuli-responsive hydrogels on the spiral-shaped microstructure, micro-robots with autonomous propulsion velocity control responding to the environmental temperature were realized. Furthermore, by integrating photonic colloidal crystal hydrogel into micro-robots, micro-robots that can convert external temperature or ethanol concentration into visible-light wavelength changes were achieved.

Chapter 1 describes the background and purpose of this research.

Chapter 2 describes the characteristics of stimuli-responsive hydrogel including cross-linking mechanism and volume change mechanism.

Chapter 3 theoretically analyzes the relationship between the geometry and the propulsion velocity based on the fluid dynamics. Then, the spiral-shaped micro-swimmers with different pitch angles were successfully fabricated by using buoyancy-assisted anisotropic gelation methods. Furthermore, it is experimentally confirmed that the propulsion velocity of these spiral-shaped micro-swimmers were able to controlled by the pitch angle change.

Chapter 4 describes the analysis of deformation behavior of micro-swimmers by the finite element simulation. It is revealed that the deformation behavior was changed by changing the pattern of hydrogel. Based on the simulation results, the propulsion velocity change was calculated.

Chapter 5 describes the autonomous propulsion velocity control of spiral-shaped micro-swimmer. The deformation of the micro-swimmer responding to the environmental temperature was succeeded. Furthermore, the acceleration and deceleration were also achieved.

Chapter 6 describes the micro-robots integrated with the photonic colloidal crystal hydrogel. The visible-light wavelength change responding to environmental temperature or ethanol concentration was achieved. Based on the results, it is showed that information about the external environment can be presented though the micro-robot.

Chapter 7 concludes this dissertation by discussing the impact of the proposed micro-robots integrated with stimuli-responsive hydrogel.

Table of Contents

Chapter 1
Introduction

1.1 Objectives in this dissertation

The objective of this dissertation is to develop untethered micro-robots integrated with stimuli-responsive hydrogel for detecting the external environment. Untethered micro-robots are sub-micron to centimeter-scale robotics without any physical restraint, and show great potential through detecting external environments for exploration of environments, and *In vivo* treatment. However, there are many technical obstacles in the integration into small-scale systems with conventional sensors, actuators, and processors. Stimuli-responsive hydrogels, that can change their volume responding to external stimuli, are attractive candidates for new components of micro-robots including actuators and sensors. In this research, two types of untethered micro-robots integrated with stimuli-responsive hydrogel were proposed for detecting the external environment. Specifically, by patterning stimuli-responsive hydrogels on the spiral-shaped microstructure, it is realized that a micro-robot can autonomously control its propulsion velocity according to the environmental temperature. Next, by integrating photonic colloidal crystal hydrogel into a micro-robot, it is achieved that a micro-robot can convert external temperature and ethanol concentration into visible-light wavelength changes.

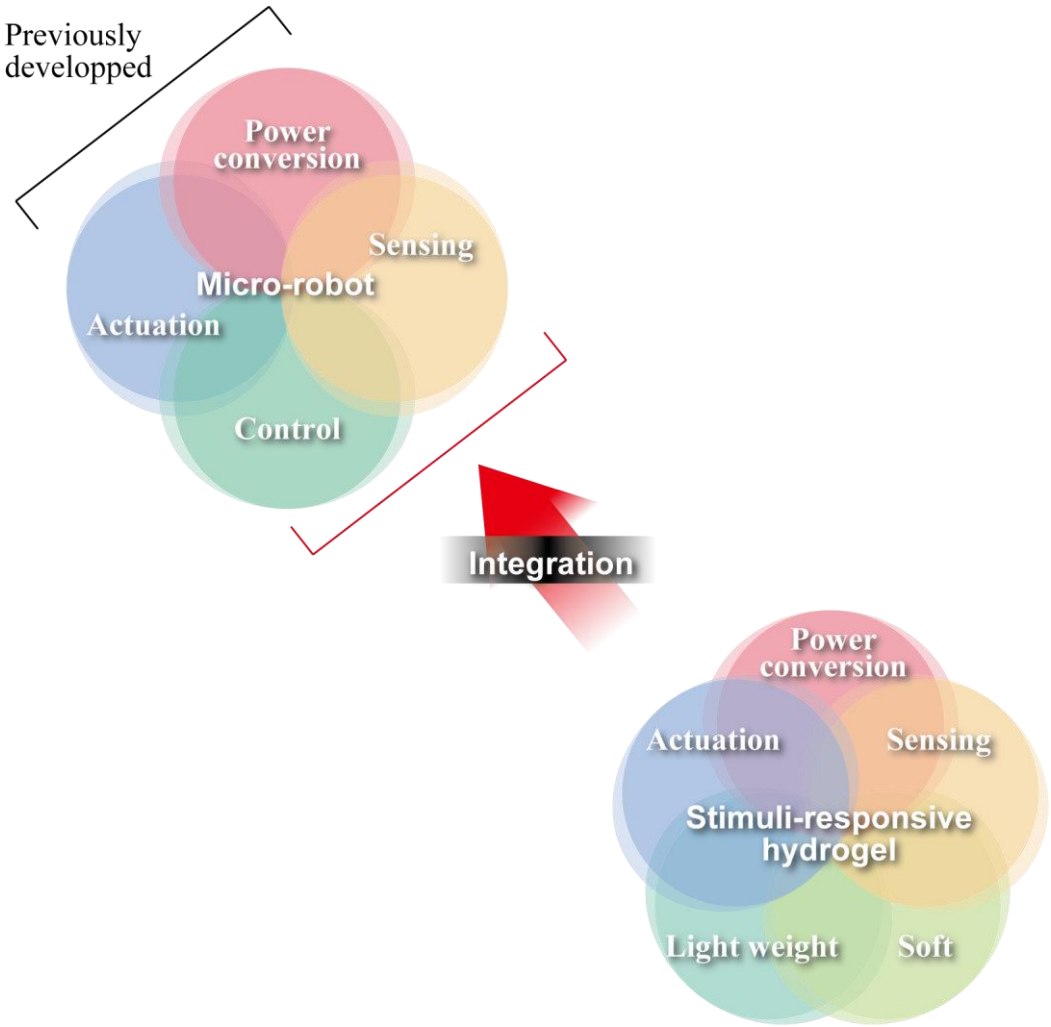

Figure 1.1 Features of micro-robots and stimuli-responsive hydrogels

1.2 Overview of micro-robots

Robotics is a device or a machine that autonomously performs some task in place of a person, and it has long been actively researched to improve the quality of people's daily lives, and in recent years, new academic fields have emerged across various research areas[1], such as soft robots[2][3][4], micro-robots[5][6][7], bio-inspired robots[8][9], and bio-hybrid

robots[10][11][12]. In particular, with the emergence of Micro Electro Mechanical Systems (MEMS) technology including photolithography since 1967[13][14], research on micro-robots is attracting attention as a next-generation technology. Micro-robots are sub-micron to centimeter-scale robotics (< 50 mm length), and show great potential in applications such as exploration of environments[1] and *In vivo* treatment (Delivery, Surgery, Imaging, and Diagnosis)[15][16].

Power conversion, actuation, sensing, and control are key factors for realizing novel micro-robots[17] (Fig. 1.1). While these essential components must be fully integrated and embedded within their structure, it is difficult to construct complex components such as those of conventional large-scale robots on the micro-scale. As the first step in realizing micro-robots, micro-scale actuators for realizing these actuations have also been developed. For example, piezoelectric actuators have widely been developed for insect-inspired legs[18], cockroach-inspired legs[19], honey bee-inspired flapping wings [20], and fish-inspired fin[21]. Moreover, a pneumatic actuator for spider-inspired robot[22] and a double-layered cantilever actuator for water strider-inspired legs[23] have also been reported. Because of the low force and power density of most micro-actuators, previous micro-robots often required a tethered connection to support pneumatic or electrical sources. A wire of micro-robots is limited to a maneuverable area, thus actuation without any wire is required as the next step toward the realization of micro-robots.

1.3 Untethered micro-robots

1.3.1 Achievement of previous untethered micro-robots

For realizing untethered micro-robots, numerous strategies have been proposed from the perspective of actuation and power conversion. Regarding the actuation, the achievements were mainly focused on developing efficient actuators and driving methods. The developments were divided into three categories; (I-i) actuators driven by less energy, (I-ii) propulsion system through surrounding environments, and (I-iii) bio-hybrid actuator.

Regarding the power conversion, two main methods were developed; (II-i) energy

Table 1.1 Summary of previous micro-robots

	Category	Energy source	Scale [mm]	Weight [mg]	Actuator
DEAnsect [24]	(I-i)	Battery	40	190	Dielectric elastomer actuator
Planar micro-robot [25]	(I-i)	Battery	30	~120	Vibration motor
Kilobot [26]	(I-i)	Battery	~20	N/A	Vibration motor
Marangoni propulsion micro-robot [29]	(I-ii)	Alcohol	15	N/A	None
Tissue-engineered jellyfish [31]	(I-iii)	(Electric fields)	10	N/A	Medusoid muscle
Tissue-engineered ray [32]	(I-iii)	(Optical stimulation)	16.3	~10.18	Rat cardiomyocytes
Sperm-flagella driven robot [33]	(I-iii)	(Magnetic fields)	50 $\times 10^{-3}$	N/A	Sperm-flagella
Robeetle [17]	(II-i)	Catalysis/Methanol	15	88	Shape-memory ally
Octobot [34]	(II-i)	Catalysis/H_2O_2	~30	N/A	Pneumatic actuator
Silicon robot[36]	(II-ii)	Solar cell	8.5	10	Piezoelectric actuator
Harvard Ambulatory Microrobot [15]	(II-ii)	Solar cell	44	1270	Piezoelectric actuator
Robofly [37]	(II-ii)	Solar cell	~20	190	Piezoelectric actuator
Microscopic robot [6]	(II-ii)	Laser	40-70 $\times 10^{-3}$	N/A	Surface electrochemical actuators
Helical swimmer [39]	(II-ii)	Magnetic fields	Sub μm	N/A	None
Soft film-shaped robots [42]	(II-ii)	Magnetic fields	3.7	N/A	None
Microflight [44]	(II-ii)	Magnetic fields	2.5	3.5	None
Gram-scale robot [45]	(II-ii)	Magnetic fields	~20	1090	Magnet actuator

N/A means the data is not available.

conversion system and (II-ii) remotely energy supply system. First, for enhancing the efficiency of power conversion, it is considered that extracting the energy from materials with high energy density. In addition, remote energy supply methods were developed for driving the micro-robots without integration with any batteries or energy storage. The achievements of untethered micro-robots were summarized in Table 1.1. Typical examples of previous untethered micro-robots were shown in Fig. 1.2.

(I-i) Actuators driven by less energy

Previous micro-robots often use a piezoelectric actuator, that required high voltage

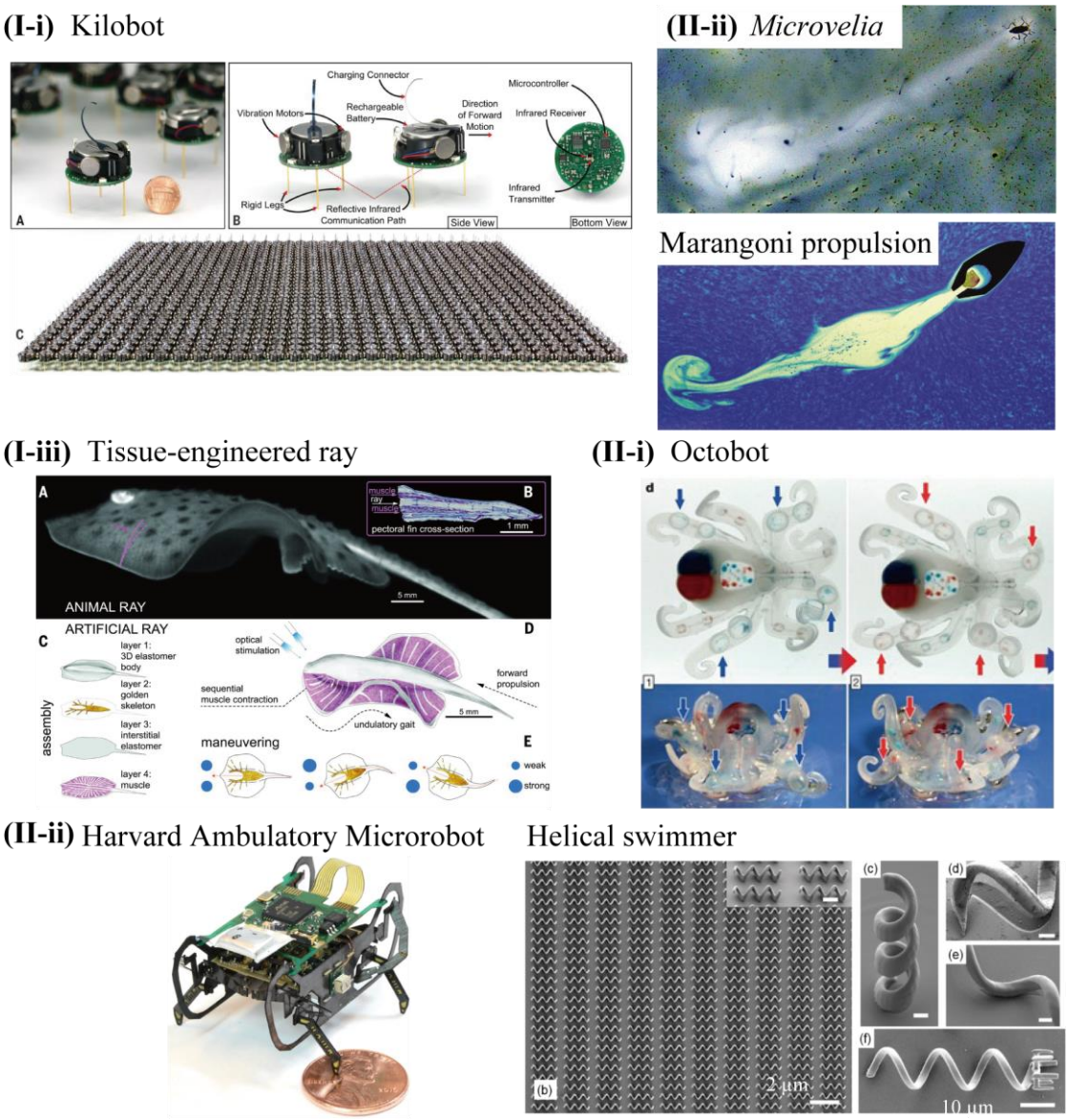

Figure 1.2 Typical examples of previous untethered micro-robots. (I-i) Actuators driven by less energy: Kilobot[26]. (I-ii) Propulsion system through surrounding environments: *Microvelia* (top) amd Marangoni propulsion micro-robot (bottom)[28]. (I-iii) Bio-hybrid actuators: Tissue-engineered ray[32]. (II-i) Enegy conversion system: Octobot[34]. (II-ii) Remotely energy supply: Harvard Ambulatory Microrobot[15] (left) and Helical swimmer[40] (right).(License numbers were summarized in Appendix G)

to drive. To decreasing the operating voltage, X. Ji and coworkers proposed a dielectric

elastomer actuator (DEA) that is driven below 500 V[24]. DEA consist of an elastomer sandwiched between two compliant electrodes and requires drive voltage. A nano-meter-thick stretchable conductive single-walled carbon nanotube (SWCNT) electrodes lead to the reduction of the driving voltage. For another example, P. Vartholomeos and E. Papadopoulos developed a planar micro-robot driven by two centripetal-force actuators[25]. The centripetal forces generated by vibration motors lead to the sliding motion of micro-robots. By using vibration motors for the sliding movement, M. Rubenstein and coworkers demonstrated programmable self-assembly of complex two-dimensional shapes with a thousand-robot swarm (Kilobot; Fig. 1.2 (I-i))[26].

(I-ii) Propulsion system through surrounding environments

There are attempts to drive micro-robots through natural phenomena such as the Marangoni effect[27]. The Marangoni effect is the mass transfer along with an interface between two fluids due to a gradient of the surface tension, and small insect such as *Microvelia* cleverly use this phenomenon to rapidly escape from the water surface to the ground (Fig. 1.2 (I-ii))[28][29]. Since the micro-robot can be driven only by the surface tension difference between the front and back of the micro-robot, the Marangoni propulsion is an attractive candidate for the simple driven method. And it also is expected to reduce the weight of the micro-robot and the size of the energy storage because Marangoni flow could be generated even with small amounts of chemicals. For driving energy, ethanol is widely used[30].

(I-iii) Bio-hybrid actuators

Biological systems such as living cells or micro-organisms are promising candidates to enhance robot ability including motility, energy conversion, and controllability. Several micro-robots driven by living cells have been developed through tissue engineering. For example, J.C. Nawroth and coworkers reported the construction of a freely swimming jellyfish from chemically dissociated rat tissue and silicone polymer[31]. Patterned neonatal rat cardiomyocytes contract synchronously when electric field stimulation is applied. In the bilayered design of the micro-robot, a flexible elastomer opposes an actuator, which promotes

asymmetric stroke patterns: active, fast contraction, and passive, slow recoil. For another example, S. Park and coworkers proposed a biohybrid micro-robot to swim and phototactically follow a light cue (Fig. 1.2 (I-iii))[32]. By patterning dissociated rat cardiomyocytes on an elastomeric body enclosing a micro-fabricated gold skeleton. Optical stimulation induced sequential muscle activation, leading to coordinated undulatory swimming. The speed and direction of the micro-robots were controlled by modulating light frequency and by independently eliciting right and left fins.

For an example of using living organisms, V. Magdanz and co-workers proposed a sperm-flagella-driven micro-bio-robot[33]. One advantage of using sperm cells for the micro-robot actuation is that these cells are readily available, easy to handle, do not need to be cultivated, and are completely harmless.

(II-i) Energy conversion system

The use of an energy source with high energy density was considered as a strategy to realize untethered micro-robots because conventional batteries at small scales are lower energy density than fat, fuels, or chemicals. Instead of the electric power supply, a method of extracting energy from chemicals such as methanol[17] and hydrogen peroxide[34] by catalytic reactions has been proposed. Catalytic reactions can produce driving sources such as heat or pneumatic pressure. X. Yang and coworkers developed an insect-scale micro-robot driven by a catalytic artificial muscle[17]. The catalytic artificial muscle is made by a wire composite with a NiTi shape-memory alloy (SMA) core and a platinum (Pt) shell, that acts as a catalyst. As the catalytic artificial muscle is exposed to the reactants, CH_3OH and O_2, it heats up and contracts due to the exothermic reaction caused by the Pt catalyst. When the supply of the reactant is stopped, the catalytic artificial muscle cools down and extends to its original length. Thus, the micro-robots can periodically drive by synchronously open and close the mechanical micro-valves that modulate the flow of reactants.

For another strategy of energy conversion, M. Wehner and coworkers developed pneumatic pressure-driven soft robots controlled through a microfluidic logic (Fig. 1.2 (II-i))[34][35]. The coupling of monopropellant fuels and microfluidic logic allowed to power,

control, and realize the autonomous operation of these pneumatically actuated systems. As the fuel decomposes in the presence of a platinum catalyst, the following reaction occurs $H_2O_2 \rightarrow 2H_2O + O_2$. This reaction results in volumetric expansion and thus the pneumatically actuated systems were driven.

(II-ii) Remotely energy supply

For remotely supplying energy, solar cells and magnetic fields are commonly used. S. Hollar and coworkers have proposed solar-powered micro-robots[36]. This solar-powered micro-robot has two, one degree-of-freedom leg and drags its tail end. The motion of micro-robot is generated via electrostatic inchworm motors driven by high voltage levels provided by solar cells. In addition, by using a piezoelectric actuator, a legged micro-robot (Fig. 1.2 (II-ii) left)[15] and flight micro-robots[37] have been developed. While the advantage of solar cells is that small electronics such as optical mouse sensors can be integrated, the miniaturization of micro-robots becomes increasingly difficult because the integration of various parts is more challenging.

For realizing hundred micrometer-scale robots, M. Miskin and coworkers have developed a new class of voltage-controllable electrochemical actuators that operate at low voltages (200 mV), low power (10 nW), and are completely compatible with silicon processing[6]. The actuators are made from nanometer-thick platinum and capping layer (graphene or titanium). When the actuator was biased relative to the surrounding aqueous electrolyte, ions adsorb/desorb from the platinum surface caused changing of the surface stress between the platinum and the capping layer, and then the actuator can be bent. The actuation can be accessed with lower applied voltages produced by photovoltaics and the behavior is highly reproducible.

Next, the use of magnetic fields for actuation is the most versatile option as this approach enables a wide variety of swimming mechanisms and can simultaneously be exploited for additional functionalities[38]. Moreover, magnetically actuated micro-robots are among the most promising miniaturized actuation systems for biomedical applications because they do not adversely interact with tissues in a wide range of conditions. For

magnetically driven micro-robots, bio-inspired systems, in particular the artificial bacterial flagella (ABFs), are widely developed, and these micro-robots mimic the helical propulsion of *E. coli* bacteria (Fig. 1.2 (II-ii) right)[39][40]. These micro-robots consist of magnetically response materials and propels themselves by rotational motion excited by magnetic fields. The magnetic force depends on the volume of the magnetic material, but a larger driving force can be generated by using a material with a larger magnetization. In a previous study, a micro-robot with a size of several microns was actually moved successfully[41], thus the magnetic field is effective as a driving source for small-scale micro-robots.

In addition to the helical propulsion, high mobility via multimodal locomotion could be realized through building magnetically driven micro-robots with soft and flexible materials such as elastomer or hydrogel[42][43]. W. Hu and coworkers have proposed magneto-elastic soft millimeter-scale robots that can swim inside and on the surface of liquids, climb liquid menisci, roll and walk on solid surfaces, jump over obstacles, and crawl within narrow tunnels[42]. Moreover, magnetic actuation is also applied for driving mechanical systems including rotational wings (micro-flight system)[44] and gram-scale robot legs[45].

1.3.2 Challenges of untethered micro-robots

As mentioned in this section, various strategies for realizing untethered micro-robots have been proposed. These strategies mainly focused on the actuation or the energy supply, and fewer examples of sensing external environments and control have been achieved. The ability to detect the external environment and act autonomously is important for the realization of untethered micro-robots (Autonomy in this study refers to the degree of human control required for the constructed robot). However, the integration of conventional sensors, actuators, and processors into these micro-robot systems is technically challenging. Therefore, it is necessary to develop new components and integration methods to overcome these challenges.

1.4 Micro-robots integrated stimuli-responsive hydrogel

1.4.1 Stimuli-responsive hydrogel

For new components of micro-robots, stimuli-responsive hydrogels are highly attractive candidates from both material and processing perspectives[46][47]. Stimuli-responsive hydrogels are cross-linked polymer networks with high water contents[48]. Stimuli-responsive hydrogels are soft and lightweight. In addition, the stimuli-responsive hydrogel has a stimuli-responsivity, and this feature enables to change their volume accordingly responding to the external stimuli (for example, temperature[49][50], light[51], pH[52], and chemical compounds[53][54][55]) without the need for additional actuators or sensors (Fig. 1.3 (a)). The volume change mechanism is independent on their scale because the volume change is caused by the interaction of the polymer network (for example, hydrophobic interaction). In fact, many micro-scale actuators[56][57] and bio-chemical sensors[58][59] have been developed through this function of the stimuli-responsive hydrogel.

From the viewpoint of processing, the stimuli-responsive hydrogel has characteristics that suitable for micro-scale processing. Stimuli-responsive hydrogels are obtained by cross-linking polymer chains. There are two main types of cross-linking mechanisms: physical cross-linking by intermolecular interactions such as hydrogen bonding and hydrophobic interactions[60][61], and chemical cross-linking by covalent bonding[62]. Physically cross-linked hydrogels are mainly fabricated through micro-fluidic devices because physically cross-linking often occurs instantaneously (Fig. 1.3 (b))[63][64][65]. Regarding the chemically cross-linking, many stimuli-responsive hydrogels can be cross-linked by photo-polymerization, that enables to fabricate of micro-scale hydrogel through photolithography (Fig. 1.3 (c))[66].

These features enable a significant reduction in the size and complexity of resulting micro-robot components. Therefore, the stimuli-responsive hydrogel is expected to integrate into untethered micro-robots as actuators and sensors.

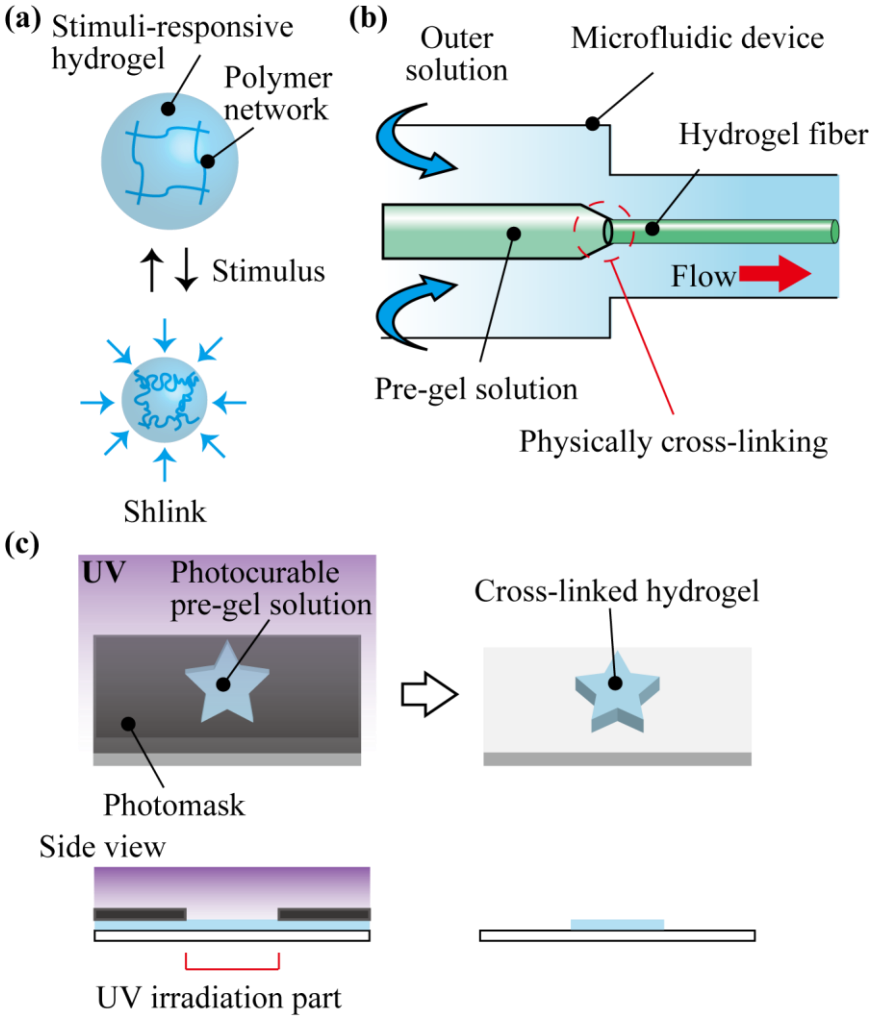

Figure 1.3 Stimuli-responsive hydrogel. (a) Volume change. (b) Micro-fluidic device. (c) Photolithography.

1.4.2 Micro-robots integrated with stimuli-responsive hydrogel

There are several examples of micro-robots integrated with stimuli-responsive hydrogel[9][67]. For example, B. Xu et al. have proposed a system that integrates a propulsion mechanism using cardiac muscle and a propulsion control using stimuli-responsive hydrogel[67]. The soft robot is propelled using a muscular tail fin that emulates the swimming of whales and works as a cellular engine powered by the synchronized contraction of striated

cardiac micro-tissue structures. The tail fin could be transformed from a wide state to a retracted state optically triggered by the nIR laser for minimizing the propulsion force and thus the transition of state lead effectively switching off the propulsion.

1.4.3 Challenges of micro-robots integrated with stimuli-responsive hydrogel

Previous micro-robots integrated with stimuli-responsive hydrogel are mainly focused on the remote control, and only a simple control of two phase transition (propulsion and stationary states), has been achieved. However, there is still a grand challenge regarding the autonomy of micro-robots for applying to the exploration of environments and *In vivo* treatment. In particular, (i) autonomous propulsion control responding to the surrounding environment and (ii) autonomously converting the external information to usable information are required for enhancing the autonomy of micro-robots.

1.5 This work: Untethered micro-robots integrated stimuli-responsive hydrogel for sensing external environment

In this research, the novel integration strategies to realize untethered micro-robots integrated with stimuli-responsive hydrogel for autonomously sensing the external environments were proposed. In particular, (i) a spiral-shaped micro-swimmer with autonomous propulsion velocity control by detecting surrounding temperature and (ii) a micro-robot integrated with photonic colloidal crystal hydrogel for converting the temperature and ethanol concentration into visible-light wavelength change were realized.

First, I propose the spiral-shaped micro-swimmer for autonomous propulsion velocity control by detecting surrounding temperature (Fig. 1.4 (a)). The propulsion velocity of spiral-shaped micro-swimmers is largely depending on the pitch angle, thus it is expected that the propulsion velocity can be controlled by the pitch angle change. To realize the pitch angle change, the stimuli-responsive hydrogel is patterned into the spiral-shaped micro-

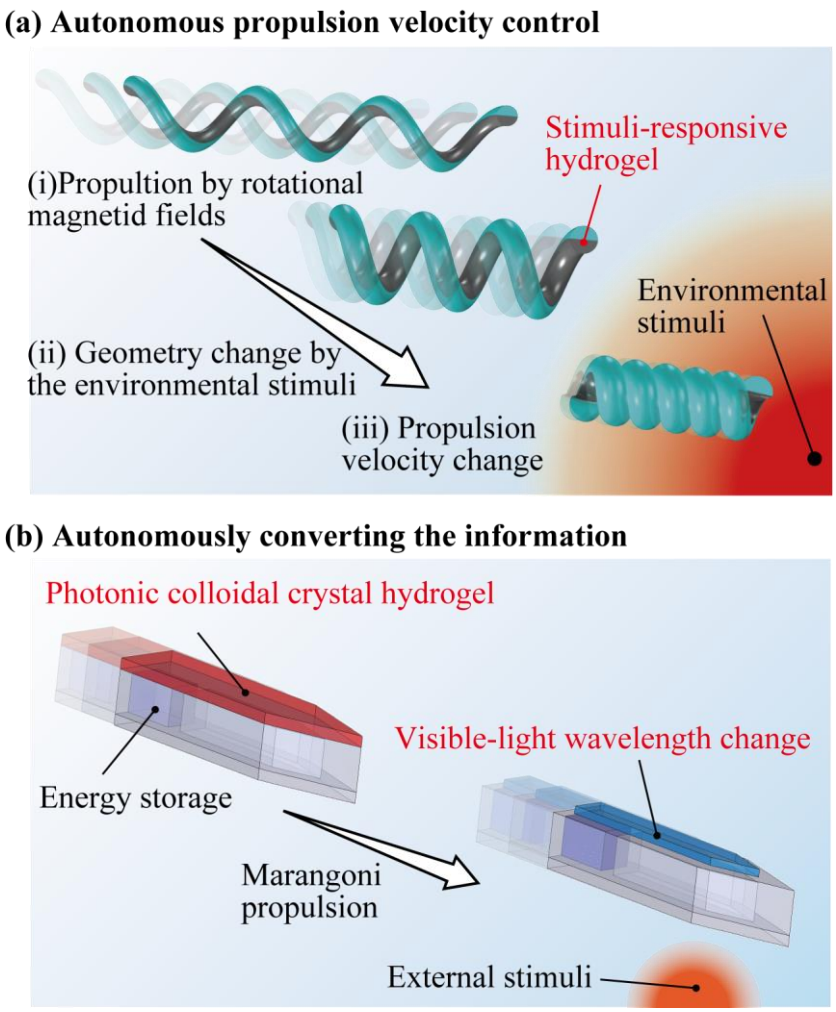

Figure 1.4 Proposed untethered micro-robots integrated with stimuli-responsive hydrogel. (a) Spiral-shaped micro-swimmer for autonomous propulsion velocity control. (b) Micro-robots integrated with photonic colloidal crystal hydrogel for converting the environmental stimuli into the visible-light wavelength change.

swimmer. The relationship between the patterning and the deformation behavior is analyzed through a finite element simulation. Based on the simulation results, the acceleration and deceleration of spiral-shaped micro-swimmers are achieved.

Next, I proposed the micro-robot integrated with photonic colloidal crystal hydrogel for converting the temperature and ethanol concentration into visible-light wavelength change (Fig. 1.4 (b)). In this dissertation, two brief concepts of micro-robot integrated with

photonic colloidal crystal hydrogel were proposed: a tubular-shaped micro-robot and a rocket-shaped micro-robot. These micro-robots have ethanol storage that enables them to propel by the Marangoni effect. By using a thermal-responsive hydrogel and an ethanol-responsive hydrogel, the information of temperature and ethanol concentration was successfully converted to the visible color sifting.

1.6 Dissertation outline

Chapter 1 describes the background and purpose of this research (Fig. 1.5).

Chapter 2 describes the characteristics of stimuli-responsive hydrogel including cross-linking mechanism and volume change mechanism.

Chapter 3 describes the relationship between the geometry and the propulsion velocity was theoretically analyzed based on the fluid dynamics. Then, the spiral-shaped micro-swimmer with different pitch angles was successfully fabricated by using buoyancy-assisted anisotropic gelation methods. Furthermore, it is experimentally confirmed that the propulsion velocity of these spiral-shaped micro-robots could be controlled by the pitch angle change.

Chapter 4 describes an analysis of deformation behavior through a finite element simulation. It is revealed that the deformation behavior was changed by changing the pattern. Based on the simulation results, the propulsion velocity change was analyzed.

Chapter 5 describes the autonomous propulsion velocity control of spiral-shaped micro-swimmer. The deformation of the micro-swimmer responding to the environmental temperature was succeeded. Furthermore, acceleration and deceleration were also achieved.

Chapter 6 describes the micro-robots integrated with the photonic colloidal crystal hydrogel. The visible color change responding to environmental temperature and ethanol concentration was achieved. Based on the results, it is showed that information about the external environment can be presented through the micro-robot.

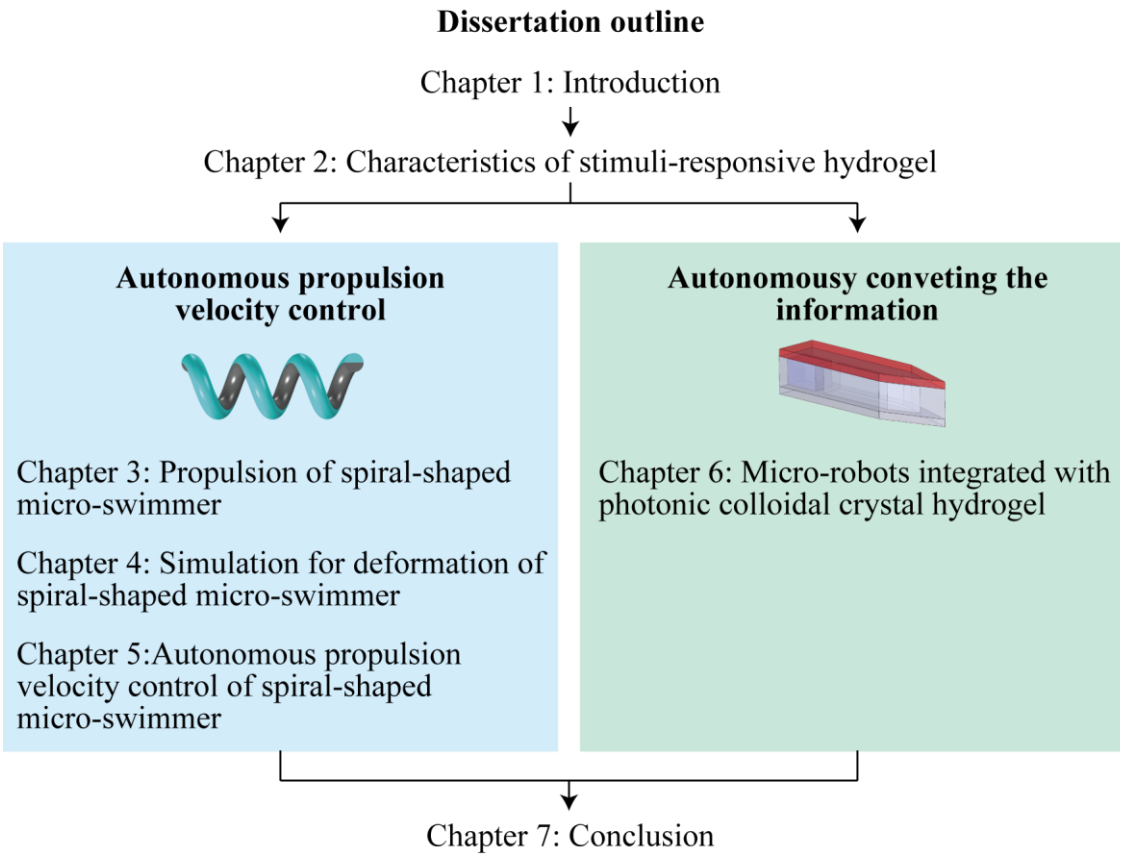

Figure 1.5 Outline of the dissertation.

Chapter 7 concludes this dissertation by discussing the impact of the proposed micro-robots integrated with stimuli-responsive hydrogel.

Chapter 2
Characteristics of hydrogel

2.1 Introduction

In this chapter, the characteristics of the hydrogel are described. First, the gelation mechanisms were introduced because these mechanisms are important for fabricating the micro-robots integrated with stimuli-responsive hydrogel. In this dissertation, two types of cross-linking mechanisms were used: physically cross-linking for rapid gelation and chemical cross-linking for bonding to an elastomer. Then, the typical mechanism of stimuli-responsiveness was introduced. Finally, the response speed of stimuli-responsive hydrogel was discussed.

2.2 Gelation mechanisms

Hydrogels are obtained by cross-linking polymer chains. There are two main types of cross-linking mechanisms: physical cross-linking by intermolecular interactions such as hydrogen bonding and hydrophobic interactions[60][61], and chemical cross-linking by covalent bonding[62]. For fabricating three-dimensional hydrogel structures, common processing methods such as machining and rolling cannot be used because hydrogels are brittle materials. Therefore, various research on forming hydrogels into various three-dimensional structures have been developed[68].

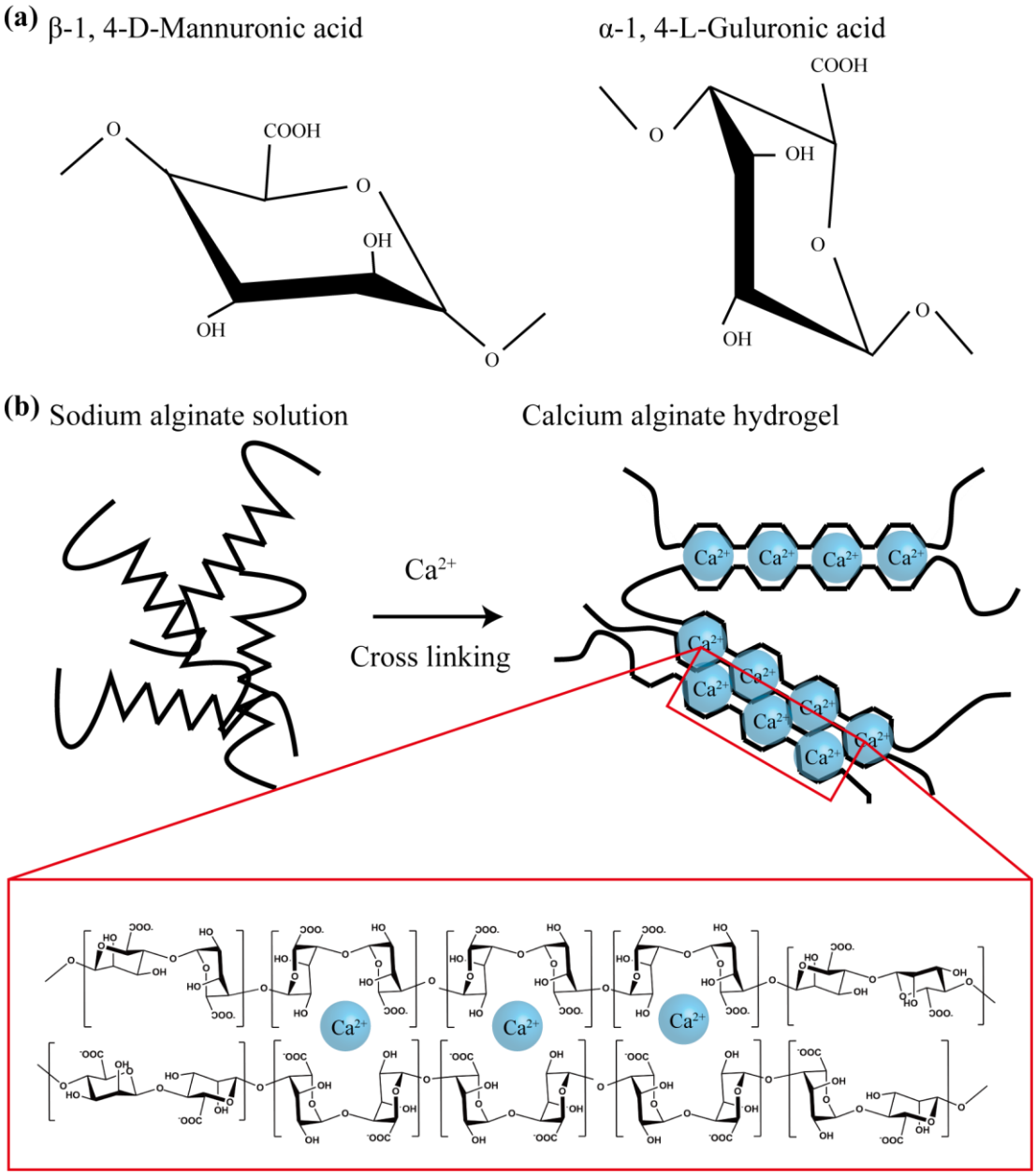

Figure 2.1 Gelation mechanism of calcium alginate hydrogel. (a) Mannuronic acid and glucuronic acid. (b) Schematic image of physically cross-linking.

2.2.1 Physically cross-linked hydrogel

First, calcium alginate hydrogel, which is used for spiral-shaped micro-swimmer, is described. Sodium alginate is a polymer of β-1,4-D-mannuronic acid (Man.) and α-1,4-L-

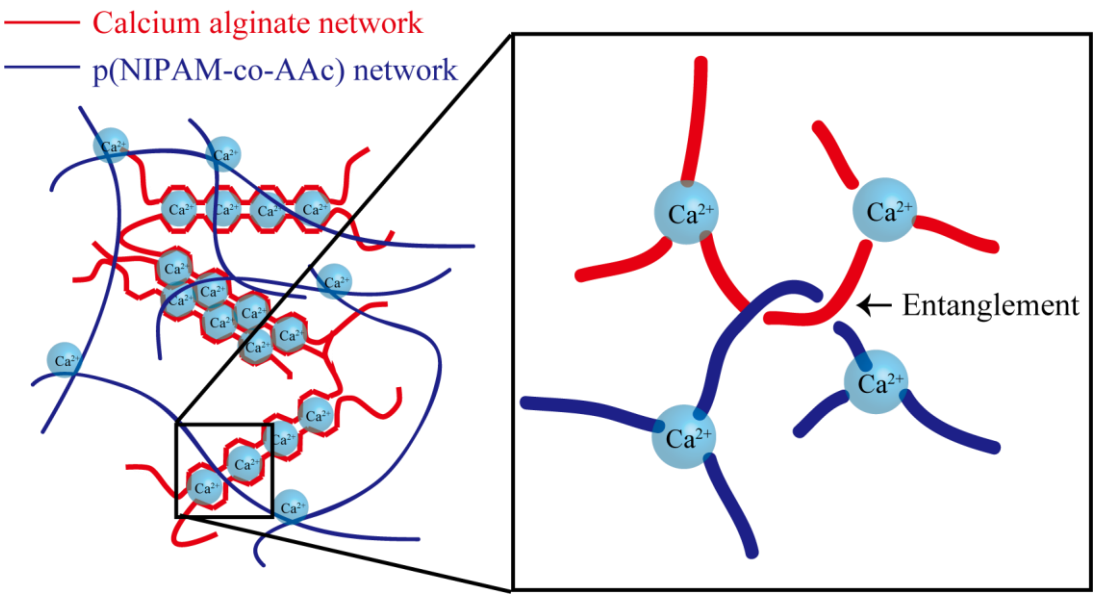

Figure 2.2 Double network of calcium alginate hydrogel and NIPAm-co-AAc.

glucuronic acid (Glu.) (Fig. 2.1 (a))[60][61]. Man. and Glu. have different steric structures and they are randomly bonded together to form linear polymers. The molecular chains of Glu. Glu. blocks are bent due to the repulsion of carboxy groups, and ionic bonding occurs when divalent cations such as calcium ions enter between the chains (Fig. 2.1 (b)). This ionic cross-linking occurs instantaneously between multiple sodium alginate chains. By taking advantage of their instantaneous polymerization, various methods to fabricate various shapes of calcium alginate hydrogels with microfluidic devices have been reported.

In addition, a poly(N-isopropylacrylamide-co-acrylic acid) (NIPAm-co-AAC) was used for the thermal stimuli-responsive hydrogel for spiral-shaped micro-swimmer. The chemical formula is $(C_6H_{11}NO)m(C_3H_4O_2)n$. NIPAm-co-AAc is constructed by modifying an acrylic acid to the end of pNIPAM. NIPAm has an amide group as hydrophilic and an isopropyl group as hydrophobic. The acrylic acid has a carboxyl group, that forms ionic bonds with divalent calcium ions to form cross-linked points of the hydrogel.

Sodium alginate and p(NIPAM-co-AAc) are both cross-linked by Ca^{2+}. The sodium alginate can rapidly gelation when ejected into the calcium chloride solution and this properties enable the gelation with keeping its shape during gelation. On the other hand. the

gelation speed of p(NIPAM-co-AAc) by Ca^{2+} cross-linking is slow, so the pre-gel solution of p(NIPAM-co-AAc) cannot keep its original shape when it is ejected in Calcium chloride solution. Therefore, mixing the NIPAm-co-AAc with the sodium alginate allows them to maintain their shape during the gelation. At this time, it is estimated that the polymer network of p(NIPAM-co-AAc) is trapped by the polymer network of calcium alginate hydrogel (Fig. 2.2). In addition, the networks of each hydrogel are entangled and it is supposed that the composite hydrogel also has temperature responsiveness.

2.2.2 Chemical cross-linked hydrogel

An adhesion between hydrogel and elastomer is too weak because of the existence of water. Thus, bonding hydrogel is one of the major challenges, and various methods to bonding hydrogel and various surfaces have been widely explored[69]. In this research, I used a combination of chemically cross-linked hydrogels and a benzophenone for bonding the hydrogel and the elastomer with covalently cross-linking[70][71].

First, it is described that a typical chemically cross-linked hydrogel poly (*N*-isopropylacrylamide) (pNIPAm). pNIPAm hydrogels that fabricated by cross-linking an acrylic monomer *N*-isopropylacrylamide. Acrylic monomers are low-molecular compounds with vinyl groups that related to the polymerization, and they could be mainly polymerized by radical reactions. Radical polymerization proceeds by three steps: initiation, propagation, and termination process (Fig. 2.3). For radical polymerization, a photoinitiator and a cross-linking agent are used in addition to the monomer. Because the radicals generated from the photoinitiator by UV irradiation are highly reactive, radicals are quickly transferred to monomers and produce the radical initiator for radical polymerization (Initiation process, Fig. 2.3 (a)). The generated radical initiator causes a rapid and continuous radical addition reaction to the double-bonded part of the vinyl group of another monomer or cross-linking agent (Propagation process, Fig. 2.2 (b)). This propagation reaction proceeds repeatedly until the termination reaction occurs, and a polymer with high molecular weight is obtained at once. The polymer chain can be cross-linked to create a polymer network structure by copolymerizing a divinyl compound with two vinyl groups during polymerization (Fig. 2.3

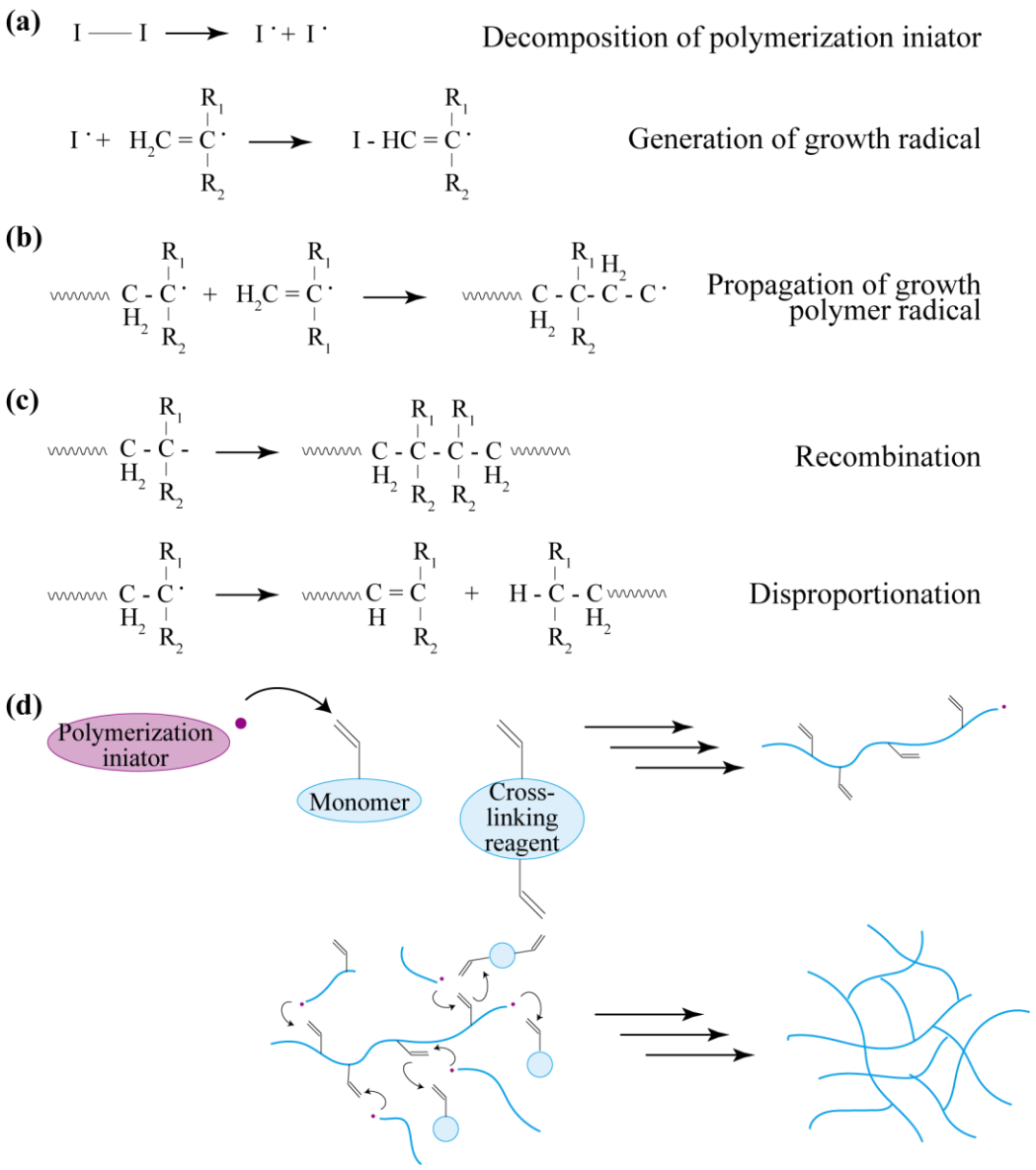

Figure 2.3 Cross-linking process: (a) Initiation, (b) propagation, and (c) termination process. (d) Schematic image of cross-linking.

(c), (d)).

2.3 Bonding hydrogel and elastomer surface

The hydrogel highly contains water, and water inhibits the adhesion to various

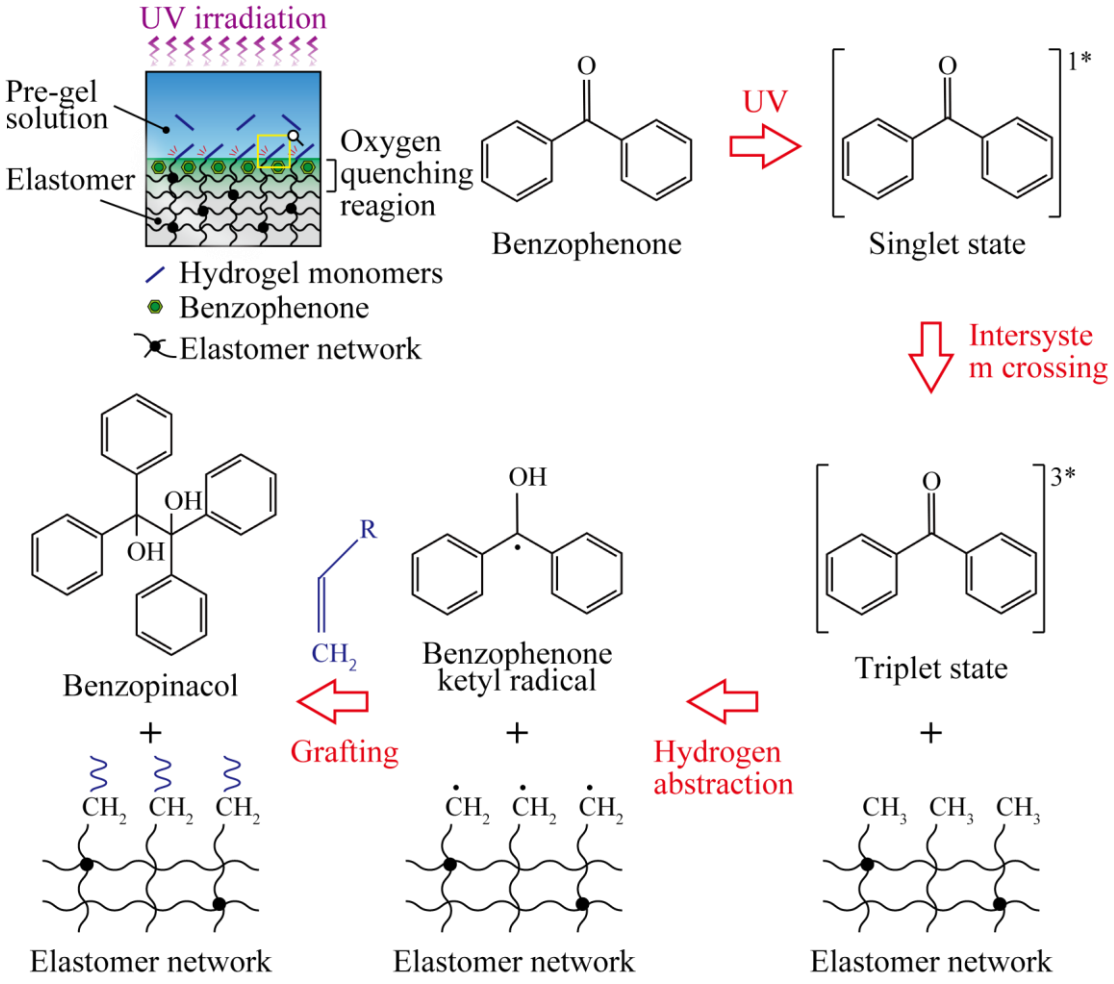

Figure 2.4 Benzophenone chemistry.

surfaces including elastomers. Previously, the bonding of hydrogel to rigid solids (for example, glass, ceramics, and metals) have been achieved by covalently crosslinking with modifying the solid surface through a silane coupling[69]. However, this method generally could not be used for bonding hydrogels and elastomers, mainly due to two challenges: First, elastomers are highly permeable to oxygen that leads to the oxygen inhibition effect by which the free-radical polymerization or surface covalent crosslinking of the hydrogel are seriously inhibited[72]. Second, the aging or hydrophobic recovery of functionalized elastomer surfaces also significantly lower the effectiveness of hydrogel bonding on elastomers[73]. To overcome these challenges, a modification of cured elastomer surfaces with benzophenone to alleviate oxygen inhibition effect and active elastomer surfaces for hydrogel polymer grafting have

been proposed[71].

Here, benzophenone chemistry for hydrogel bonding (Fig. 2.4) was described. The benzophenone in ethanol solution was treated to the elastomer surfaces via swelling-driven surface absorption of benzophenone solution[70]. The benzophenone absorbed in the surface is excited by UV irradiation into a singlet state which is followed by conversion into a triplet state through the intersystem crossing. The triplet-state benzophenone consecutively changes into benzophenone ketyl radical by abstracting hydrogen from surrounding unreactive C-H bonds in elastomer polymer. Finally, the benzophenone ketyl radical mediates the grafting of polymer networks of the hydrogel onto the reactive sites on the elastomer surface, generating benzopinacol as a final reaction product.

2.4 Stimuli-responsive behavior

Among the properties of the hydrogel, stimuli-responsiveness has been widely applied to sensors[58][59] and actuators[56][57]. Hydrogel's polymeric chains produce volume changes in response to external stimuli such as temperature[49][50], pH[52], light[51], and chemical compounds (ex. glucose[53], acetone[54], alcohol[55]). Here, it is introduced in detail the volumetric change mechanism of temperature-responsive hydrogels (pNIAPm), which is mainly used in this research. The swelling and contraction behavior is due to the changing the interaction between the polymer chains and a solvent in response to temperature changes[49]. The pNIPAm hydrogel has a lower critical solution temperature (LCST) around 33ºC. The pNIPAm hydrogel absorbs a large amount of water and swells greatly at low temperatures (< LCST 33ºC). In contrast, the pNIPAm hydrogel largely shrinks around the LCST at high temperatures (> LCST 33ºC). The pNIPAm hydrogel has a hydrophilic amide group and a hydrophobic isopropyl group, and methylene and methane groups in the main chain of the polymer chain are also hydrophobic. At low temperatures (< LCST 33ºC), the hydrophilic amide groups interact strongly with water by hydrogen bonding, and each chain is surrounding by water. The pNIPAm hydrogel absorb a large amount of water and largely swells due to the strong interaction between water and the polymer chains (Fig. 2.5 (a)). This

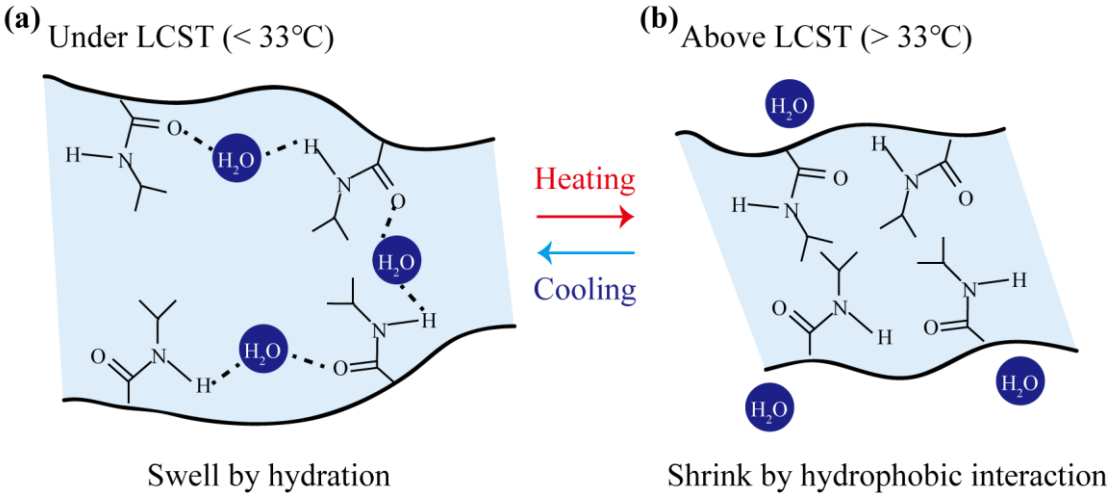

Figure 2.5 Mechanism of volume change: (a) Swelling state and (b)Shrinking state.

phenomenon is called hydration. On the other hand, the hydrogel bonds that drive hydration are thermally week, and the hydrogen bonds between the amide group and the water weaken by increasing temperature. Thus, when the temperature increases, the water leaves the polymer chain. The hydrophobic isopropyl group tends to gather with each other in water due to their low affinity for water. When the effect of aggregation due to the interaction of hydrophobic isopropyl groups exceeds the effect of reduced hydration by temperature increasing (> LCST 33ºC), the entire polymer chain aggregates. As a result, the pNIPAm hydrogels shrink with releasing the water (Fig. 2.5 (b)). In other words, temperature responsiveness is a balance between hydration and the hydrophobic interaction.

2.5 Dynamics for swelling and shrinking of hydrogel

2.5.1 Definition of symbols

The symbols mainly used in this section are as follows.

Z	Free energy density [J/m^3]
λ_α	Elongation of hydrogel in the α direction [-]
G	Shear modulus of hydrogel [-]
φ	Volume fraction of polymer [-]

T	Temperature [K]
k_B	Boltzmann's constant [J / K]
v_c	Volume of polymer segment [m^3]
χ	Kai Parameter [-]
Π	Osmotic pressure of polymer [Pa]
σ_{aa}	Osmotic stress [N]
K	Osmotic modulus [-]
ω	Volumetric strain of mesh [-]
ε	Strain tensor of mesh [-]
p	Pressure of solvent [Pa]
a	Average distance from the surface to the inside of the gel [m]

2.5.2 Dynamics

Since the hydrogel is an elastic material containing solvent, the swelling, and shrinking of the hydrogel involves simultaneous deformation of the hydrogel and flow of the solvent.[74]. An example of where the deformation of an object and the flow of a solvent occur simultaneously is in squeezing fruit to produce juice. In these phenomena, plastic deformation and structural failure are often caused in many materials. In the case of hydrogels, these effects are small, so the hydrogel is considered to be a complete miscible system of elastic material and solvent. Therefore, the continuum theory is used to describe the coupling between the deformation of the hydrogel and the flow of the solvent.

Free energy of hydrogel

The free energy density of the hydrogel, $f_{gel}(\lambda_x, \lambda_y, \lambda_z)$, can be determined theoretically from experiments or molecular models, and neutral hydrogels can be described as

$$f_{gel}(\lambda_\alpha) = \frac{G_0}{2}\left(\lambda_x^2 + \lambda_y^2 + \lambda_z^2 - 3\right) + \frac{\varphi}{\varphi_0} f_{sol}(\varphi) \tag{2.1}$$

where G_0 is the shear modulus of hydrogel in reference state and $f_{sol}(\varphi)$ is the free energy of

polymer solution with concentration φ. By using the lattice model, the free energy of solvent is described as

$$f_{sol}(\varphi) = \frac{k_B T}{v_c}[(1-\varphi)l_n(1-\varphi) + \chi\varphi(1-\varphi)]. \quad (2.2)$$

Expansion balance

Since the hydrogel is isotropically deformed, the elongation of each axis is equal ($\lambda_x = \lambda_y = \lambda_z = (\varphi_0 / \varphi)^{1/3}$). The equation (2.1) can be written as

$$f_{gel} = \frac{3G_0}{2}\left[\left(\frac{\varphi}{\varphi}\right)^{\frac{2}{3}} - 1\right] + \frac{\varphi_0}{\varphi} f_{sol}(\varphi). \quad (2.3)$$

The equilibrium state φ is determined by the condition that $f_{gel}(\varphi)$ is minimized from $\partial f_{gel}/\partial\varphi = 0$. By using this condition can be described by using equation (2.3)as

$$G_0\left(\frac{\varphi_0}{\varphi}\right)^{\frac{1}{3}} = \Pi_{sol}(\varphi) \quad (2.4)$$

where $\Pi_{sol}(\varphi) = \partial f_{sol} / \partial\varphi - f_{sol}$ is the osmotic pressure of polymer solution with concentration φ. This equation indicates that the equilibrium state of the hydrogel is determined by the balance between the osmotic pressure that causes the solvent to soak into the hydrogel and expand the volume of the hydrogel, and the elastic force of the polymer chain that prevents the volume expansion.

Osmotic stress

When the hydrogel is stretched, the force acts on the sides of the hydrogel. The force per unit area acting on the surface perpendicular to the x-axis is

$$\sigma_{xx} = \frac{1}{\lambda_y \lambda_z}\frac{\partial f_{gel}}{\partial \lambda_x}, \quad (2.5)$$

and this is called osmotic stress. The osmotic stress is a tensor quantity and can be calculated from the free energy density of the hydrogel. If the deformation of the hydrogel is large, it becomes complicated, so it is referred to as micro-scale deformation below.

Elastic free energy at micro-scale deformation

It is supposed that a point of the hydrogel mesh at position ***r*** in the reference state is moved to ***r*** + ***v*** (***r***) by deformation. When ***v*** (***r***) is small, the free energy density of hydrogel is

$$f_{gel} = \frac{1}{2}K\omega^2 + G\sum_{\alpha\beta}\left(\varepsilon_{\alpha\beta} - \frac{1}{3}\omega\delta_{\alpha\beta}\right)^2, \tag{2.6}$$

where K is an osmotic modulus, G is shear modulus, ω is the volumetric strain of mesh, and $\varepsilon_{\alpha\beta}$ is strain tensor of mesh. Moreover, ω is

$$\omega = \sum_{\alpha}\frac{\partial u_\alpha}{\partial r_\alpha} = \nabla \cdot u, \tag{2.7}$$

and $\varepsilon_{\alpha\beta}$ is

$$\varepsilon_{\alpha\beta} = \frac{1}{2}\left(\frac{\partial u_\alpha}{\partial r_\beta} + \frac{\partial u_\beta}{\partial r_\alpha}\right). \tag{2.8}$$

For the free energy in equation (2.6), the osmotic stress is

$$\sigma_{\alpha\beta} = K\omega\delta_{\alpha\beta} + 2G\left(\varepsilon_{\alpha\beta} - \frac{1}{3}\omega\delta_{\alpha\beta}\right). \tag{2.9}$$

If the hydrogel is in the equilibrium state, the osmotic stresses are balanced, so

$$\sum_{\beta}\frac{\partial\sigma_{\alpha\beta}}{\partial r_\beta} = 0 \tag{2.10}$$

is valid. Therefore, the equilibrium state of the hydrogel can be obtained by solving equations (2.9) and (2.10).

2.5.3 Governing equation of hydrogel dynamics

Stress and Osmotic stress

Since the volume modulus of the solvent, K_{sol}, is usually much larger than the osmotic modulus, K, it is assumed that the solvent is incompressible ($K_{sol} = \infty$). In addition to the osmotic stress, the solvent pressure contributes to the force acting in the hydrogel as

$$\sigma_{\alpha\beta}^{tot} = \sigma_{\alpha\beta} - p\delta_{\alpha\beta}, \tag{2.11}$$

where p is the pressure of the solvent. In small deformations that the effect of inertia is negligible, the stresses are always balanced as

$$\sum_{\beta} \frac{\partial}{\partial r_{\beta}} \left(\sigma_{\alpha\beta} - p\delta_{\alpha\beta}\right) = 0. \tag{2.12}$$

Pressure and flow of solvent

If the pressure of the solvent in the hydrogel is not constant, the solvent will flow from high pressure to low pressure. The relative velocity of the solvent to the mesh of the hydrogel, $\boldsymbol{v}_{\mathbf{rel}}$, is proportional to the pressure gradient and described as

$$\boldsymbol{v_{rel}} = -\bar{\kappa}\nabla p, \tag{2.13}$$

that called Darcy's low. The velocity of the hydrogel mesh at location r is obtained by $\dot{\boldsymbol{u}}(\boldsymbol{r}, t) = \partial \boldsymbol{u}(\boldsymbol{r}, t) = \partial t$. By defining the velocity of solvent is $\boldsymbol{v}_s(\boldsymbol{r})$, the equation (2.13) is

$$\boldsymbol{v_s} - \boldsymbol{v} = \dot{-}\tilde{\kappa}\nabla p. \tag{2.14}$$

On the other hand, since the overall volume of the hydrogel, that is the combination of the hydrogel mesh and the solvent, is incompressible, the following equation is valid as

$$\nabla \cdot \left[\varphi_o \boldsymbol{u} + (1 \dot{-} \varphi_l)\boldsymbol{v_l}\right] = 0. \tag{2.15}$$

By the equation (2.14) and (2.15), the following equation

$$\dot{\omega} = \kappa \nabla^2 p \tag{2.16}$$

can be obtained ($\kappa = (1 - \varphi_0)\tilde{\kappa}$). By equation (2.9), the equation (2.12) can be rewritten as

$$\left(K + \frac{1}{3}G\right)\nabla\omega + G\nabla^2\omega = \nabla p. \tag{2.17}$$

The equations (2.7), (2.16), and (2.17) are governing equations of hydrogel dynamics. Based on the equation(2.16) and (2.17), ω satisfy the following diffusion equation

$$\frac{\partial \omega}{\partial t} = D\nabla^2\omega. \tag{2.18}$$

A constant D corresponding to the diffusion constant is

$$D = \kappa(K + \frac{4}{3}G_0). \tag{2.19}$$

The problem of hydrogel dynamics cannot be solved by equation (2.18) alone, so boundary conditions on ω must be given in order to solve this problem. Thus, the equations (2.7), (2.17), and (2.18) must be considered to obtain the solution.

Boundary conditions

There are two boundary conditions for hydrogel dynamics: the dynamics and the solvent flow. Since the mechanical conditions are the same as in elastic mechanics, forces acting on the gel boundary is

$$\boldsymbol{f_{ext}} = (\alpha - p\boldsymbol{I}) \cdot \boldsymbol{n}, \tag{2.20}$$

where $\boldsymbol{n}$ is the normal vector of the boundary. When there is no solvent flowing in and out through the boundary, $\boldsymbol{n} \cdot \boldsymbol{v_{rel}} = 0$ is valid. The conditions for the flow of solvent is

$$\boldsymbol{n} \cdot \nabla p = 0. \tag{2.21}$$

If the solvent flows freely in and out through the boundary, it is continuous at the boundary p.

Free swelling of hydrogel

It is supposed that the hydrogel is immersed in the solvent and allowed to swell freely without any force. A time to reach an equilibrium state, τ, can be estimated up to a^2 / D because the volumetric strain of the hydrogel, ω, satisfies the diffusion equation (2.18). a is the average distance from the surface to the interior of the hydrogel. This estimate gives the correct result in many cases but gives the wrong result when $K \ll G$. If D is given by equation (2.19), τ has a finite value $a^2/\kappa G$ even when $K \rightarrow 0$, but, it is known that τ actually diverges as $a^2/\kappa K$ when $K \rightarrow 0$. Since the driving force for swelling is volumetric elasticity,

the driving force is lost in the limit of K→0. If the hydrogel shape a sphere, a cylinder, or a plane, the time, τ, is described based on the equations (2.7), (2.17), and (2.18) as

$$\tau = \frac{a^2}{D\alpha^2}, \tag{2.22}$$

where α is a value that is determined by its shape.

Chapter 3
Propulsion of spiral-shaped micro-swimmer

3.1 Introduction

3.1.1 Background of spiral-shaped micro-swimmer

One of the most important characteristics of evolutions has been motility, which became for many organisms essential for survival or targeting activities like reproduction[75][76]. To this end, many microorganisms developed soft spiral-shaped flagella (typical helical waveform of *E*. coli[77]: diameter ~400 nm, wavelength 2-5 μm), which are rotated through specialized motor units[78][79]. The motions of soft spiral-shaped flagella in viscous environments (low Reynold's number Re<<1) effectively propel the microorganisms[80]. Those microorganisms can change the morphology of their spiral-shaped flagella to control swimming motility[81] (Fig. 3.1). The morphological change of the flagella achieves robust and adaptive chemotaxis responding to both attractants and repellents such as nutrients, temperature, and pH[82][83]. For example, *E*. coli controls its swimming velocity and direction by deforming its spiral-shaped flagella in response to chemical, mechanical, and temperature modifications[75]. The force for deforming the flagella is on the order of a few piconewtons[84] and the time to changing the swimming direction is typically ~0.1 s[85]. Spermatozoa change the waveforms of their soft flagella within 0.2 s by calcium bursts to

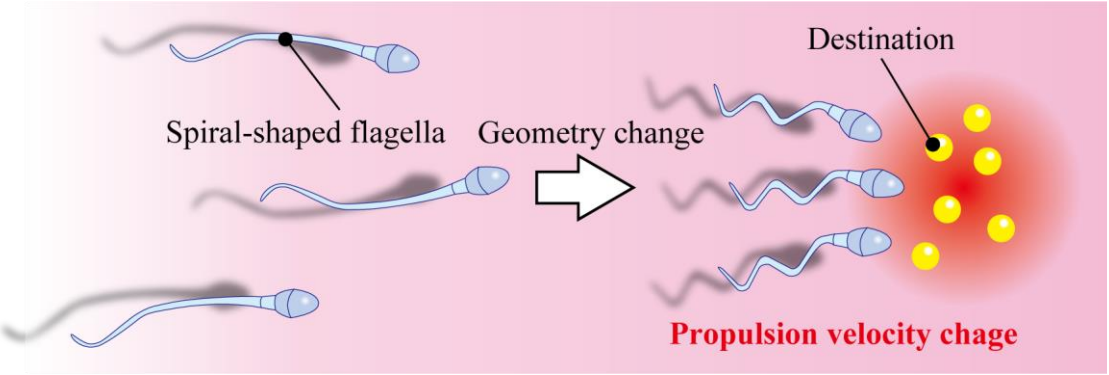

Figure 3.1 Spiral-shaped flagella can change their motility for swimming control

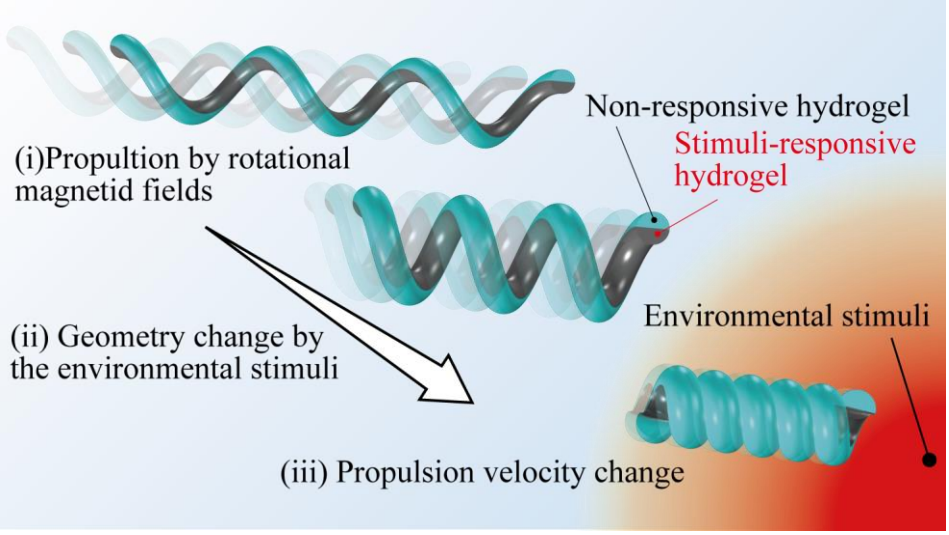

Figure 3.2 Spiral-shaped micro-swimmer integrated with stimuli-responsive hydrogel for autonomous propulsion velocity control.

change their swimming direction in the sperm activating and attracting factor (SAAF)[86]. These functions of autonomous swimming control based on morphology changes are functionally attractive for autonomous micro-robots because these swimming control systems are effective and valuable in the submicron scale to the submillimeter scale.

By mimicking these flagella systems, spiral-shaped micro-swimmers have been developed for various applications[87][38] such as target drug delivery[88], micro-object transport[40], and micro-fluid manipulation[89]. In previous research, several fabrication methods for spiral-shaped micro-swimmers have been reported, including self-scrolling[90],

template-assisted electrodeposition[91][92], glancing and deposition[41], and direct laser printing[40]. These micro-swimmers largely consist of metals and propel themselves by applied external rotational magnetic fields. However, the swimming direction and velocity can be solely controlled by external systems, because the morphology of their spiral bodies cannot be deformed. In addition, individual controls of micro-swimmers in the magnetic field are difficult because of the challenge of adjusting the magnetic fields locally. Therefore, autonomous swimming control, which is controllable by the surrounding environment could pose an advantage for developing micro-swimmers.

In this work, soft spiral-shaped micro-swimmers for autonomous propulsion controlled by detecting stimuli in the surrounding environments were described (Figure 3.2). The main components of our micro-swimmers are hydrogel and magnetic nanoparticles. The spiral-shaped micro-swimmer propels itself by rotational motion excited by magnetic fields. By patterning the stimuli-responsive hydrogel, the spiral shape changes in response to the environmental stimuli, and therefore the swimming motility of the micro-swimmer as well.

3.1.2 Outline of this chapter

In this chapter, the relationship between the geometry of the spiral-shaped micro-swimmer and the propulsion velocity was revealed. First, the parameters related to the propulsion velocity of a spiral-shaped micro-swimmer were theoretically investigated based on fluidic dynamics. Next, the buoyancy-assisted anisotropic gelation method was proposed for fabricating spiral-shaped micro-swimmer with a pitch angle change. Then, the geometry of fabricated spiral-shaped micro-swimmer was measured for discussing the relationship between the geometry of fabricated spiral-shaped micro-swimmer and fabrication conditions. Finally, spiral-shaped micro-swimmers encapsulating magnetic nanoparticles were fabricated for propulsion observation. A setup for applying magnetic fields was also constructed. Finally, the propulsion velocities of spiral-shaped micro-swimmers were observed and compared to the propulsion theory.

3.2 Propulsion theory

Firstly, to design the spiral-shaped micro-swimmers, the effects of geometric parameters on the propulsion velocity were theoretically evaluated. Microorganisms using spiral-shaped flagella for propulsion were modeled using resistive force theory at low Reynold's numbers[80][39]. Resistive force theory assigns a local drag coefficient to a cylindrical element of spiral-shaped flagella (Figure 3.3). For steady-state motion, the externally applied force, *F*, and torque, *T*, must equal the drag on the spiral-shaped micro-swimmer (Detail is described in Appendix A). In a simplified 1D model, the helical motion is described only by the rotation and translation along the spiral axis;

$$\begin{bmatrix} F \\ T \end{bmatrix} = \begin{bmatrix} a & b \\ b & c \end{bmatrix} \begin{bmatrix} u \\ \omega \end{bmatrix}, \tag{3.1}$$

where u is the velocity and ω is the rotation speed. The coefficients, a, b, and c, are functions of geometric parameters and fluid viscosity. Since the geometry of the spiral-shaped micro-swimmer determines the direction of the applied force from the fluid, the propulsion direction is determined by their geometry. They can be modeled with the resistive force theory, resulting in

$$a = \pi n D_{spiral} \left(\frac{\xi_{ll} \cos^2 \alpha + \xi_n \sin^2 \alpha}{\sin \alpha} \right), \tag{3.2}$$

$$b = \frac{\pi n {D_{spiral}}^2}{2} (\xi_{ll} - \xi_n) \cos \alpha, \tag{3.3}$$

$$c = \frac{\pi n {D_{spiral}}^3}{4} \left(\frac{\xi_{ll} \sin^2 \alpha + \xi_n \cos^2 \alpha}{\sin \alpha} \right). \tag{3.4}$$

where ξ_{ll} and ξ_n are drag coefficients along and perpendicular to the cylindrical axis, respectively. These drag coefficients for an infinitesimal cylindrical element on spiral-shaped flagella are defined by Lighthill[80] as

$$\xi_{ll} = \frac{2\pi\eta}{\ln\left(\frac{0.36\pi}{\cos\alpha} I\right)}, \xi_n = \frac{4\pi\eta}{\ln\left(\frac{0.36\pi}{\cos\alpha} I\right) + 0.5}, \tag{3.5}$$

where, η is the fluid viscosity and I is a spring index, $I = D_{spiral} / D_{gel}$. When applying only a rotational magnetic field, the external force, *F*, is zero. Thus the propulsion speed is

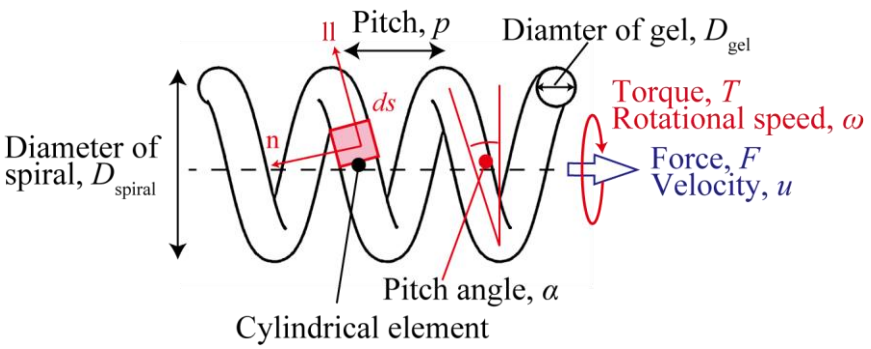

Figure 3.3 Parameters for propulsion theory.

calculated as

$$u = \frac{-b}{a}\omega. \tag{3.6}$$

According to Equations (3.2) and (3.3), the velocity, u, is described as

$$u = \frac{-\frac{\pi n D_{spiral}{}^2}{2}(\xi_{ll}-\xi_n)\cos\alpha}{\pi n D_{spiral}\left(\frac{\xi_{ll}cos^2\alpha+\xi_n sin^2\alpha}{\sin\alpha}\right)}\omega. \tag{3.7}$$

Equation (3.7) can be rewritten by nondimensionalization to ignore the influence of the spiral diameter, D_{spiral}, and the rotation speed, ω,

$$u^* = \frac{u}{D_{spiral}\omega} = \frac{-(\xi_{ll}-\xi_n)\cos\alpha}{2\left(\frac{\xi_{ll}cos^2\alpha+\xi_n sin^2\alpha}{\sin\alpha}\right)} = f(I,\alpha). \tag{3.8}$$

The dimensionless velocity represents the distance the spiral-shaped micro-swimmer travels in one revolution. When the dimensionless velocity is 1, the propulsion speed is the same speed that the spiral-shaped micro-swimmer travels in one revolution. When the spring index, I, ranges from 2.8 to 5.0, the dimensionless velocity, u*, increases as the pitch angle, α, increases from 0 to ~40°. For example, The dimensionless velocity, u*, increases when the pitch angle, α, changes from 0 to ~40° (D_{gel} = 300 μm and D_{spiral} = 1050 μm, I = 3.5) (Figure 3.4 (a)). Thereafter the dimensionless velocity, u*, decreases until the pitch angle, α, reaches ~80º. The range of dimensionless velocity, u*, was 0.039 (α = 10°) to 0.108 (α = 43°). On the other hand, when changing the spring index I (D_{gel} = 300 μm, α = 40°), the dimensionless velocity, u*, was slightly enlarged (0.098–0.118). In other words, the spring index, I, has

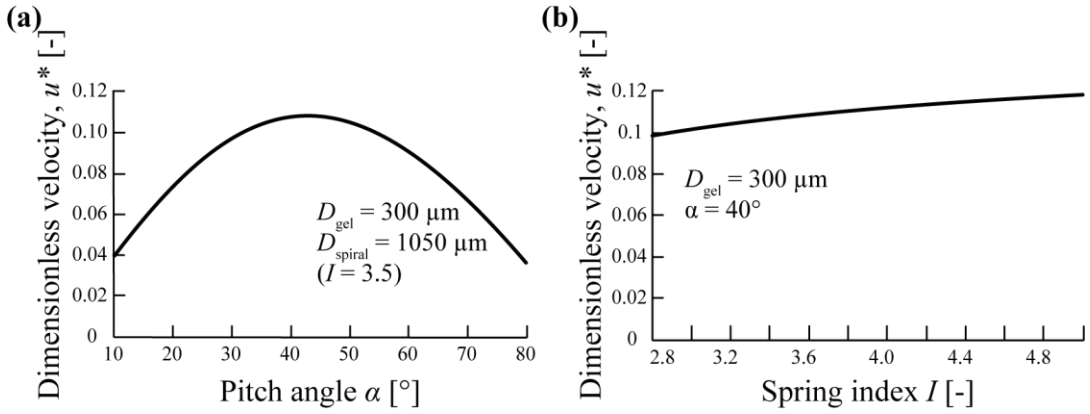

Figure 3.4 Theoretical dimensionless velocity when changing (a) the pitch angle, α, and (b) the spring index, I.

little influence on the dimensionless velocity, u^* (u^* = 0.098–0.118 during I = 2.8–5.0, α = 40°). Thus, we focused on only the pitch angle, α, which represents the degree of expansion and contraction of the spiral-shaped micro-swimmer for controlling the dimensionless velocity, u^*.

3.3 Spiral-shaped hydrogel with different pitch angle

In this section, the buoyancy-assisted anisotropic gelation method was proposed for fabricating the spiral-shaped hydrogel. The relationship between the geometry of spiral-shaped hydrogel and the fabricate conditions was discussed.

3.3.1 Fabrication methods

The spiral-shaped hydrogel was fabricated by an anisotropic gelation method[63]. This fabrication method is largely dependent on a tip angle of the bevel-tip capillary and a flow velocity. Since the timing of hydrogel ejection from the bevel-tip can be different, the spiral-shaped hydrogels were fabricated under conditions that have a high probability of being constructed based on previous research. To form spiral-shaped hydrogel A poly(*N*-isopropylacrylamide-co-acrylic acid) (p(NIPAM-co-AAC), SIGMA-ALDRICH, 741930) solution as a thermo-responsive hydrogel, and a sodium alginate solution (NaAlg; WAKO,

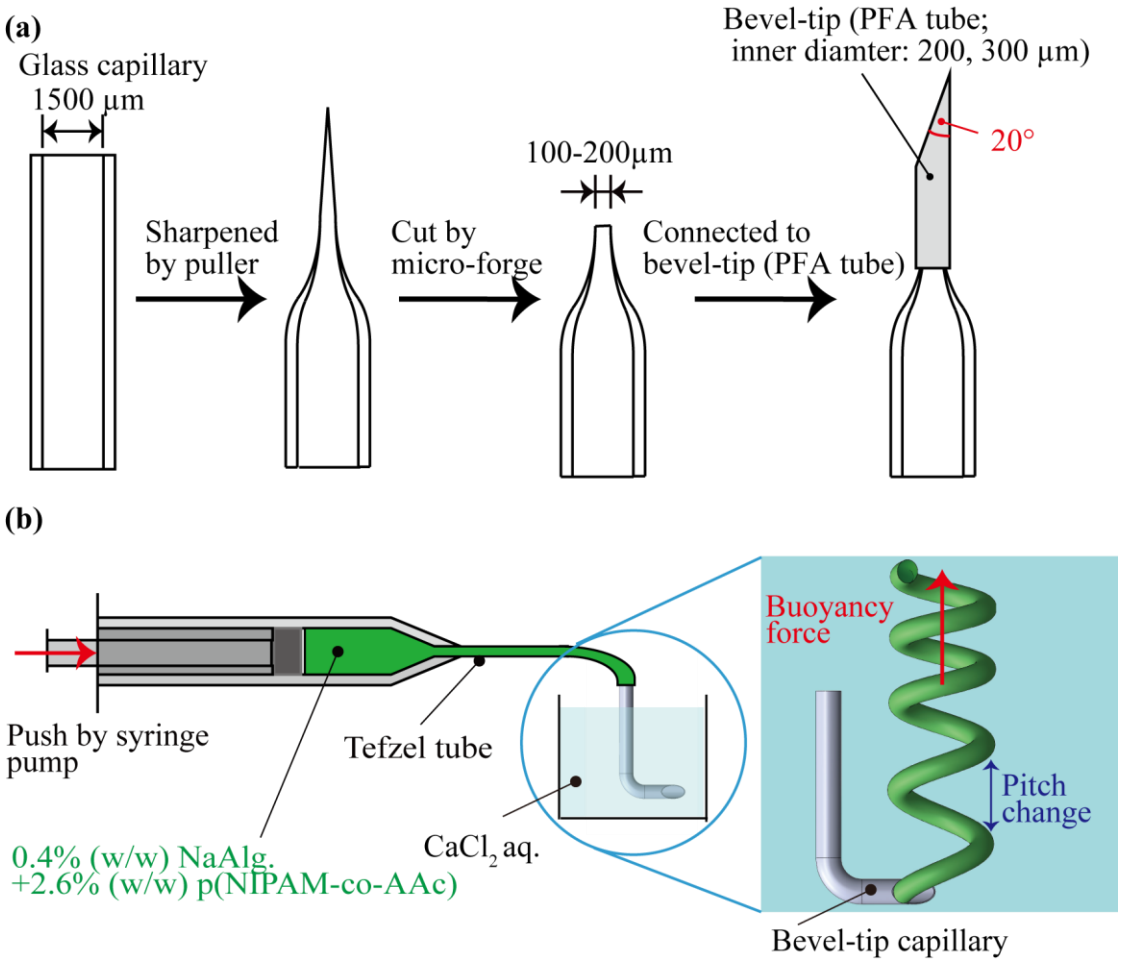

Figure 3.5 Fabrication of spiral-shaped hydrogel. (a) Preparation of the bevel-tip capillary. (b) fabrication setup.

194-13321) as a rapid gelation material were prepared. A calcium chloride solution (1-2M; $CaCl_2$; Wako, 039-00475) was also used to prepare the spiral-shaped hydrogel. Fluorescent micro-beads (5% (v/v); Life Technologies, F8811, yellow-green fluorescent, 0.2 μm) were encapsulated in the mixed solution for visualization of hydrogels.

A microfluidic device for constructing the spiral-shaped hydrogel consists of a bevel-tip, a glass capillary (Outer diameter: 1.5 mm, Inner diameter: 0.9 mm, NARISHIGE, G-1.5) for connection to the bevel-tip, a tefzel tube (VICI, 1/16"×0.5 ETFE), and a syringe (TERUMO, 1 mL). The bevel-tip was prepared by cutting a perfluoroalkoxy (PFA) microtube (inner diameter d = 300 μm) into smaller pieces (the magnitude of the tip angle θ

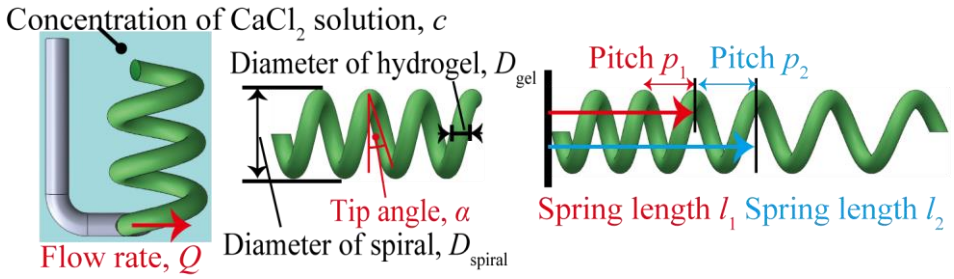

Figure 3.6 Parameters for measurement.

was adjusted to 20º). For connecting to the bevel-tip, the glass capillary was sharpened by a puller (NARISHIGE, PC-10) and the outer diameter of the tip was adjusted to 100-200 μm through a micro-forge (NARISHIGE, MF-900) (Fig. 3.5 (a)). The tefzel tube was connected to the glass capillary with a silicone tube (LABORAN, 9-869-02) and to the syringe through a connector (ISIS, VRF106). Using a syringe pump (KD Scientific, LEGATO 180), 2.6%(w/w) p(NIPAm-co-AAc) + 0.4%(w/w) NaAlg was extruded at different constant flow rates (38, 114, and 190 μL/min) into a 1-2M $CaCl_2$ solution (Fig. 3.5 (b)).

Then, the sizes of the spiral-shaped hydrogel including a diameter of hydrogel, D_{gel}, a diameter of spiral, D_{spiral}, and a pitch, p, produced under different conditions were examined (Figure 3.6). In particular, the effects of the flow rate, Q, and concentration of $CaCl_2$, c, on the resulting size of spiral-shaped hydrogel were investigated. The pitch angle, α, was calculated by measuring the diameter of hydrogel, D_{gel}, the diameter of spiral, D_{spiral}, and the pitch, p, as below,

$$\alpha = \sin^{-1}\left(\frac{p}{2(D_{spiral}-D_{gel})}\right). \quad (3.9)$$

3.3.2 Sizes of spiral-shaped hydrogel with different pitch angle

The spiral-shaped hydrogel was formed upward because of the buoyancy force in the solution. When changing the direction of the bevel-tip capillary, the chirality of the spiral-shaped hydrogel was successfully controlled (Fig. 3.7 (a)). Fabricated spiral-shaped hydrogel had a densely packed part and variable pitch part (Fig. 3.7 (b)). The pitch of the spiral-shaped

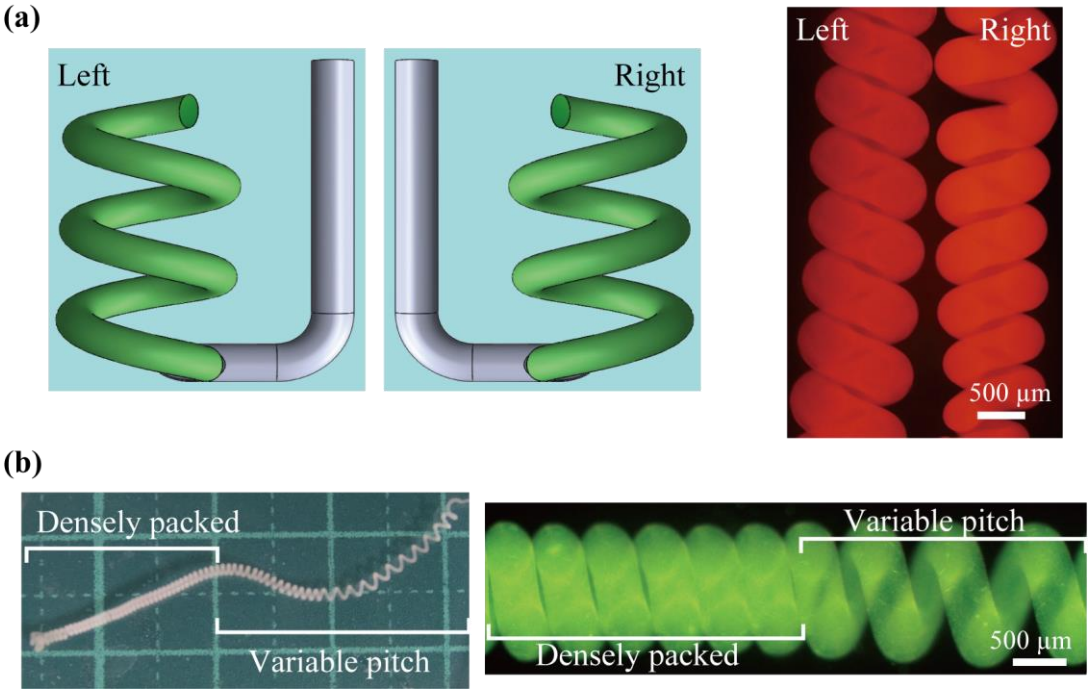

Figure 3.7 Fabricated spiral-shaped hydrogel. (a) the chirality of the spiral-shaped hydrogel could be controlled by the direction of bevel-tip. (b) Fabricated spiral-shaped hydrogel was divided into two parts: the densely packed part and the variable pitch part.

hydrogel was at first densely packed. When the buoyancy force exceeded the deforming force of the spiral-shaped hydrogel, the densely packed part turned into a variable pitch part because the buoyancy force drags the spiral-shaped hydrogel.

Next, measured sizes of the spiral-shaped hydrogel such as the diameter of hydrogel, D_{gel}, the diameter of spiral, D_{spiral}, and the pitch, p, produced under different conditions were discussed (Fig. 3.8). The diameter of hydrogel, D_{gel}, was proportionally correlated to the flow rate, Q, and inversely correlated to the concentration of $CaCl_2$ solution, c (Fig. 3.8 (a) (i)). The diameter of the spiral, D_{spiral}, had a tendency similar to D_{gel}. (Fig. 3.8 (a) (ii)). The result obtained for D_{gel} can be explained by the increase in the amount of mixed pre-gel solution extruded from the bevel-tip capillary. This tendency was consist with previously reported data[93]. It is found that D_{spiral} becomes larger as D_{gel} increased because previous studies revealed that the D_{spiral}/D_{gel} ratio for a spiral-shaped hydrogel fabricated through the anisotropic gelation method was approximately the same[63].

Regarding the pitch of the spirals, it is evaluated that a densely packed region and a variable pitch part (Fig. 3.8 (b)) (d = 300 μm; c = 1, 1.5, 2 M; Q = 38, 114, 190 μL/min). When increasing the flow rate, Q, the length of the densely packed part was decreased from over 5000 μm to 3000 μm (Fig. 3.8 (b) (i), closed circles). The length of the densely packed part was also decreased from 5000 μm to 950 μm by increasing the concentration of $CaCl_2$ solution, c (Fig. 3.8 (b) (ii), closed circles). The gradient of the pitch, Δp, increased by approximately the same amount under each condition ($\Delta p \approx 0.2$ [-], Fig. 3.8 (b), open circles).

Since the buoyancy force of the springs also increased during the fabrication process, the length of the densely packed part was decreased by increasing the flow rate, Q, and the concentration of $CaCl_2$ solution, c. Comparing the lengths of the densely packed part elucidated that the influence of concentration, c, on the length of the densely packed part was larger than that of the flow rate, Q. The gradient of the pitch, Δp, was proportionally correlated to the flow rate, Q. However, since the deforming force of the spring was proportionally correlated to its volume (the volume of spring $\propto$ the flow rate Q), it was estimated that the increase in the gradient of pitch, Δp, was approximately the same in each condition.

Finally, the pitch angle of the fabricated spiral-shaped micro-swimmer was described. The pitch angles of the densely packed part were approximately the same at each condition ($\alpha \sim 16^{o}$). The pitch angle, α, increases as the pitch, p, increases. This tendency is similar to the equation (4.9), because the diameter of gel, $D_{gel,}$ and diameter of spiral, D_{spiral}, remains almost unchanged during spring fabrication. The range of fabricated pitch angles was 15º to 77º. Therefore, the spiral-shaped hydrogel with any pitch angle could be obtained by changing fabrication conditions.

3.4 Swimming velocity of spiral-shaped micro-swimmer

In this section, the relationship between the pitch angle of the spiral-shaped micro-swimmer and the propulsion velocity was examined. First, a magnetic-responsive spiral-shaped hydrogel was fabricated. Then, a setup for applying magnetic fields was also

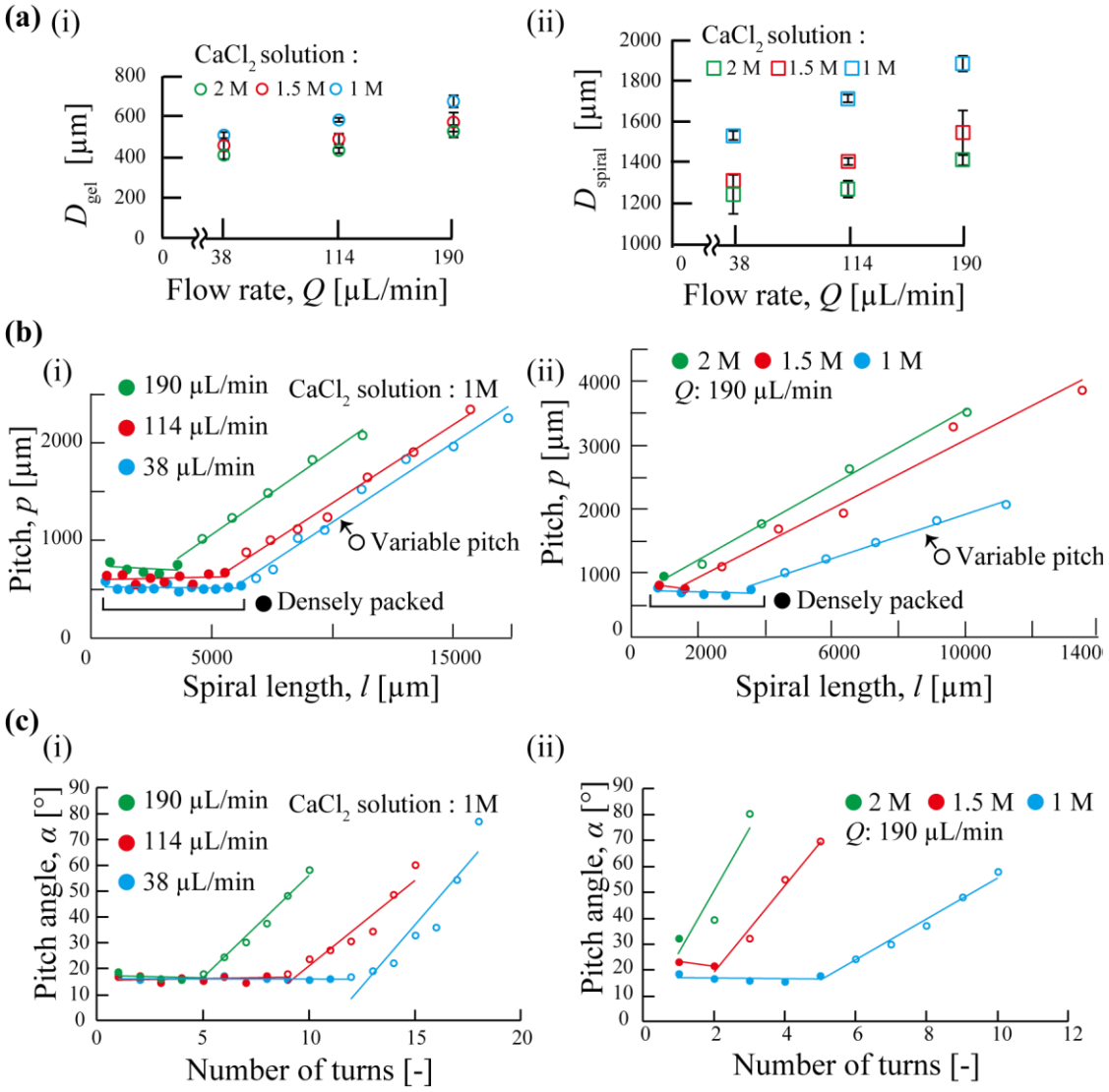

Figure 3.8 (a) Size dependency on flow rate, Q, and concentration of $CaCl_2$ solution, c: (i) D_{gel}, (ii) D_{spiral}, (b), (c) Degree of variable pitch, p, and pitch angle, α, in fabricated spiral-shaped hydrogel. Closed circles show the densely packed part and open circles show the variable pitch part: (i) flow rate, Q, (ii) concentration of $CaCl_2$ solution, c.

constructed. Finally, the propulsion velocity of fabricated spiral-shaped micro-swimmers was then observed.

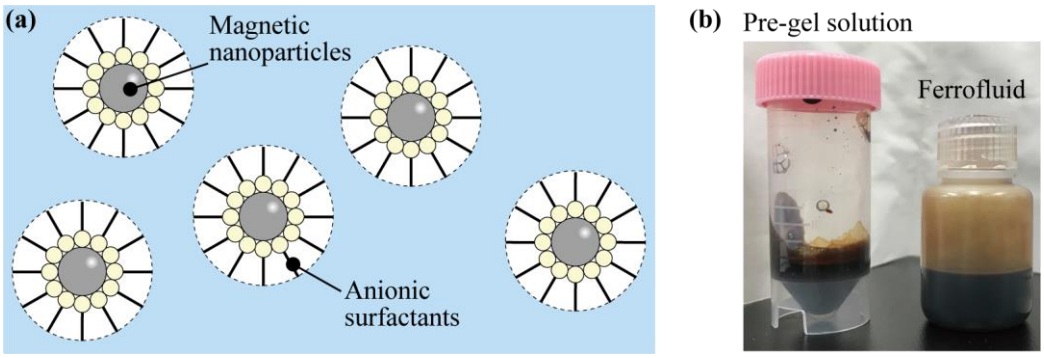

Figure 3.9 (a) Schematic image of ferrofluid. (b) Ferrofluid and the pre-gel solution after desalting.

3.4.1 Fabrication method of spiral-shaped micro-swimmer

Based on the results of chapter 3.3, the buoyancy-assisted anisotropic gelation method was used for fabricating spiral-shaped micro-swimmer with different pitch angles. Magnetic nanoparticles were used for providing a magnetic responsivity to the micro-swimmer. Magnetic nanoparticles (10.2% (v/v), diameter of particles: ~10 nm) encapsulated 2% (w/w) sodium alginate solution (NaAlg) was obtained by mixing ferrofluid (Ferro Tec, EMG707) and 5% (w/w) NaAlg solution. Ferrofluid (EMG707) contains a 17% (w/w) mixture of Fe_3O_4 and γ-Fe_2O_3. 10.2% (v/v) magnetic nanoparticles encapsulated 2% (w/w) NaAlg was desalted by ion exchange resins (BIO-RAD, AG501-X8) at 2 hours without stirring. After desalting, the ion exchange resin was removed through a nylon mesh (Falcon, Cell Strainer, mesh size: 100 μm). The magnetic fluid used in this study is a colloidal dispersion with the magnetic nanoparticles which surface is modified with a surfactant (Fig 3.9 (a)). No deposition of magnetic nanoparticles was observed after mixing and desalting in the pre-gel solution (Fig. 3.9 (b)). Therefore, it is thought that the magnetic nanoparticles are uniformly dispersed in the hydrogel as well as in the colloidal dispersion.

Bevel-tip capillaries were prepared by cutting a perfluoroalkoxy (PFA) microtube (inner diameter: 300 μm) into smaller pieces (the magnitude of the tip angle was adjusted to 20°). The bevel-tip capillary was connected to a syringe (TERUMO, 1 mL) filled with desalted 10.2% (v/v) magnetic nanoparticles encapsulated 2% (w/w) NaAlg via an ethylene

tetrafluoroethylene tube (VICI, 1/16"×0.5). Using a syringe pump (KD Scientific, LEGATO 180), the NaAlg was extruded at a constant flow rate, 200 μL/min, into the 1M calcium chloride ($CaCl_2$) solution. Fabricated spiral-shaped hydrogels were cut to 3 turns (chose a part of approximately the same pitch angle) by scissors (Bio research, 13-308), and the average value of the three turns was used as the representative parameters.

3.4.2 Experimental setup for propulsion of spiral-shaped micro-swimmer

For propulsion velocity observation, the fabricated spiral-shaped micro-swimmers were placed into a chamber surrounded by orthogonal Helmholtz coils (TTRH101-100, Gigateko) (Fig. 3.10). Geometric parameters of Helmholtz coils were summarized in Table 3.1. A swimming chamber was set in the center of the magnetic pole. The chamber was filled with highly viscous fluid 1 M $CaCl_2$ + 0.75 g/mL sucrose solution (WAKO, 196-00015). The sucrose was used for adjusting the viscosity of environmental fluids and the viscosity η is 12.6 mPa s measured by a viscometer (SV-1A, AND).

For applying rotational magnetic fields, cyclic currents (sin wave) were respectively generated to the X and Y coils with 90° phase difference by using 4 equipment: a 2ch function generator (GW Instek, AFG-2225), two motor drivers (Maxon motor, ESCON 70/10), an electric source for switching the motor drivers, and an electric source for a power supply. The voltage that could be output by the function generator is small, so the function generator cannot generate large magnetic fields. Therefore, the motor drivers were used to amplify the outputs of the function generator. The motor drivers have a switching function, which requires a voltage above a threshold (2.4 V) to drive them. When applying the magnetic fields, the voltage (5V) was applied for motor drivers to turn on. The conditions of each piece of equipment were summarized in Table 3.2, and the magnitudes of the magnetic fields in the x and y coils were both 10 mT at these conditions. For propulsion of spiral-shaped micro-swimmer, the rotational magnetic field (10 mT, 5Hz) was applied to the spiral-shaped micro-swimmer (Magnetic actuation principles are described in Appendix B and the frequency-dependent behavior is described in Appendix C).

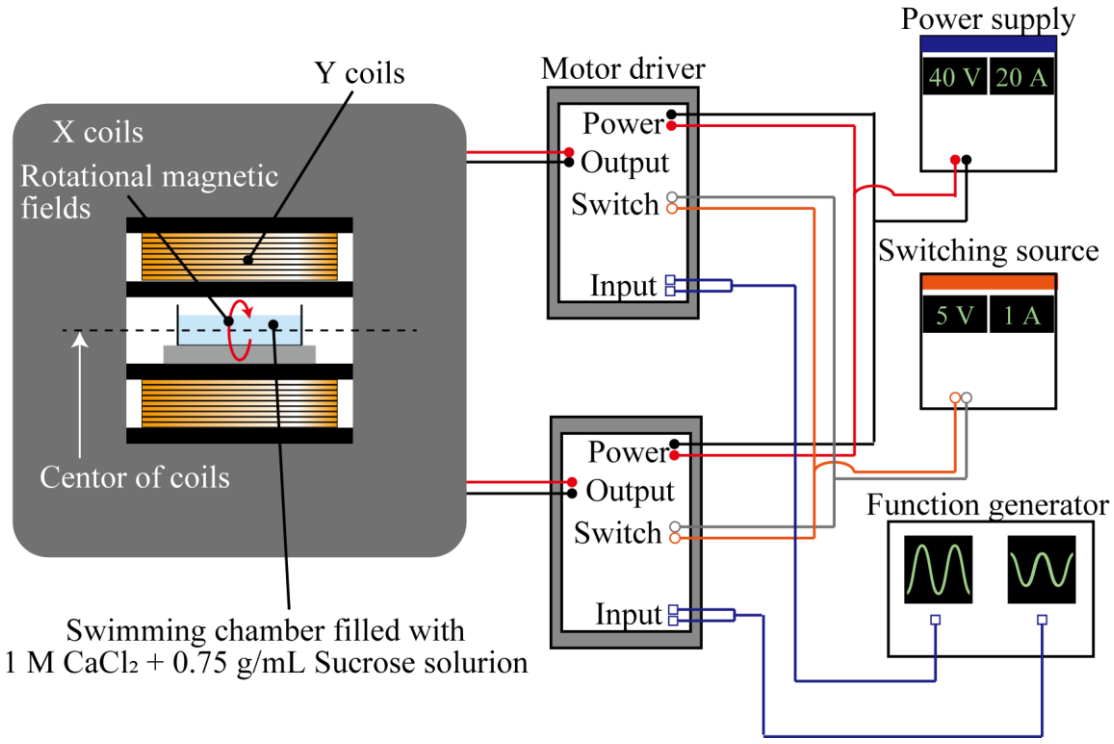

Figure 3.10 Experimental setup for propulsion of spiral-shaped micro-swimmer.

Table 3.1 Geometric parameters of Helmholtz coils

	Displacement of magnetic pole [mm]	Inner diameter [mm]	Outer diameter [mm]
X coils	50	160×190	280×310
Y coils	50	70×80	180×190

The propulsion behavior of the spiral-shaped micro-swimmer was observed from the top of the Helmholtz coil by a digital camera (Olympus, Tough TG-5). The swimming behavior was observed until the spiral-shaped micro-swimmers go down to the chamber bottom. The propulsion velocity, u, and the rotational speed of micro-swimmer, ω, were measured by using video analysis (Adobe, Adobe Premiere Pro 2020).

3.4.3 Dimensionless velocity of spiral-shaped micro-swimmer

Spiral-shaped micro-swimmers with various pitch angles, α = 14°–42°, were

Table 3.2 Conditions for applying magnetic fields

	Function generator			Switching electric source	Power supply
	Amplitude [V]	Phase [-]	Frequency [Hz]		
X coils	3.6	0	5	5V/1A	40V/20A
Y coils	3.1	π/2	5	5V/1A	40V/20A

successfully obtained (average D_{gel} = 476 μm, average D_{spiral} = 1629 μm, typical spiral swimmers at α =17°, 39° are shown in Fig. 3.11 (a)). The spiral-shaped micro-swimmer successfully propelled itself in the viscous fluid (Fig. 3.11 (b)) responding to applied rotational magnetic fields (10 mT, 5Hz). The propulsion velocity, u, the rotational speed, ω, and the spiral diameter, D_{spiral} were measured. The experimentally determines dimensionless velocity, u_e*, was calculated by using these measured values and Equation (4.8). The dimensionless velocity, u_e*, for 12 different swimmers with α = 14°–42° increased with increasing the pitch angle, α (minimum u_e* = 0.026, maximum u_e* = 0.077, Fig. 3.11 (c) dot plots). This increasing tendency was similar to the theoretically calculated dimensionless velocity, u_t*, derived from the geometry of the swimmer (pitch angle, α, and spring index, I) (Fig. 3.11 (c) solid line). The experimentally calculated dimensionless velocity, u_e*, was smaller than the theoretically derived dimensionless velocity, u_t*. It is considered that the resistive force theory is true only for Re = 0 (experimental conditions: Re = 0.051–0.162), and small inertial effects still occur depending on the size and velocity of the spiral-shaped micro-swimmer[39]. Therefore, these results indicate that the propulsion velocity dependence on the pitch angle, α, was experimentally verified in our spiral swimmers.

3.5 Conclusion

In this chapter, it was revealed that the propulsion velocity could be controlled by the pitch angle change based on both theoretical analysis and experimental results.

Micro-scale spiral-shaped hydrogels were successfully fabricated by using the anisotropic gelation method. The size of the spiral could be precisely controlled by the tip diameter, d. In addition, the pitch of the spring, α, could range from 500-4000 μm due to a

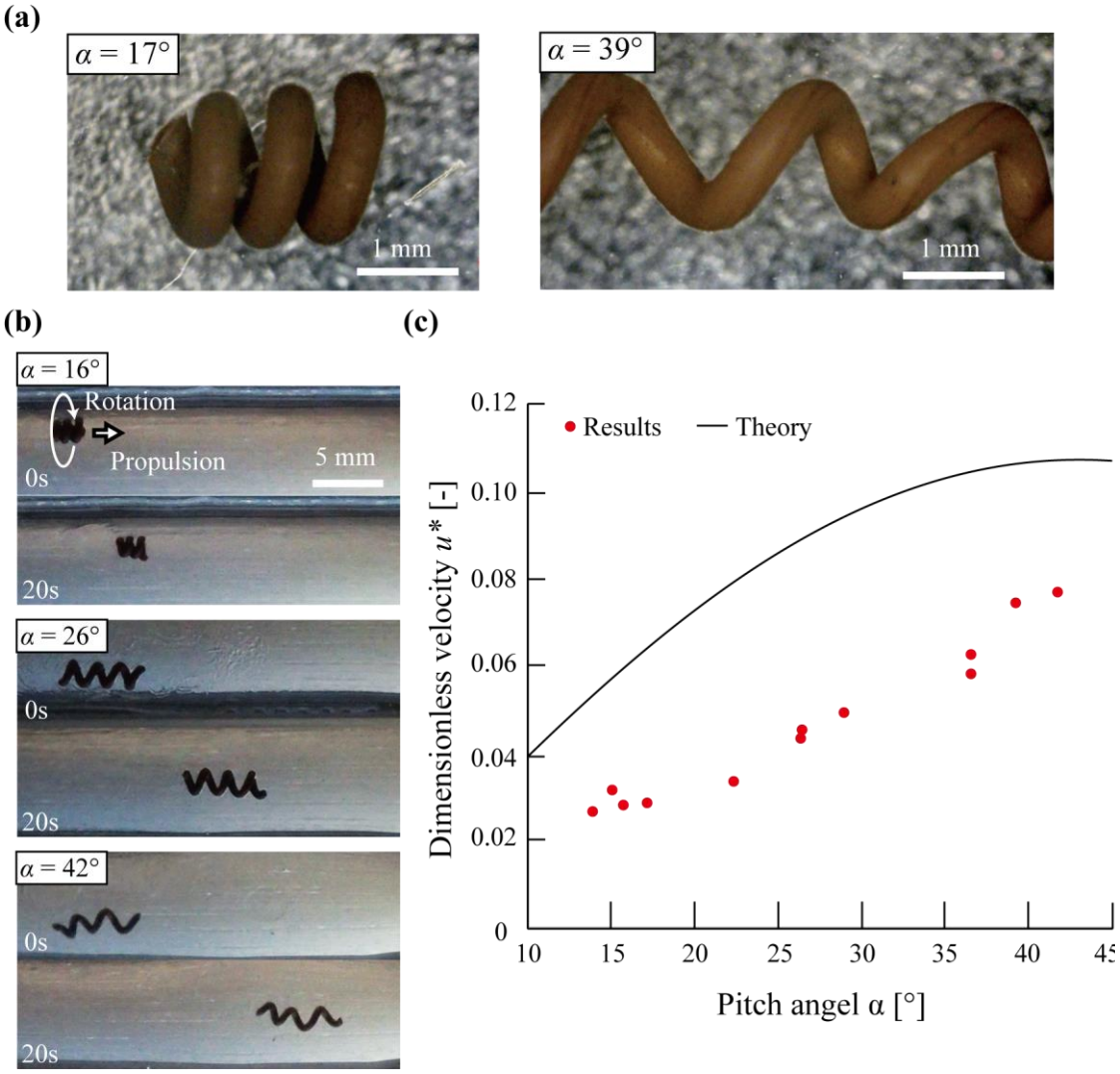

Figure 3.11 Propulsion of spiral-shaped micro-swimmer. (a) Fabricated spiral-shaped micro-swimmer. (b) Propulsion behavior. (c) Dimensionless velocity.

buoyancy force. One of the challenges in this proposed spiral-shaped hydrogel was to continuously fabricate desirable uniform-pitch spirals because the buoyancy increased during the fabrication process, thereby causing a gradient in the pitch. As a solution, using a drag force driven from fluid flow near the bevel-tip capillary could form a uniform-pitch spiral-shaped hydrogel. Furthermore, the spirals' chirality was also controlled.

The spiral-shaped micro-swimmers with various pitch angles (α = 14°–42°) were

also successfully fabricated by the proposed method. By applying the rotational magnetic fields, the propulsion of the spiral-shaped micro-swimmer was succeeded. Although detailed measurements of the forces and torques required for propulsion were not performed in this study, it has been reported in previous studies that they were propelled at several pN[94]. The coefficients related to the diameter of spiral, D_{spiral}, thus it is estimated that the force required for propulsion decreases as the size of micro-swimmer decrease.

The dimensionless velocity, u_e*, for 12 different swimmers with α = 14°–42° increased with increasing the pitch angle, α (minimum u_e* = 0.026, maximum u_e* = 0.077). This increasing tendency was similar to the theoretically calculated dimensionless velocity, u_t*, derived from the geometry of the swimmer (pitch angle, α, and spring index, I) Therefore, the propulsion velocity of spiral-shaped micro-swimmer could be controlled by the pitch angle change.

Chapter 4
Simulation for deformation of spiral-shaped micro-swimmer

4.1 Outline

In this chapter, the deformation behavior of spiral-shaped micro-swimmer was analyzed by using a finite element simulation. Since the stimuli-responsive hydrogel changes its volume isotropically, the stimuli-responsive hydrogel was patterned on the spiral-shaped structure. First, the deformation theory of double-layered structure was discussed based on previous research[95]. Then, Young's modulus and a shrinking ratio of hydrogel were measured to conduct a finite element simulation. For validating the simulation, deformations of the double-layered fiber-shaped structure were compared. Finally, the deformation of spiral-shaped was analyzed and the propulsion velocity change was calculated based on the deformation simulation.

4.2 Deformation theory of double-layered structure

The symbols mainly used in this section are as follows.

α	Thermal expansion coefficient [1/K]
a	Thickness of the material [m]
h	Total thickness of the beam [m]

ρ	Radius of the beam [m]
E	Modulus of elasticity [Pa]
P	Tensile force [N]
M	Bending moment [N·m]
I	Moment of inertia of area [m^4]
δ	Deflection [m]

A thin beam made of two materials is uniformly heated from t_0°C to t°C. When applying the heat, the beam will bend due to the difference in thermal expansion coefficients. The width of the beam is taken as equal to unity. The following analysis has been made on the assumption that cross-sections of the beam originally plane and perpendicular to the axis remain plane during bending and become perpendicular to the curved axis of the beam. Consider an element cut out from the beam by two cross-sections mn and m_1n_1. If $\alpha_2 > \alpha_1$, the deflection will be convex down, as shown in Fig. 4.1. All the forces acting over the section of material 1 on the concave side can be defined by an axial tensile force P_1 and bending moment M_1. For material 2 on the convex side, all forces acting on the cross-section can be also defined by an axially compressive force P_2 and bending moment M_2. Due to no external forces acting on the beam, all forces acting over any cross-section of the beam must be equal, therefore,

$$P_1 = P_2 = P \tag{4.1}$$

$$\frac{Ph}{2} = M_1 + M_2. \tag{4.2}$$

Each bending moment can be represented by the radius ρ and the flexural rigidity E_xI_x as bellow:

$$M_x = \frac{E_xI_x}{\rho}. \tag{4.3}$$

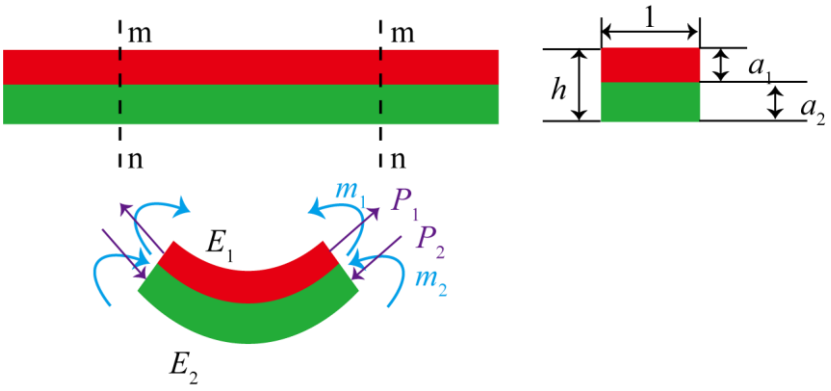

Figure 4.1 Deflection of double-layered beam while uniformly heated.

The equation (2.56) was substituted in equation (2.55),

$$\frac{Ph}{2} = \frac{E_1 I_1 + E_2 I_2}{\rho}. \tag{4.4}$$

Another equation for calculating P and ρ will be obtained from the consideration of deformation. On the bearing surface of both materials, the unit elongation occurring in the longitudinal beams of materials 1 and 2 must be equal, therefore,

$$\alpha_1(t - t_0) + \frac{P_1}{E_1 a_1} + \frac{a_1}{2\rho} = \alpha_2(t - t_0) + \frac{P_2}{E_2 a_2} + \frac{a_2}{2\rho}. \tag{4.5}$$

By using equation (2.54) and (2.55), equation (2.58) can be represented as

$$\frac{h}{2\rho} + \frac{2(E_1 I_1 + E_2 I_2)}{h\rho}\left(\frac{1}{E_1 a_1} + \frac{1}{E_2 a_2}\right) = (\alpha_2 - \alpha_1)(t - t_0). \tag{4.6}$$

Then, equation (2.59) can also be represented as

$$\frac{1}{\rho} = \frac{(\alpha_2 - \alpha_1)(t - t_0)}{\frac{h}{2} + \frac{2(E_1 I_1 + E_2 I_2)}{h}\left(\frac{1}{E_1 a_1} + \frac{1}{E_2 a_2}\right)}. \tag{4.7}$$

In addition, by using the moment of inertia of area $I_x = \frac{a_x^3}{12}$ and ratios $\frac{a_1}{a_2} = m, \frac{E_1}{E_2} = n$, the curvature of the beam can be represented as

$$\frac{1}{\rho} = \frac{6(\alpha_2 - \alpha_1)(t - t_0)(1+m)^2}{h(3(1+m)^2 + (1+mn)\left(m^2 + \frac{1}{mn}\right)}. \tag{4.8}$$

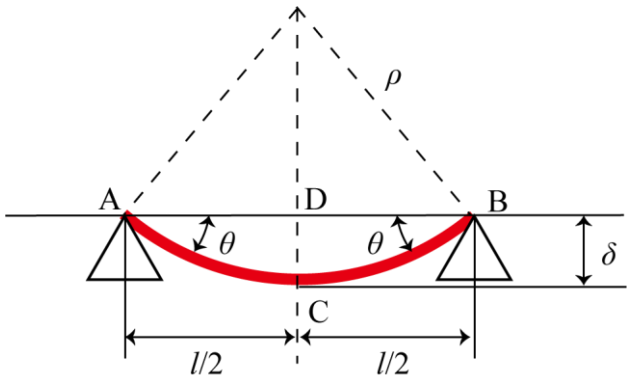

Figure 4.2 Deflection of simply supported double-layered beam.

If the thickness of materials is equal ($a_1 = a_2$, m = 1), the curvature can be rewritten as

$$\frac{1}{\rho} = \frac{24(\alpha_2-\alpha_1)(t-t_0)}{h\left(14+n+\frac{1}{n}\right)}. \tag{4.9}$$

In addition, the radius can be obtained by a deflection δ. It is considered the condition that a beam AB of bimorph simply supported at the ends be bent due to uniform heating, as shown in Fig. 4.2. Then from the fact that the curve ACB is an arc of a circle having radius ρ it follows, that,

$$\delta(2\rho - \delta) = \left(\frac{l}{2}\right)^2. \tag{4.10}$$

Moreover, if the deflection is small in comparison with the radius, the equation (2.63) can be approximated as

$$2\rho\delta = \frac{l^2}{4}. \tag{4.11}$$

4.3 Measurement of parameters

For conducting the deformation simulation, a young's modulus, a Poisson's ratio, and a shrinking ratio of stimuli-responsive hydrogel were required. The young's modulus and the shrinking ratio were measured by following experiments. The Poisson's ratio that was measured in previous work was used.

4.3.1 Measurement of Young's modulus

Firstly, the hydrogel pieces were fabricated for the measurement of the young's modulus. p(NIPAm-co-AAc) (2.6%(w/w)) + NaAlg (0.4%(w/w)) as a stimuli-responsive hydrogel and NaAlg (1.0% (w/w)) + propylene glycol alginate (1.0% (w/w); PGAlg; Wako, 165–17415) as a non-responsive hydrogel were used. Each reagent was filled in a silicone tube (inner diameter: 7mm, outer diameter 9 mm), and the tube was placed in a cell strainer (40μm, FAL-2340, Falcon). Then, the cell strainer with the tube was immersed in 1 M $CaCl_2$ solution overnight. After gelation, the hydrogels were removed from the silicone tube. The calcium alginate hydrogel (the non-responsive hydrogel) was largely shrunk with the gelation, and the diameter of the non-responsive hydrogel decreased to 5 mm. The stimuli-responsive hydrogel did not shrink much and have a 7 mm diameter. The hydrogels were cut with a disposable scalpel (2-5726-21, AS ONE) to a thickness of 4 mm. The stimuli-responsive hydrogel was heated at 50ºC for 5 min before measurement.

Young's modulus is measured by a force meter (FGP-1, SHIMPO). A load was applied to the hydrogel pieces by pushing the force meter at a constant speed (0.2 mm/s). The force meter was moved through a Z stage (OSMS26-50(Z), Sigma Koki). The measurement was started when 0.1 mN was applied and stopped when a strain reached 0.2. Three pieces of each hydrogel were measured, and the average value was determined as the representative of Young's modulus.

4.3.2 Measurement of Shrinking ratio

For measuring the shrinking ratio of stimuli-responsive hydrogel, a sphere-shaped stimuli-responsive hydrogel and a fiber-shaped stimuli-responsive hydrogel were fabricated by using p(NIPAm-co-AAc) (2.6%(w/w)) + NaAlg (0.4%(w/w)). The pre-gel solution was extruded into 1 M $CaCl_2$ solution through a glass capillary (inner diameter: 1 mm) at a constant speed (300 μL/min). When fabricating the sphere-shaped stimuli-responsive hydrogel, the tip of the glass capillary was not soaked in the $CaCl_2$ solution. when fabricating the fiber-shaped stimuli-responsive hydrogel, the tip of the glass capillary was soaked in the

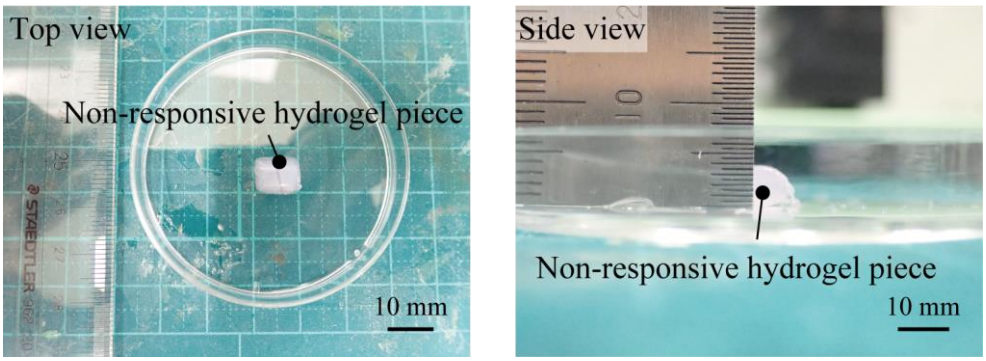

Figure 4.3 Hydrogel piece for measurement of Young's modulus.

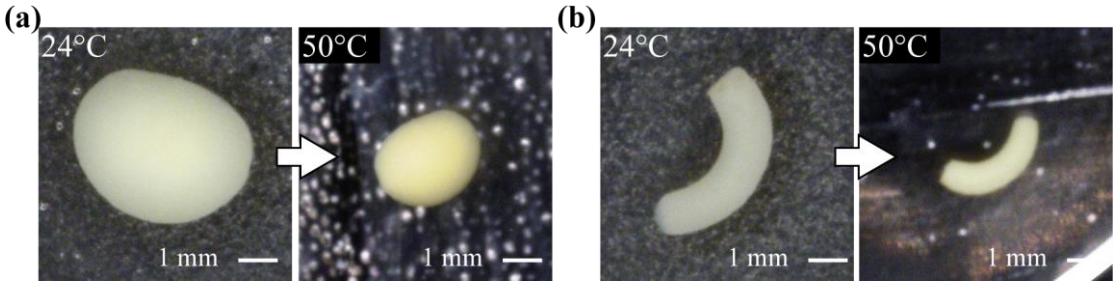

Figure 4.4 Thermal responsiveness of (a) Sphere-shaped hydrogel and (b) fiber-shaped hydrogel.

$CaCl_2$ solution.

The fabricated stimuli-responsive hydrogels were applied thermal stimuli (~50º) through a hot plate for 5 min. The temperature of the $CaCl_2$ solution was confirmed with a thermometer (PT-7LD, Optex). The diameters before and after deformation were measured by a digital microscope (Keyence., VH-5500).

4.3.3 Result of measurement parameters

The hydrogel pieces were fully gelled by calcium chloride solution (Fig. 4.3). The load was linearly related to the displacement before the strain reached 0.2. The young's modulus of stimuli-responsive hydrogel and non-responsive hydrogel were 13.5 kPa and 48.3 kPa, respectively.

Both sphere-shaped and fiber-shaped were shrunk responding to the thermal stimuli (Fig. 4.4). Before shrinking, the average diameters of sphere-shaped and fiber-shaped

hydrogel were3174 μm and 838 μm, respectively. After shrinking, both average diameters of sphere-shaped and fiber-shaped hydrogel were decreased to 1936 μm and 519 μm, respectively. Both shrinking ratios were approximately the same and the average shrinking ratio was 0.385. It is considered that the shrinking ratio of stimuli-responsive hydrogel did not depend on its geometry.

4.4 Simulation validation for deformation simulation

The simulation validation was evaluated by comparing the simulation results and experimental results. Since it is important that the deformation behavior of the double-layered hydrogel is approximately the same in both the experimental results and the simulation results, each radius of curvature after deformation is compared.

4.4.1 Fabrication of double-layered fiber-shaped hydrogel

To form double-layered fiber-shaped hydrogel, 2.6 %(w/w) p(NIPAm-co-AAc) + 0.4 %(w/w) NaAlg as a stimuli-responsive layer, and 1.5% w/w NaAlg + 1.0% w/w propylene glycol alginate (PGAlg) as a non-responsive layer were used. The PGAlg was used to adjust the viscosity. By using a Y-connector (ISIS, VFY106Y), a double-layered laminar flow was created. The double-layered pre-gel solution was ejected into a calcium chloride solution via a glass tube (inner diameter: 0.6 mm, outer diameter: 1 mm; G-1; Narishige).

A geometry of fabricated double-layered fiber was measured by the digital microscope (Keyence, VH-5500). Then, the fabricated double-layered fiber was applied thermal stimuli by 1 M $CaCl_2$ solution at 50ºC for 5 min. After applying the thermal stimuli, the radius of curvature was also measured by the digital microscope.

4.4.2 Conditions of simulation

To analyze the deformation behavior of double-layered fiber-shaped hydrogel, a finite-element simulation was conducted by COMSOL Multiphysics Ver. 5.4. In this calculation, swell and shrink behaviors of the stimuli-responsive hydrogel were simplified as

Table 4.1 Simulation parameters of stimuli-responsive hydrogel and non-responsive hydrogel.

Parameters	Stimuli-responsive hydrogel	Non-responsive hydrogel
Heat expansion coefficient [1/K]	-0.385	0
Young's modulus [Pa]	13.5	48.3
Poisson's ratio [-]	0.25	0.31

an object deformation caused by thermal shrinkage. Based on the fabricated double-layered fiber-shaped hydrogel, a double-layered fiber-shaped hydrogel model was constructed. The diameter of the double-layered fiber-shaped model was 594.5 μm and a radius of curvature before deformation was 2667.23 μm (a center angle was 73º; Fig 4.5 (b) left). The cross-section of the double-layered fiber-shaped model was a circle. The measured Young's modulus and the shrinking ratio were used. Because the non-responsive hydrogel did not shrink responding to the thermal stimuli, the shrinking ratio of non-responsive hydrogel was defined as 0. Based on the previous research, the Poisson's ratio of stimuli-responsive hydrogel and non-responsive hydrogel were 0.25[96] and 0.31[97], respectively. These parameters were summarized in Table 4.1. The minimum mesh size of this simulation was 0.059 μm. As a fixed constraint, one end of the non-responsive hydrogel was set to zero displacements in the x, y, and z-axis. Because of the large amount of deformation, a nonlinear deformation analysis was performed. The temperature was raised by 1 ºC for heat shrinkage, and only before and after deformation were compared.

4.4.3 Deformation of double-layered hydrogel fiber

First, the geometry of fabricated double-layered fiber was measured for constructing the simulation model. The diameter of double-layered fiber was 594.5 μm, and the radius of curvature before deformation was 2667.23 μm (the center angle was 73.9º; Fig. 4.5 (a) left). The fabricated double-layered fiber-shaped hydrogel was bent responding to the thermal stimuli. The radius of curvature after deformation was decreased to 424 μm (Fig. 4.5 (a)

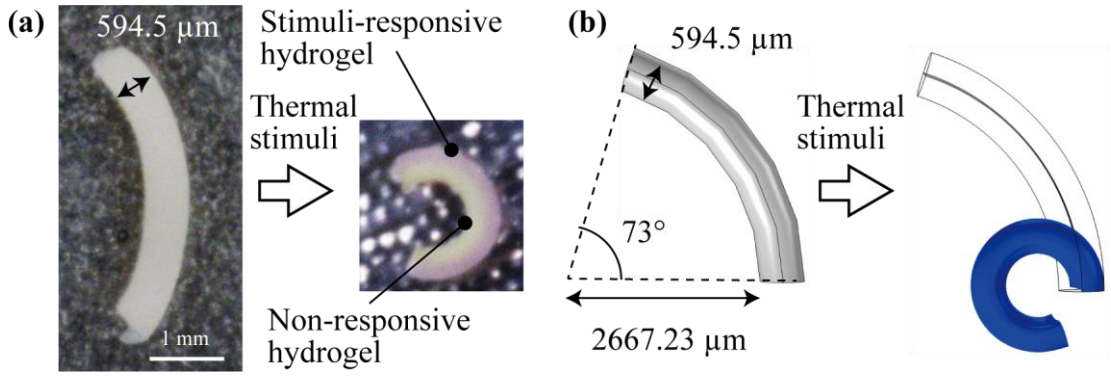

Figure 4.5 Deformation of double-layered fiber-shaped hydrogel. (a) Experimental results. (b) Simulation results.

right).

4.4.4 Results of deformation simulation of double-layered hydrogel fiber

The double-layered fiber-shaped hydrogel model was also bent responding to the applying thermal stimuli (Fig. 4.5 (b) right). This bending behavior was similar to the experimental results. The radius of curvature after deformation was 417 μm, that approximately the same value as the experimental results (424 μm). Therefore, the measured parameters (Young's modulus and shrinking ratio) and simulation conditions (mesh size and condition of constraint) were suitable for the deformation simulation.

4.5 Deformation Simulation of spiral-shaped micro-swimmer

Based on Chapter 4.4, the deformation of double-layered spiral-shaped hydrogel was analyzed. Then, the propulsion velocity change was calculated based on the simulation results and the resistive force theory.

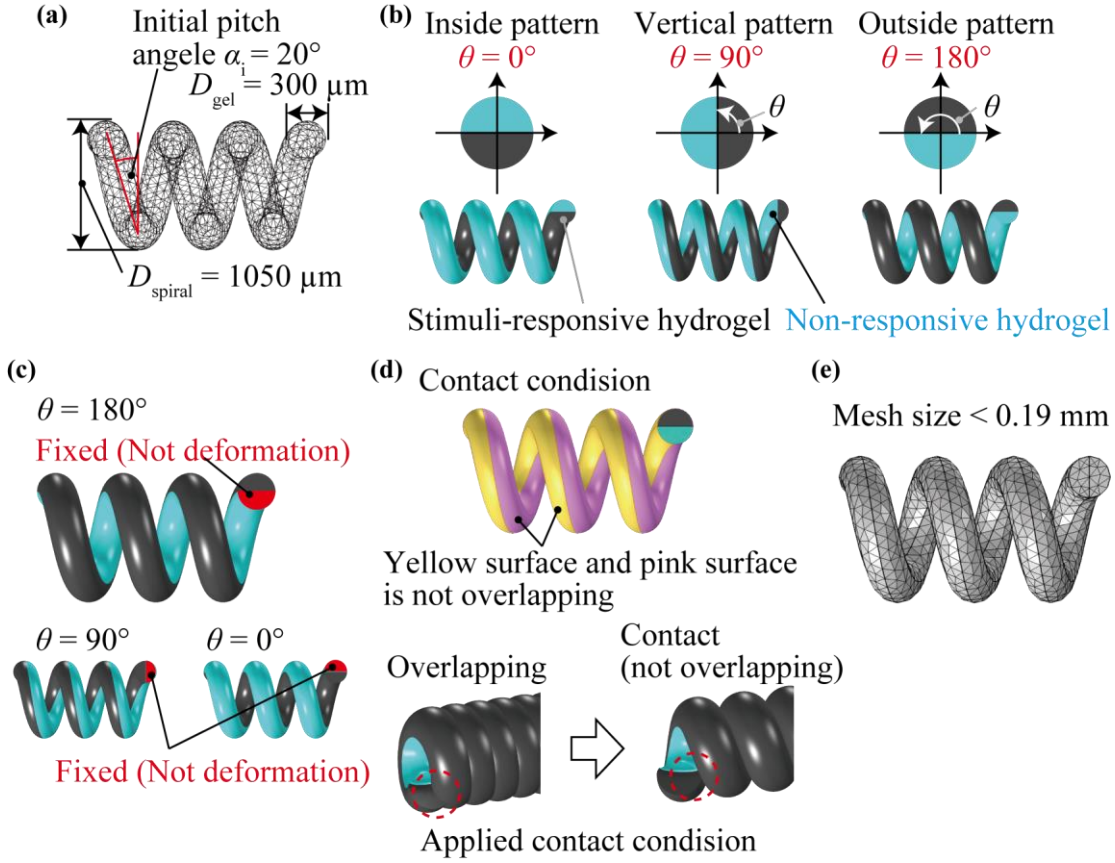

Figure 4.6 Conditions of the finite element simulation. (a) Geometry of the simulation models. (b) Schematic image of the double-layered spiral-shaped micro-swimmer. (c) The restraint condition of each double-layered spiral-shaped micro-swimmers. (d) The contact conditions of deformation simulation. (e) The 3D meshing of the spiral-shaped micro-swimmer.

4.5.1 Simulation conditions

To analyze the deformation behavior of double-layered spiral-shaped hydrogel, the finite-element simulation was also conducted by COMSOL Multiphysics Ver. 5.4. In this calculation, swell and shrink behaviors of the stimuli-responsive hydrogel were also simplified as an object deformation caused by thermal shrinkage. The geometry of spiral-shaped hydrogel was determined as D_{gel} = 300 μm, D_{spiral} = 1050 μm (Fig. 4.6 (a)). Physical

parameters of the stimuli-responsive hydrogel and non-responsive hydrogel for this calculation were the same in Chapter 4.4 (Table 4.1). Three types of bi-layered spiral swimmer models were built with different pattern angles θ = 0° (inside pattern), 90° (vertical pattern), and 180° (outside pattern), as shown in Fig. 4.6 (b). For the boundary condition, the one end of the non-responsive hydrogel was fixed (not move and deform to any axis, Fig. 4.6 (c)). The surface of the double-layered spiral-shaped micro-swimmers could not be overlapped by a contacting condition (Fig. 4.6 (d)). The minimum mesh size of our simulation was approximately 0.19 mm (Fig. 4.6 (e)). Because of the large amount of deformation, nonlinear deformation analysis was also performed. The temperature was raised by 1 ºC for heat shrinkage, and only before and after deformation were compared.

And then, the results of the deformation simulation were analyzed towards the deformation direction and the amount of deformation. Using these calculation results, the dimensionless velocity, u^*, was calculated by Equation (3).

4.5.2 Analysis of propulsion velocity change

First, the influence of the pattern angle, θ, on the deformation was investigated. At θ = 0°, the inside pattern spiral-shaped micro-swimmer was compressed (Fig. 4.7 (a), left). On the other hand, the outside pattern spiral-shaped micro-swimmer (θ = 180°) was expanded (Fig. 4.7 (a), right). These results show that the direction of deformation depends on the pattern angle, θ. The more detailed analysis by changing the pattern angle, θ, was described in Appendix D.

Next, the results of the deformation simulation were analyzed towards the deformation direction and the amount of deformation. The gap of the spiral, $G = p – D_{gel}$ (Fig. 4.7 (b), inset) was evaluated because the deformable range of the double-layered spiral-shaped micro-swimmer is limited by the gap G. The spiral-shaped micro-swimmer was completely packed and not contracted further when the gap G = 0. Initially, the gap, G, before deformation was 304 μm (Fig. 4.7 (b), white bar). After the stimulus, the inside pattern spiral-shaped micro-swimmer (θ = 0°, G = 36 μm, Fig. 4.7 (b), red bar) and the vertical pattern spiral-shaped micro-swimmer (θ = 90°, G = 96 μm, Fig. 4.7 (b), green bar) contracted,

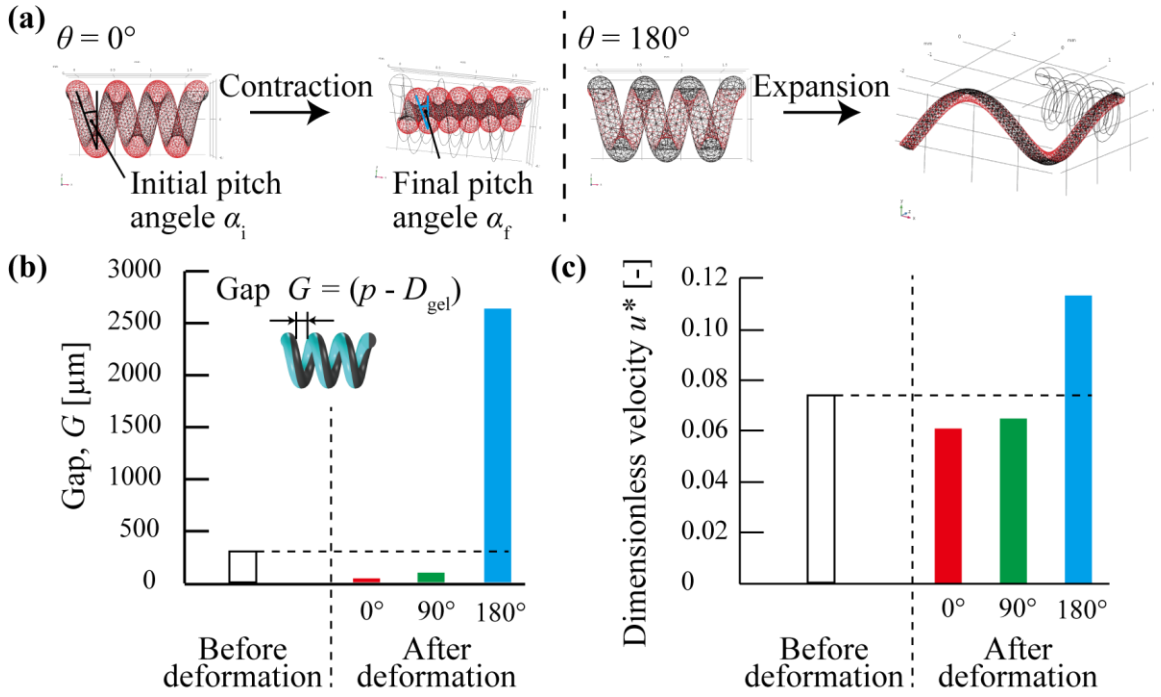

Figure 4.7 Finite element simulation of double-layered spiral-shaped micro-swimmer. (a) The simulation results of the inside pattern spiral-shaped micro-swimmer (left) and the outside pattern spiral-shaped micro-swimmer (right). The gap, G, before and after deformation. (c) The dimensionless velocity, u^*, before and after deformation.

whereas the outside pattern spiral-shaped micro-swimmer (θ = 180°, G = 2641 μm, Fig. 4.7 (b), blue bar) expanded. The deformation amount of the outside pattern spiral-shaped micro-swimmer (θ = 180°) was much larger than both of the inside pattern spiral-shaped micro-swimmer (θ = 0°) and the vertical pattern spiral-shaped micro-swimmer (θ = 90°). These results indicate that the deformation direction and the amount of deformation can be designed through the pattern angle, θ.

Using these calculation results, the dimensionless velocity, u^*, was calculated by Equation (3.8). The initial dimensionless velocity before deformation, u_i^*, was 0.074 (Fig. 4.7 (c), white bar). The calculated dimensionless velocities after deformation, u_f^*, were 0.061 (θ = 0°, Fig. 4.7 (c), red bar), 0.065 (θ = 90°, Fig. 4.7 (c), green bar) and 0.113 (θ = 180°, Fig.4.7 (c), blue bar). To clarify the propulsion velocity change before and after the stimulus,

the difference in dimensionless velocity, $\Delta u^* = u_f^* - u_i^*$, was focused. The inside pattern spiral-shaped micro-swimmer ($\theta = 0°$) and the vertical pattern spiral-shaped micro-swimmer ($\theta = 90°$) became slower ($\theta = 0°$: $\Delta u^* = -0.0129$; Fig. 4.7 (c), red bar, $\theta = 90°$: $\Delta u^* = -0.0086$; Fig. 4.7 (c), green bar). On the other hand, only the outside pattern spiral swimmer ($\theta = 180°$) became faster by the deformation ($\Delta u^* = 0.0399$, Fig. 4.7 (c), blue bar). These results show that the propulsion velocity change of the double-layered spiral-shaped micro-swimmer varied by changing the pattern angle, θ.

4.6 Conclusion

To summarize the simulation results, the large deceleration could be realized when the patterning angle, $\theta = 0^o, 90^o$. In addition, the amount of deceleration could be enlarged as the initial pitch angle, α_i, increasing, because the double-layered spiral-shaped hydrogel could be largely deformed without inhibiting the contact of hydrogel (Appendix D). Besides, it is expected to realize the acceleration by using the expansion of a double-layered spiral-shaped micro- swimmer. The pitch angle was changed from 20^o to ~50^o when the patterning angle, $\theta = 180^o$, and the initial pitch angle, $\alpha_i = 20^o$. Based on the restive force theory, the difference of dimensionless velocity was $\Delta u^* = 0.0399$, thus the spiral-shaped micro-swimmer could be accelerated. On the other hand, the spiral shape was deformed to the nearly fiber shape as the initial pitch angle, α_i, increasing when the double-layered spiral-shaped micro-swimmer expanded. Therefore, the patterning angle, $\theta = 0^o$or 90^o, and the large initial pitch angle, α_i, were suitable for deceleration behavior. In contrast, the patterning angle, $\theta = 180^o$, and the small initial pitch angle, α_i, were suitable for deceleration behavior.

Chapter 5
Autonomous propulsion velocity control of spiral-shaped micro-swimmer

5.1 Introduction

In this chapter, the propulsion velocity changes of double-layered spiral-shaped micro-swimmer based on the deformation simulation were described. First, the deformation of double-layered spiral-shaped hydrogel was observed. Then, the propulsion velocity changes of the double-layered spiral-shaped micro-swimmer were investigated.

5.2 Deformation of stimuli-responsive spiral-shaped hydrogel

In this section, it is observed that whether the deformation behavior was changed by patterning of the stimuli-responsive hydrogel as the simulation results. For comparing the deformation behavior, the single-layered spiral-shaped hydrogel, the vertical patterned spiral-shaped hydrogel with various pitch, and outside patterned spiral-shaped hydrogel was fabricated.

5.2.1 Fabrication of stimuli-responsive spiral-shaped hydrogel

Single-layered spiral-shaped hydrogel

For fabricating the single-layered spiral-shaped hydrogel, 2.6%(w/w) p(NIPAm-co-

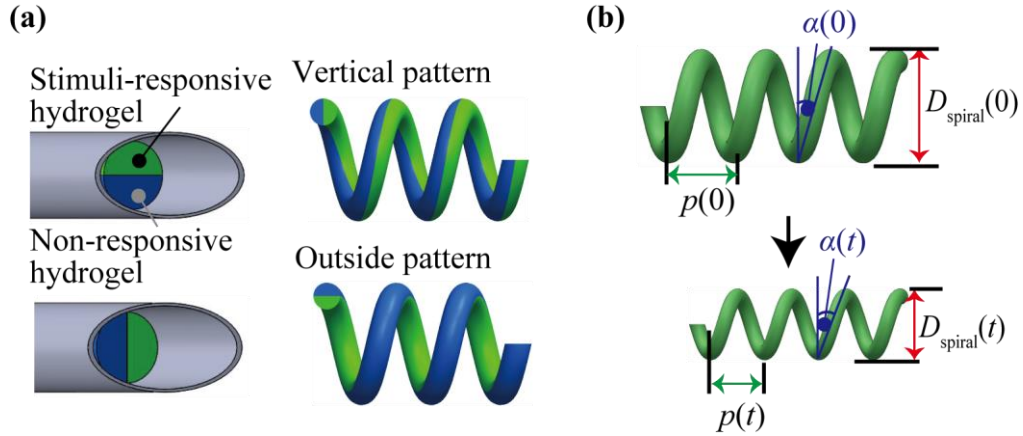

Figure 5.1 (a) Direction of laminar follow for vertical pattern and outside pattern. (b) definition of shaped parameters as a function of time: t, pitch: $p(t)$, diameter: $D_{spiral}(t)$, and pitch angle: $\alpha(t)$.

AAc) + 0.4%(w/w) NaAlg was extruded into 1 M $CaCl_2$ solution via a bevel-tip capillary (d = 200 μm, tip angle: 20°) at constant flow rate (Q = 38 μL/min).

Double-layered spiral-shaped hydrogel

In the microfluidic capillary with a bevel tip, a double-layer laminar flow by using 2.6 %(w/w) p(NIPAm-co-AAc) + 0.4 %(w/w) NaAlg as a stimuli-responsive layer, and 1.5% (w/w) NaAlg + 1.0% (w/w) propylene glycol alginate (PGAlg) as a non-responsive layer was created. The PGAlg was used to adjust the viscosity. By using the double-layered laminar flow created in the bevel-tip capillary with a Y-connector (ISIS, VFY106Y), a double-layered laminar flow was created. Flow rates for each layer were controlled. The stimuli-responsive solution flowed at a rate of 28.6 μL/min, and the non-responsive solution flowed at a rate of 7.5 μL/min.

When forming outside patterns of double-layered spiral-shaped hydrogel, the direction of the laminar flow pattern to the bevel-tip capillary was adjusted (Fig. 5.1 (a)). Flow rates for each layer were controlled. The stimuli-responsive solution flowed at a rate of 28.5 μL/min, and the non-responsive solution flowed at a rate of 19 μL/min.

Experiment of thermal responsiveness

The thermal responsiveness of the spiral-shaped hydrogel was observed by heating with a hotplate from 23 to 50 °C in a 1 M CaCl2 solution. The temperature of the CaCl2 solution was confirmed with the thermometer (PT-7LD, Optex). An axial direction shrinkage ratio, $R_{\mathrm{axial}} = p(t)/p(0)$, and cross-sectional direction, using $R_{\mathrm{cross}} = D_{\mathrm{spiral}}(t)/D_{\mathrm{spiral}}(0)$ were measured (t is the time of measurement and 0 represents the initial state; Fig. 5.1 (b)). In addition, I evaluated a pitch angle change, $\Delta\alpha = \alpha(t) - \alpha(0)$, where pitch angle was calculated using $\alpha(t) = \tan^{-1}(p(t)/2D_{\mathrm{spiral}}(t))$. The hydrogel's responsiveness was observed with a digital microscope (Keyence, VH-5500), and actuation was measured every 30 s, for 5 min.

By 4 cycles of heating (50 °C, 300 s) and cooling at room temperature (23 °C, over 300 s), the deformation, R, and the pitch angle, α, were measured (response speed is discussed in Appendix E). When cooling, the spiral-shaped hydrogel was placed into the 1M $CaCl_2$ solution, after it had settled at room temperature (approximately 23 °C). When comparing deformation ratios of double-layered spiral-shaped hydrogel, the results of cycle 1 were used. When comparing the pitch angle changes, results from cycle 1 were also used.

5.2.2 Shrinking/Swelling of the stimuli-responsive spiral-shaped hydrogel

Single-layered spiral-shaped hydrogel

The fabricated single-layered spiral-shaped hydrogel has a densely packed part and a varied pitch part (Fig. 5.2 (a)). After the shrinkage converged (heating duration: 180 s), the densely packed part ($\alpha(0) = 10°$) in the single-layered spiral-shaped hydrogel isotropically shrunk at a rate following $R_{\mathrm{axial}} \approx R_{\mathrm{cross}} \approx 0.7$, but this shrinkage did not change the shape of the spiral, given by $\Delta\alpha = -0.14°$ (Fig. 5.2 (b)). The variable pitch part ($\alpha(0) = 12^{\circ}$) also isotropically shrunk ($R_{\mathrm{axial}} = 0.8$, $R_{\mathrm{cross}} = 0.6$, $\Delta\alpha = 3.0°$, Fig. 5.3 (a)). The pitch angle, α, of the densely packed part in the single-layered spiral-shaped hydrogel was approximately

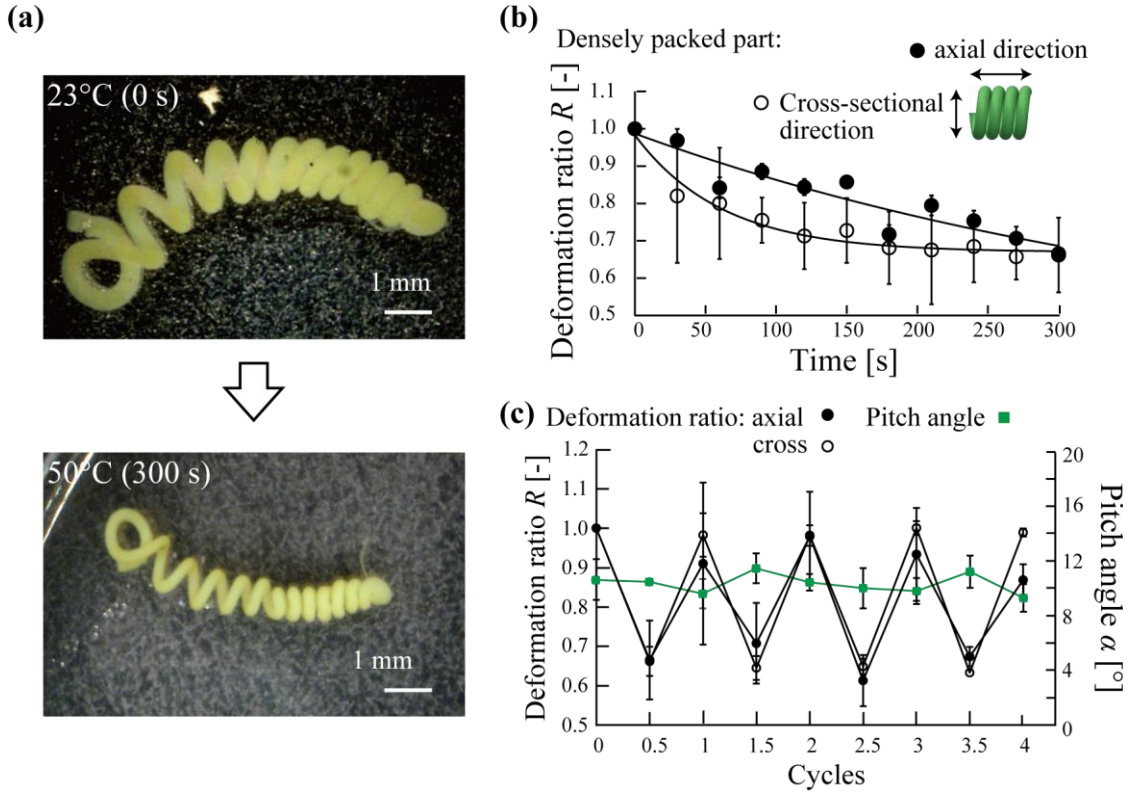

Figure 5.2 Shrinking/Swelling characteristics of single-layered spiral-shaped hydrogel (Densely packed part). (a) images of the shrinking behavior. (b) Shrinking characteristics of densely packed part when heated from 23ºC to 50ºC. (c) Results of repeatability for the shrinking/swelling behavior of densely packed part. Closed circles show the deformation ratio in the axial direction and open circles show the deformation ratio in the cross-sectional direction. Rectangles represent the pitch angle.

constant at ~10°, while the spiral compressed in the axial direction and cross-sectional direction ($R_{axial} \approx R_{cross} \approx 0.7$, Fig. 5.2 (c)). The pitch angle, α, of the variable pitch part was also approximately constant at ~15º, while compression occurred in the axial direction and cross-sectional direction ($R_{axial} \approx 0.72$, T $R_{cross} \approx 060$, Fig. 5.3 (b)). This responsivity revealed that the spiral's response to temperature was repeatable (Fig. 5.2 (c), Fig. 5.3 (b)). These results showed that single-layered spiral-shaped hydrogel shrunk isotropically while maintaining the shape of the spring (The pitch angle, α, was constant).

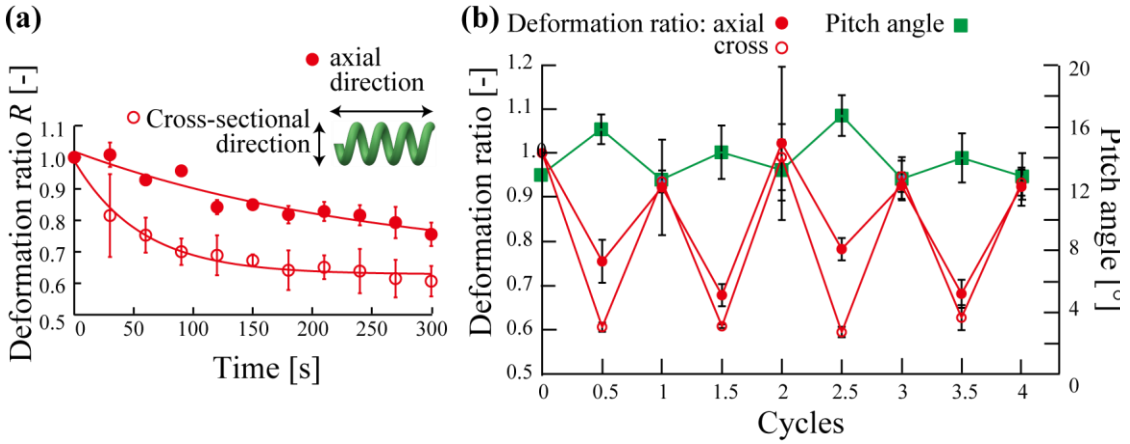

Figure 5.3 Shrinking/Swelling characteristics of single-layered spiral-shaped hydrogel (Variable pitch part). (a) Shrinking characteristics of variable pitch packed part when heated from 23ºC to 50ºC. (c) Results of repeatability for the shrinking/swelling behavior of variable pitch part. Closed circles show the deformation ratio in the axial direction and open circles show the deformation ratio in the cross-sectional direction. Rectangles represent the pitch angle.

Double-layered spiral-shaped hydrogel

Three types of spiral-shaped hydrogels with different pitches referred to as Double 1 ($p(0)$ = 258–296 μm), Double 2 ($p(0)$ = 820–970 μm) and Double 3 ($p(0)$ = 1620–2490 μm) (Fig. 5.4 (a)) were fabricated. Flow rates were 28.6 μL/min and 7.5 μL/min for stimuli-responsive and non-responsive layers, respectively. A fluorescent image of a formed double-layered spiral-shaped hydrogel (D_{gel} = 289 μm, D_{spring} = 1010 μm) showed that the hydrogel was clearly divided into two layers (the green part is the stimuli-responsive hydrogel layer; the red part is the non-responsive hydrogel layer; Fig. 5.4 (b)). In addition, the pitch of the double-layered spiral-shaped hydrogel also varied according to the buoyancy force.

Using these three types of double-layered spiral-shaped hydrogel, the degree of axial deformation and changes in pitch angle during 4 cycles of heating (50ºC, 300 s) (For example, Double 3: Fig. 5.4 (c)) and cooling (23ºC, over 300 s) were examined. The shrinkage of all double-layered spiral-shaped hydrogels occurred largely in the axial direction and converged

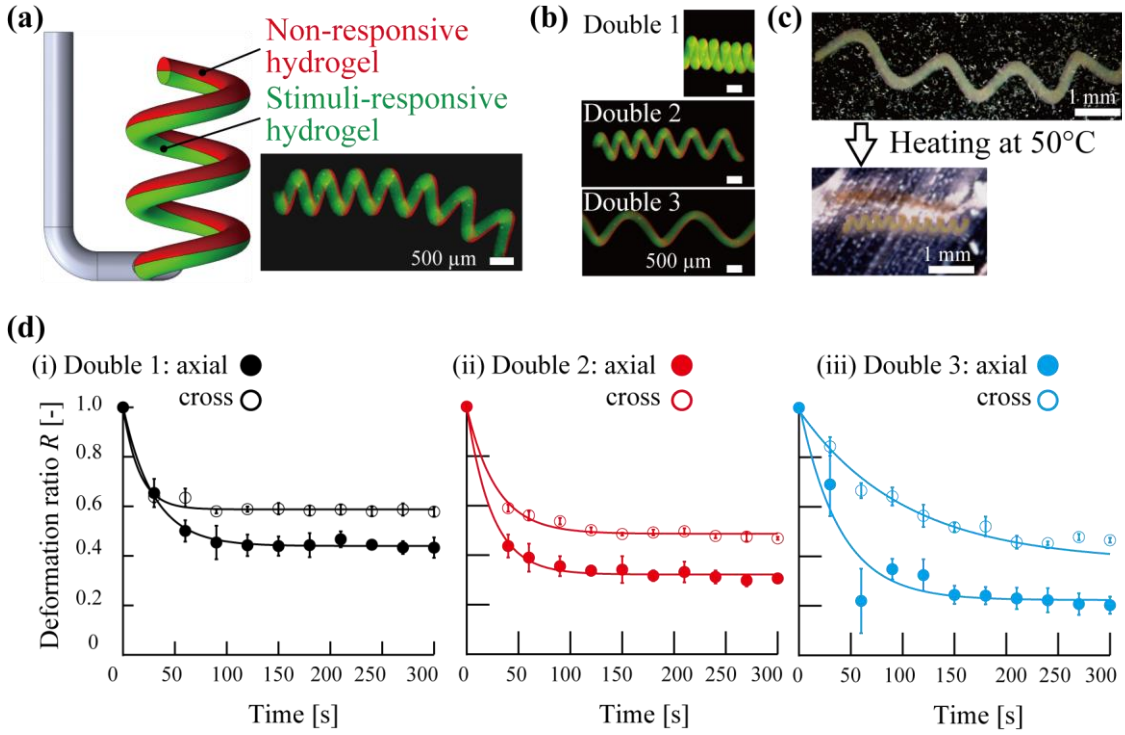

Figure 5.4 Shrinking/Swelling characteristics of double-layered spiral-shaped hydrogel. (a) Fabrication setup and fluorescent images of double-layered spiral-shaped hydrogel. (c) Responsivity of a double-layered spiral-shaped hydrogel (Double 3) heated at 50ºC. (d) Shrinking characteristics of double-layered spiral-shaped hydrogel with different pitches when heated from 23ºC to 50ºC. Closed circles show the deformation ratio in the axial direction and open circles show the deformation ratio in the cross-sectional direction: (i) Double 1, (ii) Double 2, and (iii) Double 3.

at approximately 100 s (Fig. 5.4 (d)). The same behavior was observed in the cooling process. Here, deformation ratios for axial directions, R_{axial}, were smaller than those for cross-sectional directions, R_{cross}. Moreover, although the pitch angle of the Double 1 spiral was approximately constant (α = 6.3–9.8°) (Fig. 5.5, black), those of the Double 2 and Double 3 springs changed drastically (Double 2: α = 13–23°; Fig. 5.5, red; Double 3: α = 19–43°; Fig. 5.5, blue). These results indicate that springs were largely compressed as pitch increased.

It is compared that the deformation ratios, R, and pitch angle changes, $\Delta\alpha$, for all single-layered (Fig. 5.2 (a)) and double-layered (Fig. 5.4 (b)) spiral-shaped hydrogel to

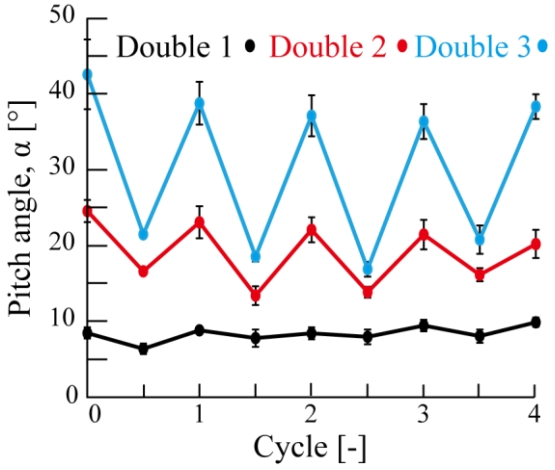

Figure 5.5 Repeatability of pitch behavior for double-layered spiral-shaped hydrogel.

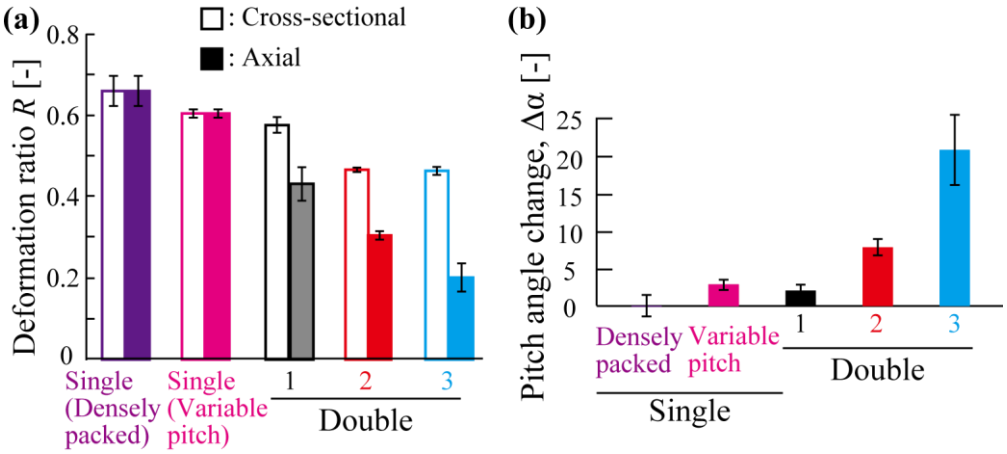

Figure 5.6 Comparing deformation behavior. (a) Deformation ratio after heating at 50ºC (Cycle 1). (b) Pitch angle change, $\Delta\alpha = \alpha\,(300) - \alpha\,(0)$ (Cycle 1).

analyze how shrinking behavior was affected by different spiral conditions. Both deformation ratios of the densely packed and variable pitch single-layered spiral-shaped hydrogel were small (Single_densely: $R_{axial} = 0.7 \pm 0.04$; $R_{cross} = 0.7 \pm 0.04$, Single_variable: $R_{axial} = 0.6 \pm 0.01$; $R_{cross} = 0.6 \pm 0.01$, Fig. 5.6 (a)). In contrast, the Double 1-3 spirals were mainly compressed in their axial direction, with larger shape changes than those of the single-layered spiral-shaped hydrogel (Double 1: $R_{axial} = 0.4 \pm 0.04$, $R_{cross} = 0.6 \pm 0.02$. Double2 $R_{axial} = 0.3 \pm 0.01$; $R_{cross} = 0.5 \pm 0.01$, Figure 4f). Double 3 that had the largest pitch and the largest axial deformation ($R_{axial} = 0.2 \pm 0.03$; $R_{cross} = 0.5 \pm 0.01$, Fig. 5.6 (a)). In general, the change in

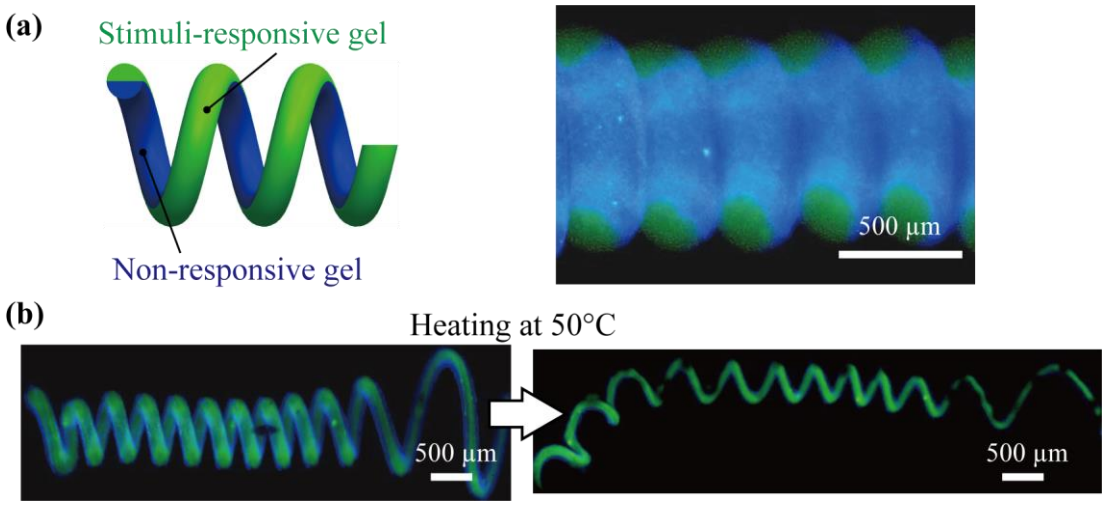

Figure 5.7 Expansion deformation of double-layered spiral-shaped hydrogel. (a) Schematic illustration and fluorescent image of the double-layered spiral-shaped hydrogel. (b) Fluorescent image of expansion in the double-layered spiral-shaped hydrogel (Double 4).

pitch angle, $\Delta\alpha$, of the single-layered spiral-shaped hydrogel was small, regardless of the pitch size (Fig. 5.6 (b)). The $\Delta\alpha$ of the densely packed double-layered spiral-shaped hydrogel (Double 1) was also slight; however, Double 2 and Double 3 had a significant $\Delta\alpha$ as the pitch of the spring increased. These results proved that the compression of the stimuli-responsive spiral-shaped hydrogel can be realized by pattering the shrink part in the spiral and that the compression degree of a double-layered spring depends on the initial pitch, $p(0)$. These deformation behaviors have a similar tendency to the simulation results conducted in Chapter 4.

In addition to compression of spiral-shaped hydrogel triggered by thermal stimuli, expansion of a spiral-shaped hydrogel in the axial direction was achieved by using a double-layered spiral-shaped hydrogel whose boundary between the two layers was parallel to the axial direction of the spring (Double 4, $\alpha = 11^{\circ}$) (Fig. 5.7 (a)). The outer layer (labeled green) of the spiral was a stimuli-responsive part that could shrink in response to temperature changes, while the inner layer (labeled blue) of the spiral was a non-responsive part. The pitch angle of Double 4 increased with heating (50ºC, 300 s, Fig 5.7 (b)), while the outside of the spring shrank. The shrinkage of cross-sectional direction is converged at approximately

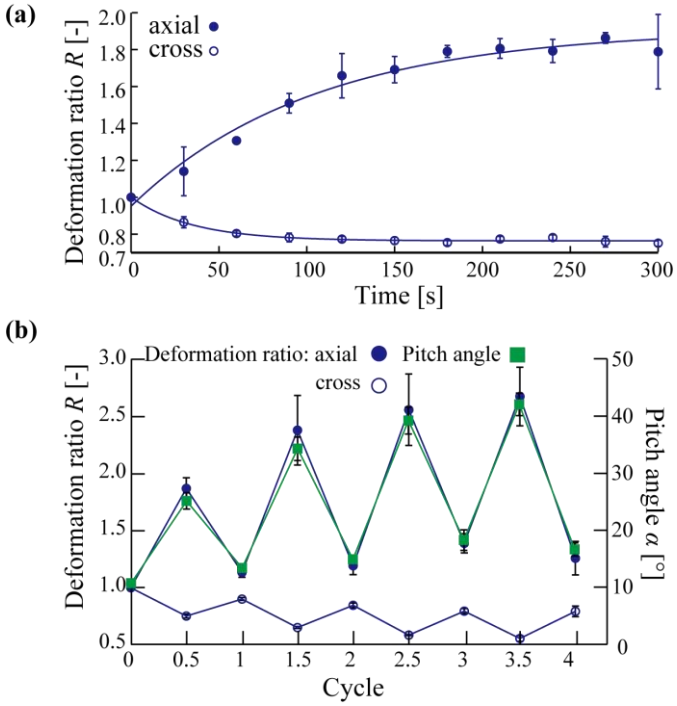

Figure 5.8 Expansion deformation of outside patterned spiral-shaped hydrogel. (a) Expansion characteristics of outside patterned spiral-shaped hydrogel when heated from 23ºC to 50ºC. (b) Repeatability of pitch behavior in outside patterned spiral-shaped hydrogel.

100 s, while the shrinkage of axial direction is converged at approximately 300 s. The deformation ratios, R_{axial} (Fig. 5.8 (a), closed circle), increased, while $R_{cross\_sectional}$ (Fig. 5.8 (a), open circle) decreased (R_{axial} = 2 ± 0.20; $R_{cross\text{-}sectional}$ = 0.8 ± 0.02). The shape of Double 4 was largely expanded toward the axial direction during deformation (α = 11-42˚, Fig. 5.8 (b)). These results showed that shrinkage of the stimuli-responsive p(NIPAM-co-AAc) was converted to large expansion movement in the axial direction. These results showed that the deformation behavior of the outside pattern was also similar to the simulation results.

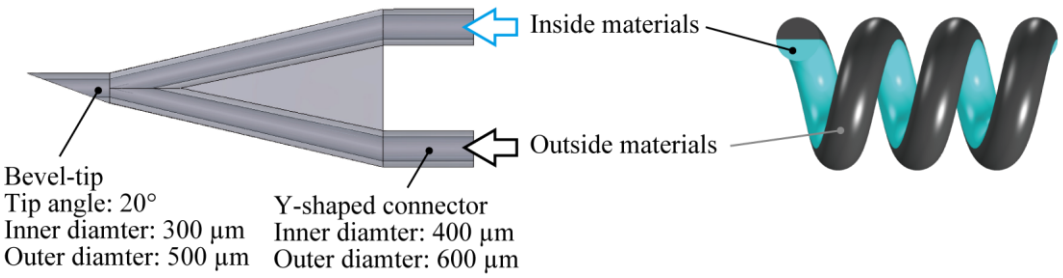

Figure 5.9 Fabricated bevel-tip with Y-shaped connector.

5.3 Propulsion velocity change of the double-layered spiral-shaped micro-swimmer

5.3.1 Fabrication of double-layered spiral-shaped micro-swimmer

To form double-layered spiral-shaped micro-swimmers, 6.8% (w/w) magnetic nanoparticles encapsulated 2.6%(w/w) Poly (N-isopropyl acrylamide-co-acrylic acid) (p(NIPAM-co-AAc); SIGMA-ALDRICH, 741930) + 0.4% (w/w) NaAlg as a stimuli-responsive layer, and 3% (v/v) fluorescent microbeads (yellow-green fluorescent, 0.2 μm; Life Technologies , F8811) encapsulated 1.0% (w/w) NaAlg + 1.0% (w/w) propylene glycol alginate (PGAlg; Wako, 165–17415) as a non-responsive layer were used.

The magnetic encapsulated p(NIPAM-co-AAc) + NaAlg. and the NaAlg. + PGAlg. were easy to mix in a micro-fluidic device, and thus they are required to separate until ejected. To separate them, a bevel-tip capillary with a Y-shaped connector was fabricated through two-photon stereolithography (Nanoscribe) (Fig. 5.9). The tip angle of the bevel-tip was 20º and the inner diameter was 300 μm (The outer diameter was 500 μm). The inner diameter and outer diameter of the Y-shape connector were 400 μm and 600 μm, respectively. By changing the pre-gel solution flowing into each inlet, the inside and outside patterns can be controlled.

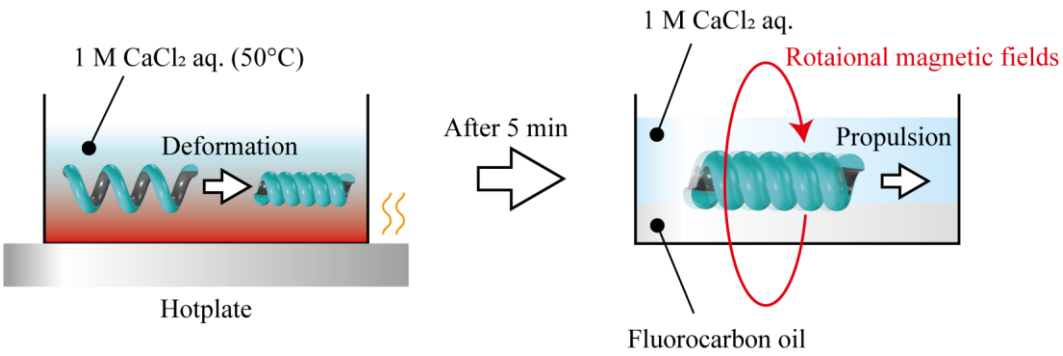

Figure 5.10 Experimental setup for observing the propulsion velocity change.

5.3.2 Experimental setup

For observing the temperature dependence of the final pitch angle, fabricated bi-layered Spiral swimmers were heated with a hotplate (As One, ND-1) from 26°C to 46°C in 1M $CaCl_2$ solution. The temperature of the $CaCl_2$ solution was confirmed with a thermometer (Optex, PT-7LD). The Spiral swimmer's responsiveness was observed with a digital microscope (Keyence, VH-5500), and final pitch angles were measured after 2 minutes of heating. To analyze the deformation of our double-layered spiral-shaped micro-swimmer, I compared the measured final pitch angle, α_f, with the calculated values on the basis of the simulation results.

For propulsion force change observation, the fluorocarbon oil (Single Cell Technology, Pico-Surf™ 1 (2% (w/w) in Novec™ 7500)) was used for decreasing friction (Fig. 5.10). The swimming behavior of the double-layered spiral-shaped micro-swimmer before deformation was conducted at room temperature (20°C). The rotational magnetic field (10 mT, 5Hz) was applied. The setup for applying magnetic fields was the same as Chapter 3.4. The double-layered spiral-shaped micro-swimmers propelled on the fluorocarbon oil. After heated the double-layered spiral-shaped micro-swimmers at 50°C for 5 minutes, the swimming behavior of the deformed double-layered spiral-shaped micro-swimmer was observed. To observe the propulsion velocity change, fabricated double-layered spiral-shaped micro-swimmers were placed into a chamber filled with 1 M CaCl2 solution

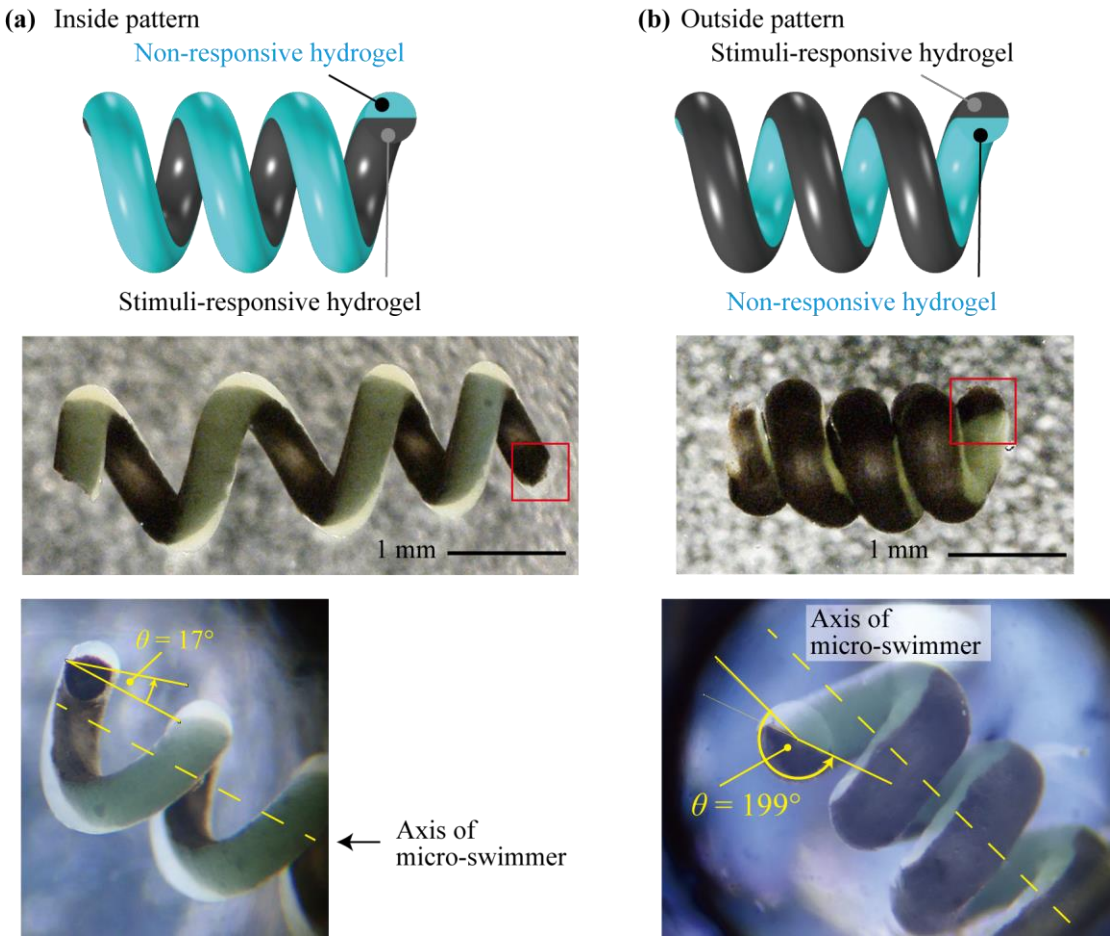

Figure 5.11 (a) Fabricated inside pattern micro-swimmer. (b) Fabricated ouside pattern micro-swimmer.

(experimental conditions: Re = 0.095–0.537) and the rotational magnetic field (10 mT, 5Hz) was applied.

5.3.3 Results

By adjusting the direction of the laminar flow pattern to the bevel-tip capillary, an inside pattern spiral swimmer (θ = 17°, α_i = 32°) and outside pattern spiral swimmer (θ = 199°, α_i = 21°) were fabricated (Fig. 5. 11 (a)). By applying temperature stimuli (26–46°C), the inside and outside pattern spiral-shaped micro-swimmers gradually deformed to expand and to contract, respectively, with increasing temperature (Fig. 5.12 (a)). These results

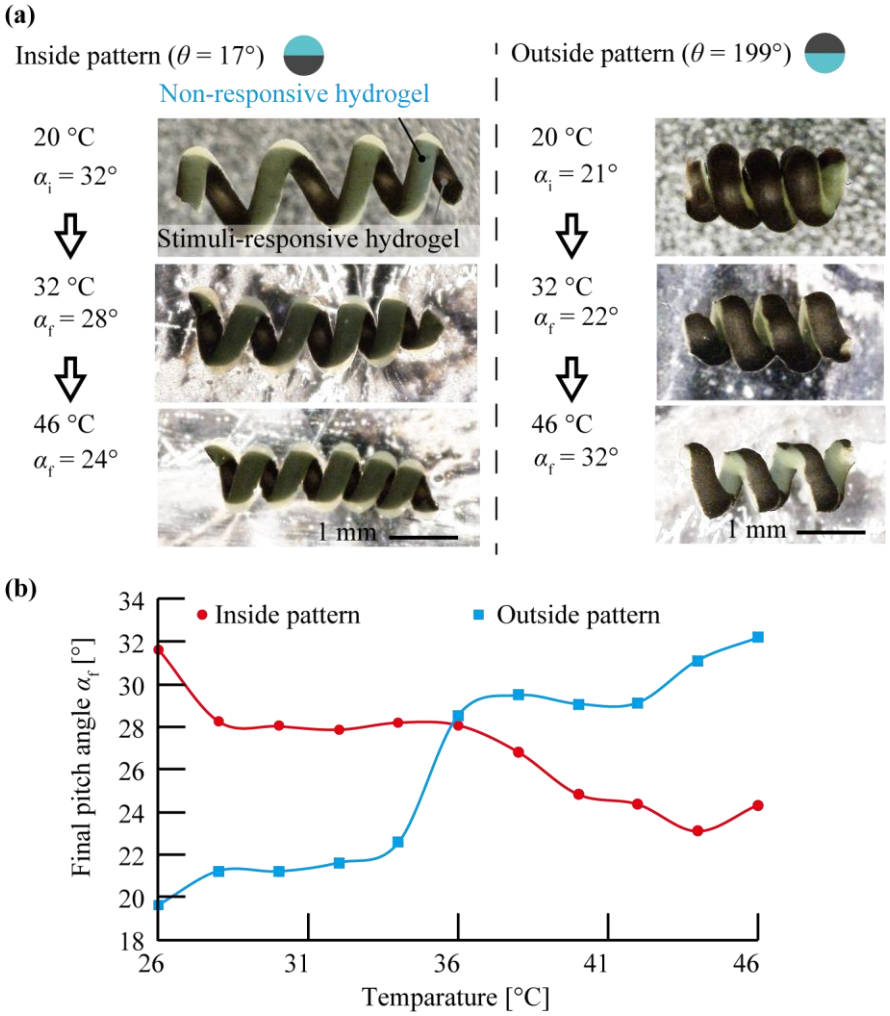

Figure 5.12 (a) Deformation of the inside pattern spiral-shaped micro-swimmer (left) and the outside pattern spiral-shaped micro-swimmer (right). (b) The relationship between the final pitch angle, α_f, and the surrounding temperature.

indicate that the final pitch angle, α_f, could be controlled by the strength of the external stimuli.

To analyze the deformation of the double-layered spiral-shaped micro-swimmer, it is compared that the measured final pitch angle, α_f, with the calculated values on the basis of the simulation results (The patterning angle of inside pattern and outside pattern is $\theta = 0$ and 200, respectively. Table 5.1). The final pitch angle of the inside pattern spiral swimmer eventually reached 24° at 46°C, which was close to the simulation results ($\alpha_f = 22°$, Fig. 5.12 (b), red circles). On the other hand, the outside pattern spiral swimmer expanded (Fig. 5.12

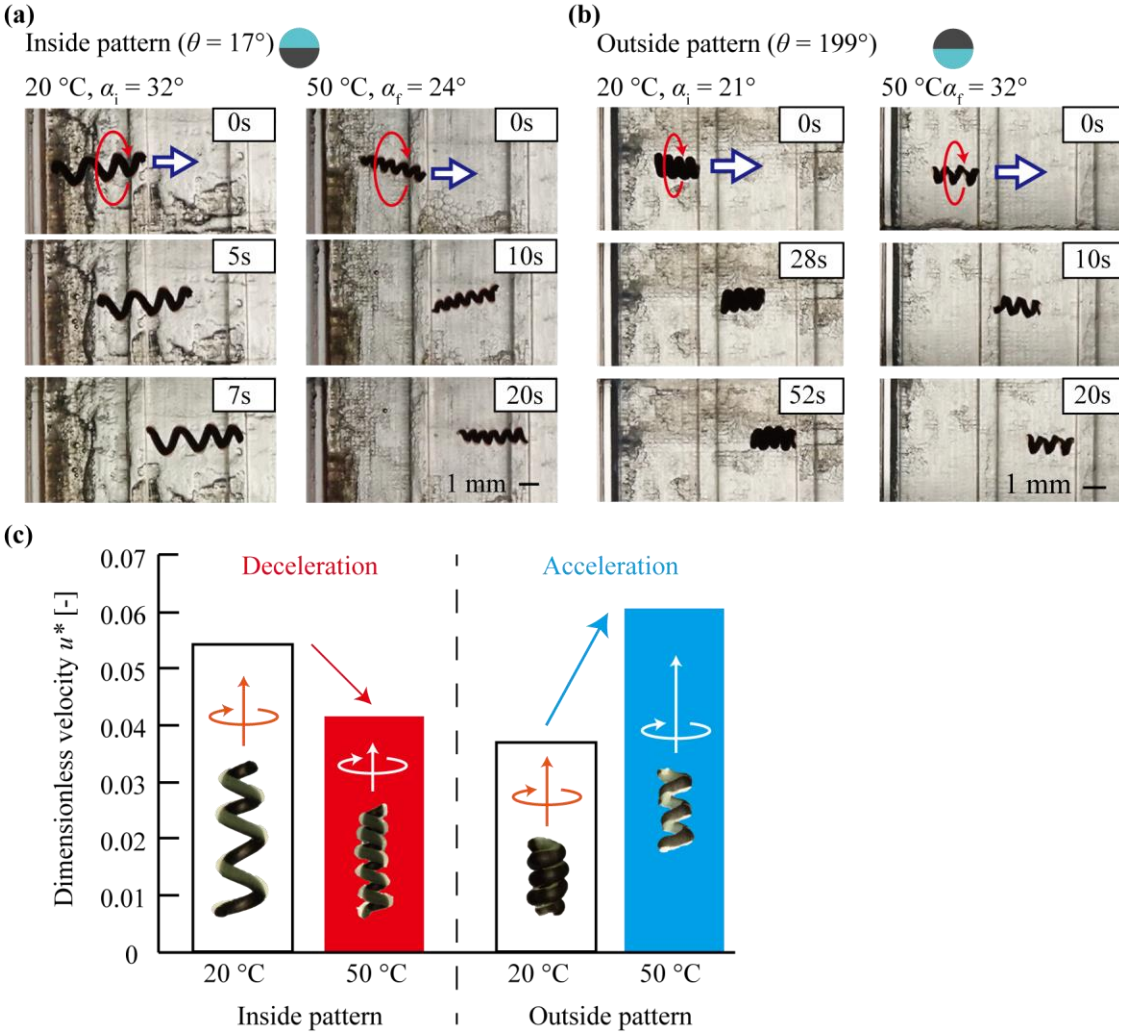

Figure 5.13 Propulsion velocity control by detecting the surrounding environment. (a) The swimming behaviors of the inside pattern spiral-shaped micro-swimmer. (b) The swimming behaviors of the outside pattern spiral-shaped micro-swimmer. (c) The dimensionless velocity change of the inside pattern spiral-shaped micro-swimmer and the outside pattern spiral-shaped micro-swimmer.

(b), blue squares). When a temperature stimulus of 46°C was applied, the final pitch angle of the outside pattern spiral-shaped micro-swimmer was 32º, that value was close to the simulation results (α_f = 38°). These results indicated that the deformation behavior was successfully simulated by the finite element simulations.

Table 5.1 Comaprison of experimental results and simulation results.

		Experiment		Simulation	
		Before	After	Before	after
Inside	α	32	24	30	22
	u^*	0.054	0.042	0.097	0.061
Outside	α	21	32	20	38
	u^*	0.037	0.061	0.074	0.120

Then, the propulsion velocity change by deforming the geometry of the bi-layered spiral swimmer caused by applying temperature stimuli was verified. The dimensionless velocity of the inside pattern spiral swimmer decreased from 0.054 (α_i = 32°) to 0.042 (α_f = 24°) as the geometry change was caused by the applied 50°C temperature stimuli (Fig. 5.13 (a) and (c), left). In contrast, the dimensionless velocity of the outside spiral swimmer increased from 0.037 (α_i = 21°) to 0.061 (α_f = 32°) (Fig. 5.13 (b) and (c), right). The measured dimensionless velocity u^* of each condition was smaller than the dimensionless velocity of simulation results because the simulation results were calculated by Equation (3.7). As discussed in Section 3.4.3, it is considered that the resistive force theory is true only for Re = 0, and small inertial effects still occur depending on the size and velocity of the spiral-shaped micro-swimmer. These acceleration and deceleration behaviors had tendencies similar to those of the simulation results (Fig. 4.7 (c)). The actual velocity showed a similar trend. The actual velocity of the inside pattern swimmer decreased from 424 μm/s to 257 μm/s, and the actual velocity of the outside pattern swimmer increase from 96 μm/s to 200 μm/s. Therefore, these results indicate that the propulsion velocity of spiral swimmers can be autonomously controlled by changing the geometry of the spiral swimmer in response to the surrounding stimuli.

Finally, the dynamic motility changes of micro-swimmer responding to the external environment are discussed in the 1D model. In order to detect the external environment and dynamically change their motion, the deformation of the micro-swimmer must be completed

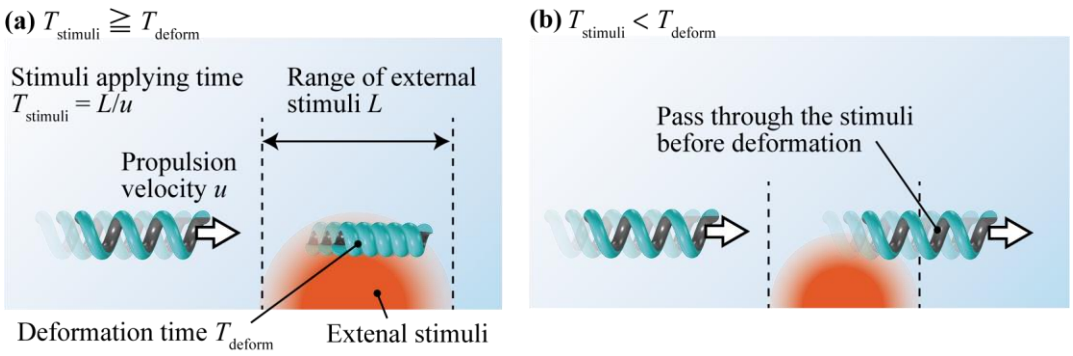

Figure 5.14 The dynamic motility change of micro-swimmer. (a) When $T_{stimuli} \geq T_{deform}$, the micro-swimmer was fully deformed. (b) When $T_{stimuli} < T_{deform}$, the micro-swimmer pass through the stimuli before deformation.

during the external stimuli is applied to the micro-swimmer. The time during the external stimuli was applied (a stimulus applying time, $T_{stimuli}$) and the time required for completing the deformation (a deformation time, T_{deform}) was compared (Fig. 5.14). When $T_{stimuli} \geq T_{deform}$, the micro-swimmers could change their motility by sensing the external environment (Fig. 5.14 (a)). On the other hand, the micro-swimmer pass through the external stimuli before changing their motility when $T_{stimuli} < T_{deform}$ (Fig. 5.14 (b)). In this study, the ratio of $T_{stimuli}$ and T_{deform}, which represent the responsivity of the micro-swimmer, was defined as

$$T_{res} = \frac{T_{stimuli}}{T_{deform}}, \tag{5.1}$$

and the micro-swimmer could change their motility during applying stimuli when $T_{res} \geq 1$. The stimuli applying time, $T_{stimuli}$, is determined by the propulsive velocity of the micro-swimmer, u, and the range of the external stimuli, L, in the form $T_{stimuli} = u/L$. Since the deformation time, T_{deform}, depends on the volume change of the stimuli-responsive hydrogel, it can be regarded as the response time of the stimuli-responsive hydrogel, τ. The response time, τ, was written as Equation (2.22). Thus, The condition of whether the micro-swimmer could change their motility by sensing external stimuli is expressed in the form

$$T_{res} = \frac{L}{u\tau} \geq 1. \tag{5.1}$$

Then, the responsivity of the micro-swimmer is discussed based on the results obtained from the experiments. By the results of 5.2.2, the response time, τ, was approximately 100 s when the diameter of gel was approximately 200 μm. In the case of inside pattern spiral-shaped micro-swimmer, the propulsion velocity before deformation was u = 424 μm/s. When the range of applying the external stimulus is more than 42.4 mm, the inside pattern spiral-shaped micro-swimmer can change the propulsive velocity by sensing the external stimulus. The length of the inside pattern micro-swimmer was approximately 4.2 mm, thus the stimuli length of 10 times the total length of the micro-swimmer was required to sense the external environment. The propulsion velocity, u, and the response time, τ, were depending on the scale of the micro-swimmer ($u \propto D_{\text{spiral}}$, $\tau \propto a^2$). Therefore, miniaturizing the micro-swimmer could be a powerful approach to realize the high responsivity of micro-swimmers.

5.4 Conclusion

Compressive and expanding actuation of double-layered spiral-shaped hydrogel with large deformations were achieved. The deformation ratio of double-layered spiral-shaped hydrogel could be further magnified by optimizing thicknesses and stiffness of both stimuli-responsive and non-responsive layers.

The proposed fabrication strategy for spiral-shaped hydrogel fully depended on the peripheral gelation of the outer calcium alginate[63]. Because p(NIPAm-co-AAc) cross-linked with Ca^{2+}, similar to NaAlg, was used, the responsiveness was limited to temperature and pH. However, by creating coaxial laminar flow in the bevel-tip capillary, spiral-shaped hydrogels encapsulating various functional materials inside their cores could be formed. It is expected that spiral-shaped micro-swimmer with various types of sources could be fabricated using different stimuli-responsive materials by varying pH, light, and chemicals, thereby expanding the applicability of the spiral-shaped micro-swimmer to practical applications.

One of the notable potentials of spiral-shaped micro-swimmer is that the propulsion velocity is controlled by the applied stimuli because the geometry of the spiral-shaped body gradually changes depending on the strength of the surrounding stimuli. The double-layered

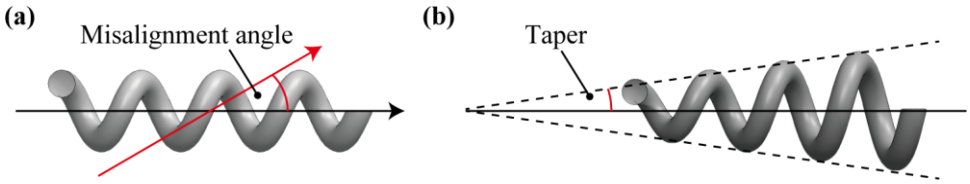

Figure 5.15 (a) Misalignment angle. (b) Taper of micro-swimmer.

spiral-shaped hydrogel could be repeatedly deformed, thus I think that the propulsion velocity could also be changed repeatedly because the propulsion velocity change is dependent on the geometry variation. Moreover, the acceleration and deceleration behaviors of the spiral-shaped micro-swimmers were designed by adjusting both the pitch angle, α, and the pattern angle, θ. From the deformation theory of double-layered structure, the ratio of the stimuli-responsive layer to the non-responsive layer is also considered to affect the amount of deformation. The amount of deformation increases as the stimuli layer thickness, reaching a maximum at a ratio of about 2. Therefore, proposed spiral-shaped micro-swimmers represent a significant new approach to realize autonomous propulsion velocity control. In contrast, spiral-shaped micro-swimmers also have limitations regarding to the scale of the swimmers. The scale of the swimmer is larger than the typical scale of microorganisms. Because spiral-shaped flagella have a strong advantage for swimming in fluid with a low Reynolds number, a scale of just about a couple micrometers for the micro-swimmers is preferred. The scale of the swimmer depends on the diameter of the bevel-tip capillary; thus, it is considered that smaller swimmers could be fabricated by using a bevel-tip capillary with a diameter in the tens of micrometers.

In this study, the wobbling of spiral-shaped micro- swimmers to the perpendicular direction of propulsion direction was observed. A misalignment angle was measured in the previous research, and it is decreased with a smaller pitch angle θ (Fig. 5.15 (a))[40]. When the pitch angle θ is smaller than 45°, the misalignment angle was smaller than 10°. In other words, if the helix shape has a constant diameter of the spiral, the effect of wobbling is considered to be small. In this study, it is thought that the cause of the wobbling was due to the difference in the diameter of spiral, D_{spiral}, because the misalignment angle was increase as the taper of micro-swimmer increase (Fig. 5.15 (b))[98]. Therefore, if a diameter of spiral,

D_{spiral}, with a small difference and a small pitch angle ($\alpha < 45°$) is used, there is no need to consider the effects of wobbling.

In conclusion, the soft spiral-shaped micro-swimmer for autonomous swimming control by detecting surrounding environments was demonstrated. The dimensionless velocity of the fabricated double-layered spiral-shaped micro-swimmer was successfully changed by applying the thermal stimuli. Double-layered spiral-shaped micro-swimmers could be characterized by using the ability to encapsulate various functional materials including other stimuli-responsive hydrogels. Moreover, the complex compartmentalization of the spiral swimmer characterized by a laminar flow inside the capillary can also contribute to the optimization of their internal structure and functionality enhancement. The proposed spiral-shaped micro-swimmer can open new avenues for various microscale biochemical applications such as autonomous soft robots and soft micro-probes for the intricate, minuscule environment.

Chapter 6
Micro-robots integrated with photonic colloidal crystal hydrogel

6.1 Introduction

Stimuli-responsive hydrogels are attractive materials for realizing the biochemical sensors of micro-robots because stimuli-responsive hydrogels1 shrink and swell in response to the intensity of external stimuli such as temperature, light, pH, and chemical substance. While the stimuli-responsive hydrogel has attractive functions. there are grand challenges to apply the stimuli-responsive hydrogel for the components of micro-robots: (i) It is difficult to obtain the information by the volume change of the stimuli-responsive hydrogel and (ii) It is difficult to integrate the stimuli-responsive hydrogel into the micro-robots because water inhibit am adhesion between the stimuli-responsive hydrogel and other materials.

For applying these stimuli-responsive hydrogels for biochemical sensors, it is necessary to convert the external stimulus to another type of information. A photonic colloidal crystal hydrogel, in which monodispersed colloidal particles are regularly arranged, is expected to be a powerful tool for sensors based on a stimuli-responsive hydrogel. The photonic colloidal crystal hydrogel reflects visible-light wavelength through Bragg's diffraction. In this hydrogel, the intensity of the stimulus can be converted to visible color information by the change in the distance between the colloidal particles. Thus, it is possible to obtain sensing information with the naked eye.

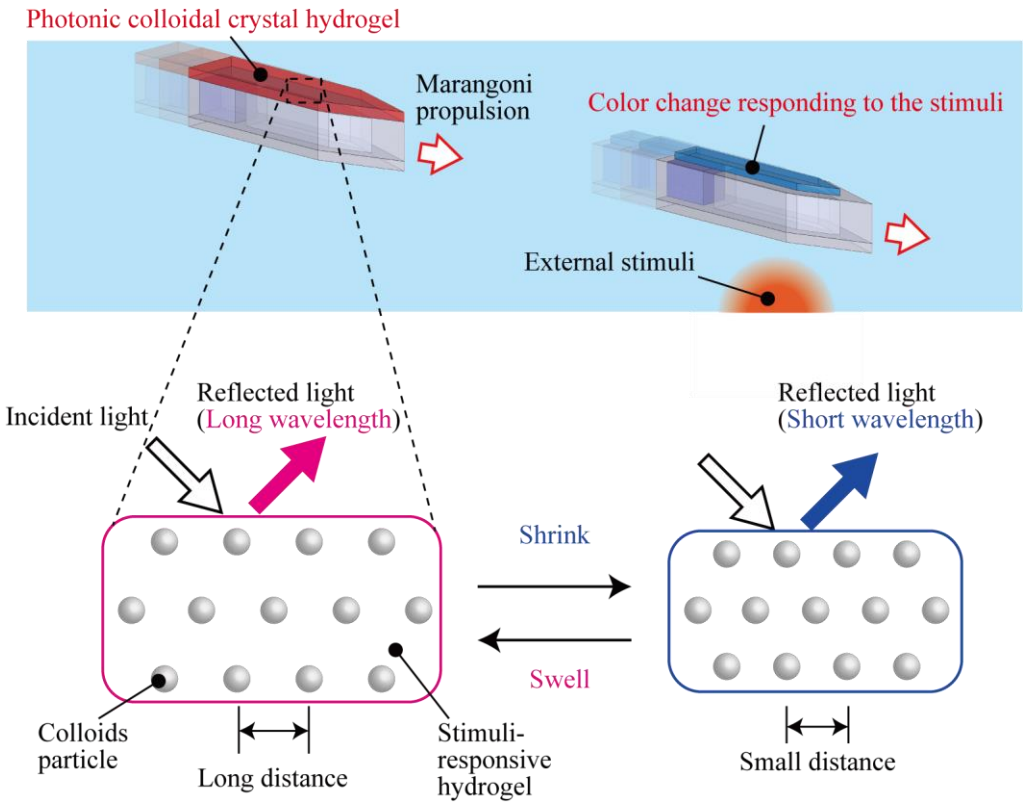

Figure 6.1 Brief concept of micro-robots integrated with photonic colloidal crystal hydrogel for converting the environmental stimuli into the visible-light wavelength change.

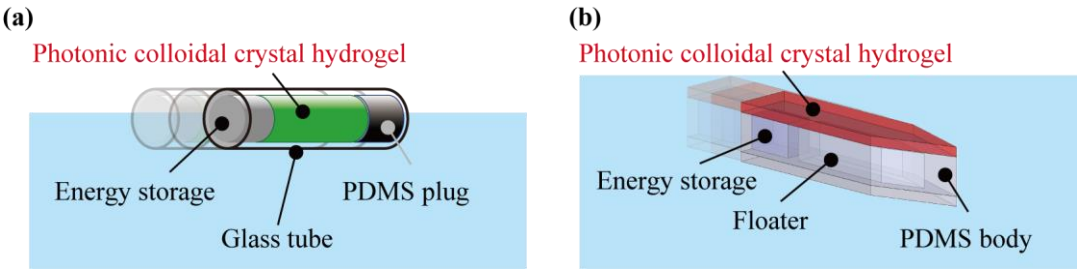

Figure 6.2 Proposed micro-robots integrated with photonic colloidal crystal hydrogel. (a) Tubular-shaped micro-robots. (b) Rocket-shaped micro-robots.

In previous research, the micro-robots patterned with photonic colloidal crystal hydrogel by photolithography were proposed[43][99]. However, these micro-robots could not be applied for sensing functions because the structural color of micro-robots was changed

during the propulsion with the deformation of its geometry. Thus, it is required to separate the driving function and the sensing function. Here, it is proposed that novel design of micro-robots integrated with photonic colloidal crystal hydrogel (Fig. 6.1). The photonic colloidal crystal hydrogel was placed on the micro-robots body. By this design, the sensing function independent of the propulsion function can be realized. For driving method, the Marangoni propulsion was used, because of fewer limitations of the driving environment and energy storage. In this research, two types of micro-robots were proposed: tubular-shaped micro-robots (Fig. 6.2 (a)) and rocket-shaped micro-robots (Fig. 6.2 (b)). The main components of micro-robots were a body, a photonic colloid crystal hydrogel as a environmental sensor, and a hydrogel as energy storage filled with ethanol. When floated on the water, the ethanol filled in the energy storage is released by spontaneous diffusion. The released ethanol rises to the air-water interface by buoyancy and generates surface tension asymmetry because of the presence of ethanol lowers the surface tension of water. The propulsion of micro-robots by interfacial flows caused by surface tension gradients, a phenomenon is known as the Marangoni effect. To increase the diffusion time of ethanol, the gel is filled with ethanol for propulsion. In addition to the propulsion system, the color of photonic colloid crystal hydrogel on the micro-robots is changed by thermal stimuli. In this research, *N*-isopropyl acrylamide (NIPAm) that has thermal responsibility and *N*-(Hydroxymethyl) acrylamide (NMAm) that has the ethanol responsivity were used.

6.2 Outline

In this chapter, the characteristics and fabrication mechanism of a photonic colloidal crystal were first introduced. Second, a floating theory of micro-robots and a Marangoni propulsion were described. Third, the fabrication methods of micro-robots integrated photonic colloidal crystal hydrogel were described. Forth, the visible color-change responding to environmental temperature and ethanol concentration and propulsion of micro-robots were demonstrated. Finally, the design and fabrication method of micro-robots integrated photonic colloidal crystal hydrogel was concluded by the conducted experiments

and the outlook of this development.

6.3 Photonic colloidal crystal

Regularly arranged colloidal particles reflect the light of a specific wavelength by Bragg diffraction (Fig. 6.3 (a)). The peak wavelength λ of the reflected wavelength is expressed the following,

$$\lambda = 2dn\sin\theta \tag{6.1}$$

where d is the distance of the colloid particles, n is their effective refractive index, θ is the angle of the incident light.

As a method to align the colloidal particles, vaporization of solvent[100][101] and desalting by using ion exchange resin[55] are proposed. In this research, the desalting method was used for preparing the photonic colloidal crystal hydrogel. In the desalting method, the colloidal particles are arranged in the pre-gel solution by an electric double layer (Fig. 6.3 (b)) (Detail is described in Appendix F). The arraying method using an electric double layer of silica colloidal particles was described. The surface of silica colloidal particles is covered with silanol groups. Normally, the silanol groups are electronegative in solution such as

$$\text{Si-OH} + \text{OH}^- \rightarrow \text{Si-O}^- + \text{H}_2\text{O}. \tag{6.2}$$

The ionized H^+ is attracted to the colloidal particles by electrostatic interaction, while it tends to distribute uniformly by thermal motion. Therefore, H^+ is distributed in the vicinity of the colloidal particles while diffusing, which is called the electric double layer. The ions present in the solution are exchanged to H^+ and OH^- when the colloidal solution is mixed with the ion exchange resin and desalted. The concentration of ions in the colloidal solution decreases since the exchanged H^+ and OH^- become water (H_2O) molecules in the solution. As a result, the ions in the vicinity of the colloidal particles have a stronger force to diffuse uniformly in the solution, thus increasing the thickness of the electric double layer. The increasing thickness of the electric double layer causes strong repulsion to act between the particles, and

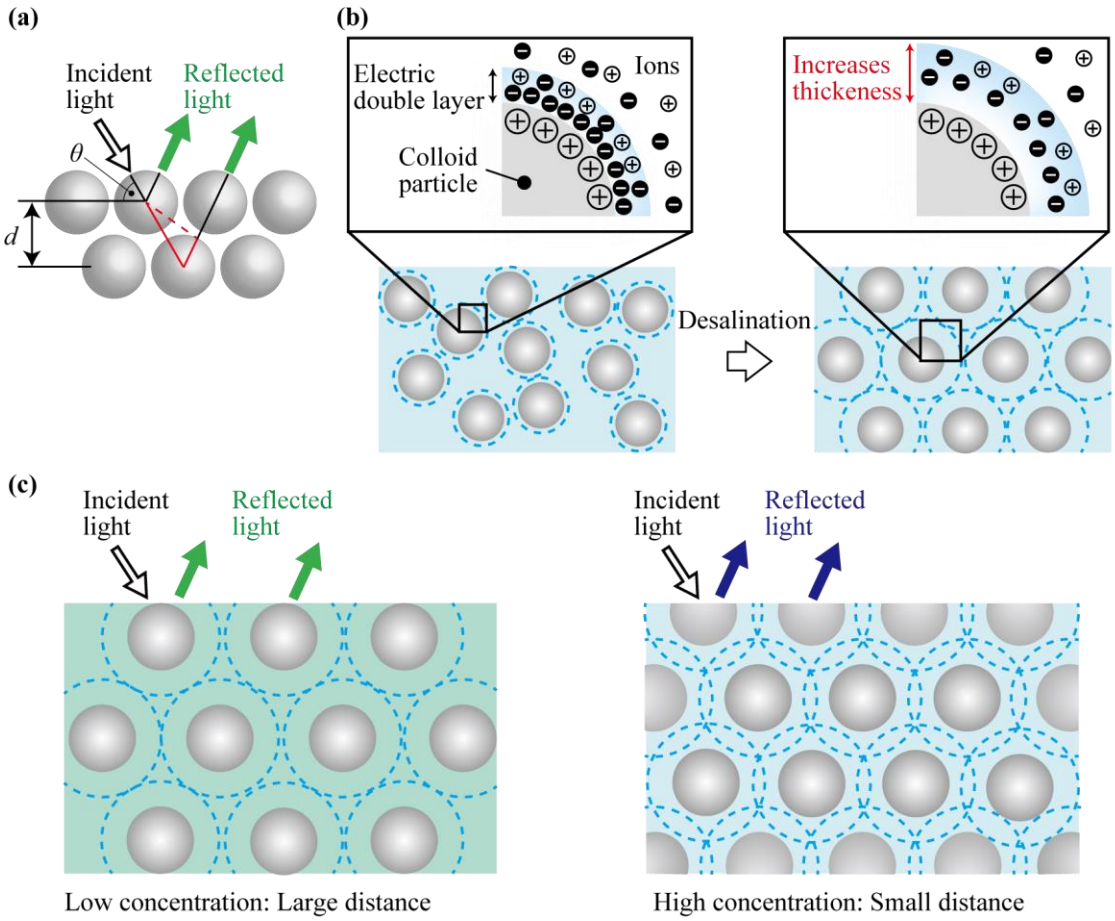

Figure 6.3 Photonic colloidal crystal. (a) Schematic image of bragg diffraction. (b) The colloidal particles are arranged by the electric double layer. (c) The distance of particle is dependent on the concentration of the colloidal particles.

the colloidal particles arrange themselves in a regular pattern. The distance of the colloid is determined by the balance between the thickness of the electric double layer and the colloidal particle concentration (Fig. 6.3 (c)). In a previous study, it was reported that the crystal structure of colloidal crystals produced in a pre-gel solution by desalting was a face-centered cubic (fcc) lattice[55]. Since silica colloids are oriented in the (1 1 1) plane of the close-packed fcc lattice the plane spacing d is expressed using the particle size D in the form

$$d = \frac{\sqrt{6}}{3} D. \tag{6.3}$$

In the case of an fcc lattice with a close-packed structure, the volume fraction is 74%, so the average refractive index n_c is expressed as

$$n_c = \sqrt{n_p^2 \times 0.74 + n_a^2 \times 0.26} \tag{6.4}$$

where n_p is the refractive index of colloidal particles and n_a is the refractive index of substances that fill the voids of photonic colloidal crystals. By equations (6.1), (6.3), and (6.4), the value of the peak λ of the wavelength reflected from the crystal increases with the size D of the particles and with the refractive index of the material filling the voids.

6.4 Float mechanism of micro-robots

An object floating on the surface of the water is subjected to two main forces from the water; surface tension and a buoyancy force. So, in this dissertation, these forces were considered to design the micro-robots.

6.4.1 Surface tension

The loading capacity of the tubular-shaped micro-robot is an important design parameter. In this section, a numerical model of the forces acting on the tubular-shaped micro-robot is described based on previous researches[102][28]. A two-dimensional model of the tubular-shaped micro-robot made by a hydrophobic material (ex. glass) was discussed (Fig. 6.4). It is assumed that the tubular micro-robots is a contact length c, a diameter of tubular-shape, r (Fig. 6.4 (a)). The vertical lift force, F, acting on the tubular-shaped micro-robot of a buoyancy force, F_b, and a force due to surface tension, F_s, is described as

$$F = F_b + F_s. \tag{6.5}$$

The buoyancy force, F_b, is deduced by integrating the vertical component of hydrostatic pressure, p, over the body area in contact with the water (Fig. 6.4 (b)). The force due to surface tension, F_s, is the vertical component of the surface tension, γ, along the constant perimeter. Moreover, E. H. Mansfield and J. B. Keller described that F_b and F_s are equal to

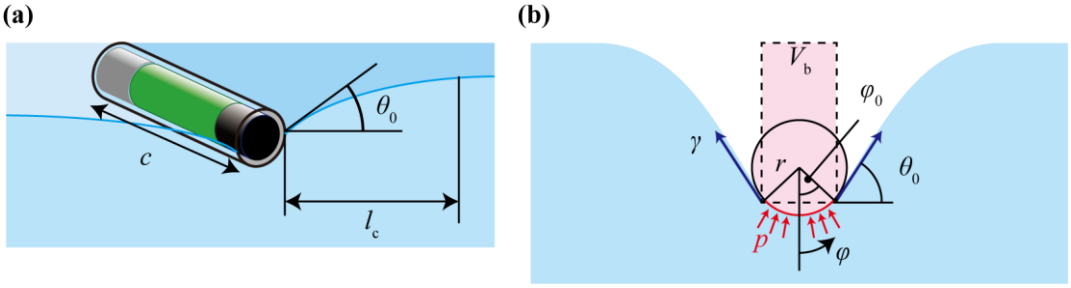

Figure 6.4 Parameters for the floating mechanisms. (a) The length of micro-robot. (b) The forces on the floating body.

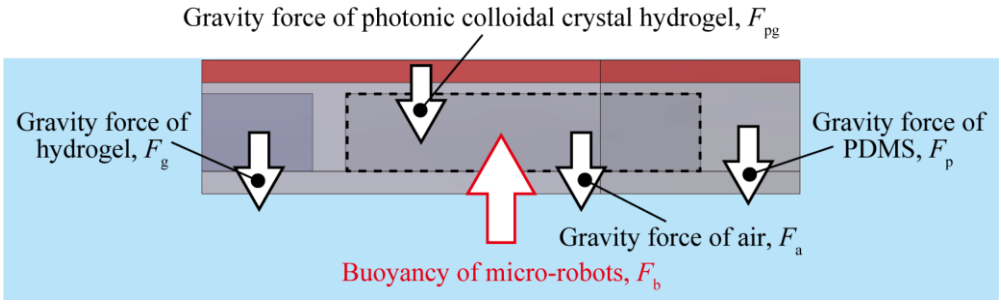

Figure 6.5 The forces related to the rocket-shaped micro-robot.

the weights of the fluid displaced inside and outside of the contact perimeter, respectively. Therefore, F_b and F_s are respectively described as

$$F_b = c\int_0^{\varphi_0} p\cos\varphi \cdot r d\varphi = \rho g V_b \quad . \tag{6.6}$$

$$F_s = 2\gamma c\sin\theta_0. \tag{6.7}$$

where V_b, φ_0, and θ_0 are a volume of water displaced above the meniscus, an arc angle, and an angle of tangency between the tubular shape and the water, respectively. Above all, when the gravity of the tubular-shaped micro-robots smaller than the vertical lift force $Mg < \rho g V_b + 2\gamma c \sin\theta_0$ (M is a weight of micro-robots), the tubular-shaped micro-robots can float. It is noted that the surface tension does not dependent on the diameter of tubular-shape, r, or the contact angle, θ_c. On the other hand, the buoyancy force, F_b, does depend on the diameter of the tubular shape. Thus, the force due to surface tension dominants over the buoyancy force when the diameter is small.

6.4.2 Buoyancy force

Next, the float mechanism of rocket-shaped micro-robots was discussed (Fig. 6.5). The buoyancy force is dominant because the rocket-shaped micro-robots are large, so the influence of surface tension can be ignored. The buoyancy of micro-robots, F_b, is equal to the weights of the fluid displaced. The rocket-shaped micro-robots were divided into four parts: the PDMS body, the photonic colloidal crystal hydrogel, the energy storage hydrogel, and the floater. So, the rocket-shaped micro-robots can float when the buoyancy exceeded the summarized gravity force of part as follows

$$F_b > F_p + F_{pg} + F_g + F_a, \quad (6.8)$$

where F_p, F_{pg}, F_g, and F_a are the gravity force of PDMS, gravity force of photonic colloidal crystal hydrogel, gravity force of hydrogel, and gravity force of air, respectively. The hydrogel highly contains water, thus the density of hydrogel was assumed to be equal to that of water, thus the equation (6.8) is rewritten as

$$V_b \rho_w g > V_p \rho_{PDMS} g + V_{pg} \rho_w g + V_g \rho_w g + V_a \rho_{air} g, \quad (6.9)$$

where V and ρ are the volume of each area and the density.

6.4.3 Marangoni propulsion

The mechanism of Marangoni propulsion can be better understood by considering a rectangular object as shown in Fig. 6.6. Suppose that ethanol is released on that left side and lowers the surface tension of the water. Then both the contact angle on the left side, θ_2, and the magnitude of the surface tension of the ethanol-water mixture, γ_2, are decreased. As a result, an asymmetry of the surface tension is induced, and the net propulsion force, F_{prop}, is applied toward the right side. Denoting the width of the rectangular object by w, the propulsion force is formulated as

$$F_{prop} = w(\gamma_1 \sin\theta_1 - \gamma_2 \sin\theta_2). \quad (6.10)$$

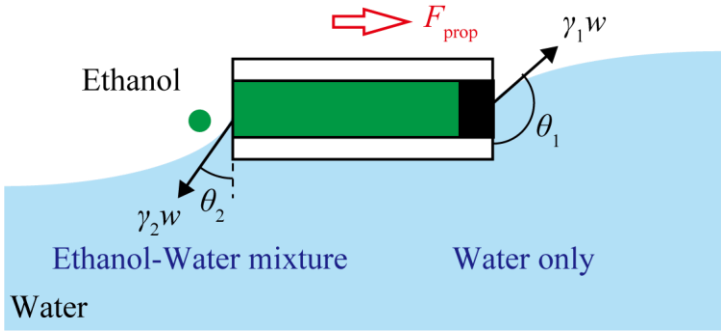

Figure 6.6 The principle of Marangoni propulsion in the rectangular object floating on water: Propulsion force: F_{prop}, width: w, surface tension: γ, and contact angle: θ.

A horizontal balance of force yields the resulting steady speed U. The propulsion force, F_{prop}, is balanced by the appropriate high Reynolds number drag force, $F_{drag} = \rho U^2 wd$, where wd is the relevant projection of the micro-robots submerged exposed are. The followed equation can be obtained;

$$U = \sqrt{\frac{\gamma_1 \sin\theta_1 - \gamma_2 \sin\theta_2}{\rho d}}. \quad (6.11)$$

Speed increases with a greater fore-aft difference in surface tension and contact angle. A lighter micro-robots leads to a smaller intrusion depth d and therefore faster speeds.

6.5 Tubular-shaped micro-robots

6.5.1 Preparation of photonic colloidal crystal hydrogel

In this study, two stimuli-responsive hydrogels were used; a *N*-isopropylacrylamide (NIPAm) as a thermal-responsive hydrogel and a *N*-(Hydroxymethyl) acrylamide (NMAm) as an ethanol-responsive hydrogel.

First, the preparation of NIPAm hydrogel with photonic colloidal crystal was described. A silica sol (SiO_2 particle: 40 %, diameter: 130 nm, MP-1040, Nissan Chemicals) was used for constructing a photonic colloidal crystal. Before preparing the photonic colloidal crystal hydrogel, the silica sol was desalted by an ion exchange resin (~15% (w/w); BIO-RAD, AG501-X8) for ~5 min. And then, NIPAM (Wako Pure Chemical, 095-03692),

N, *N*'-Methylenebisacrylamide (MBAA; Wako Pure Chemical, 134-02352) as a cross-linker (W_{NIPAM} : W_{MBAA} = 100:1), 0.5 % (v/v) photo-polymerization initiator (BASF, Irgacure1173), the silica colloidal particles (Diameter: 130 nm) was prepared for the photonic colloidal hydrogel. The concentration of the silica colloidal particles was adjusted for changing structural color; 20% for blue, 10% for green, and 6% for red. For the tubular-shaped micro-robots, the concentration of NIPAM was also changed for the color; 3.5 %(w/w) for blue and 7.0 % (w/w) for green and red. For the rocket-shaped micro-robots, the 7% (v/v) NIPAm was used. Before the gelation process, the pre-gel solution was bubbled by N_2 gas.

Next, the preparation of NMAm with photonic colloidal was described. The ($Si0_2$ particle: 40 %, diameter: 130 nm) was also used for constructing photonic colloidal crystal. Before preparing the photonic colloidal crystal hydrogel, the silica sol was desalted by an ion exchange resin (~15% (w/w)) for ~5 min. And then, NMAm (Tokyo Chemical, M0574f), MBAA as a cross-linker (W_{NMAm} : W_{MBAA} = 50:1), 0.5 % (v/v) Irgacure1173, 6% the silica colloidal particles (Diameter: 130 nm) was prepared for the photonic colloidal hydrogel. Before the gelation process, the pre-gel solution was also bubbled by N_2 gas.

6.5.2 Fabrication of tubular-shaped micro-robots

Fabrication methods of tubular-shaped micro-robots differed depending on the stimuli-responsive hydrogel.

First, the fabrication methods using NIPAm were described (Fig. 6.7 (a)). The main components of tubular micro-robots were a galas capillary, a poly-dimethylsiloxane (PDMS) plug, and the photonic colloid crystal hydrogel. The PDMS was dyed with black ink. The dyed PDMS was injected into the glass capillary (Φ0.8×2 mm; G-2; Narishige) and cured at 70ºC for 2 hours. After curing, the glass capillary was trimmed to 10 mm length (PDMS was adjusted to 2 mm length). Photonic colloidal crystal pre-gel solutions were injected to one end of the glass capillary and cured under a UV light for 3 min by using a mask aligner (EMA-400; Union).

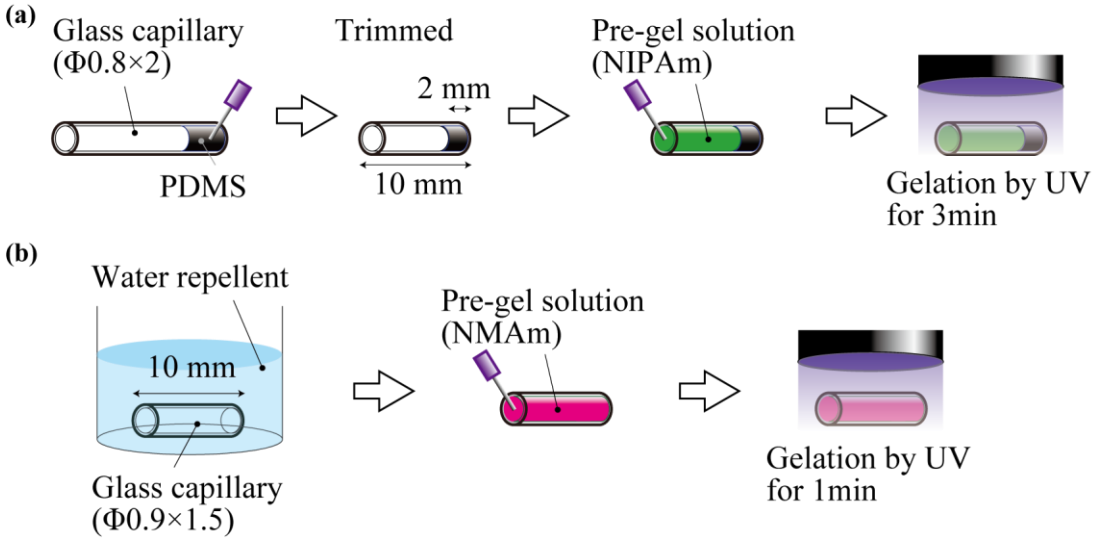

Figure 6.7 Fabrication method of tubular-shaped micro-robots: (a) NIPAm (b) NMAm.

Next, the fabrication methods using NMAm were described (Fig. 6.7 (b)). The main components were a glass capillary and the photonic colloidal crystal hydrogel. The glass capillary (Φ0.9×1.5 mm; G-1.5; Narishige) was trimmed to 10 mm in length. Stimuli-responsive hydrogels tend to adhere to the glass tube, so the glass capillary was treated by water-repelling to reduce the effect of adhesion as the following process. The glass capillary was immersed in a water repellent coating agent (Water Repellent; Rain-X) for 5 min. The water repellent was removed by Kimwipes (S-200; Nippon Paper Crecia) and heating at 70ºC for 3 min. Then, the treated glass capillary was washed with pure water. The pure water was fully removed by heating at 70ºC. Photonic colloidal crystal pre-gel solutions were injected into the glass capillary and cured under a UV light for 1 min by using the mask aligner.

6.5.3 Propulsion setup of tubular–shaped micro-robots

For the driving source, 50% (v/v) ethanol was used. The green micro-robots with NIPAm and the red micro-robots with NMAm were soaked in the 50 % (v/v) ethanol to filled the ethanol in the micro-robots over 2hours. The ethanol-filled micro-robots were placed on the surface of pure water. A chamber for observing the tubular-shaped micro-robots was coated by parylene (~1 μm) for modifying the surface of the chamber to hydrophobic. Depths

of pure water were adjusted to 10 mm for tubular-shaped micro-robots with NIPAm and 5 mm for micro-robots with NMAm. The micro-robots were then floated on the surface of the pure water by surface tension. The ethanol filled in the micro-robots was continuously diffused to the pure water. The released ethanol rises to the air-water interface by buoyancy and generates surface tension asymmetry because the presence of ethanol lowers the surface tension of water (Ethanol: 28.2 mN/m at 20ºC, Water: 72 mN/m at 25ºC). The robot swimming by interfacial flows caused by surface tension gradients. The propulsion behavior was analyzed by video analysis software (Keyence, VW−H2MA).

6.5.4 Experiments of visible-light wavelength change

NIPAM hydrogel shrink as the temperature increases. The structural color change of two types of micro-robots was observed: green micro-robot (10% colloids) and red micro-robot (6% colloids). Micro-robots were once heated over 40ºC and then cooled at room temperature (~23ºC). The structural color change was observed by a digital microscope (Keyence, VH-5500**)**.

NMAm hydrogel can respond to the ethanol concentration. The tubular-shaped micro-robots were once immersed in 70% ethanol overnight to peel the stimuli-responsive hydrogels from the inner glass. After peeling, the tubular-shaped micro-robots were immersed in the 10-100% (v/v) ethanol overnight. The structural color change was observed by the same digital microscope.

6.5.5 Temperature responsiveness of tubular-shaped micro-robots

The micro-robots integrated photonic colloidal crystal hydrogel was successfully fabricated (Fig. 6.8 (a)). The structural colors were clearly observed. When the concentration of colloidal crystal was adjusted to 6, 10, and 20% (w/w), the structural color was red (Fig. 6.8 (a) right), green (Fig. 6.8 (a) center), and blue (Fig. 6.8 (a) left), respectively. Their reflection spectra I_{ref} were also measured (Fig. 6.8 (b)). The peak spectra of each condition were 677 nm (6%), 534 nm (10%), and 481 nm (20%) respectively. It was confirmed that the

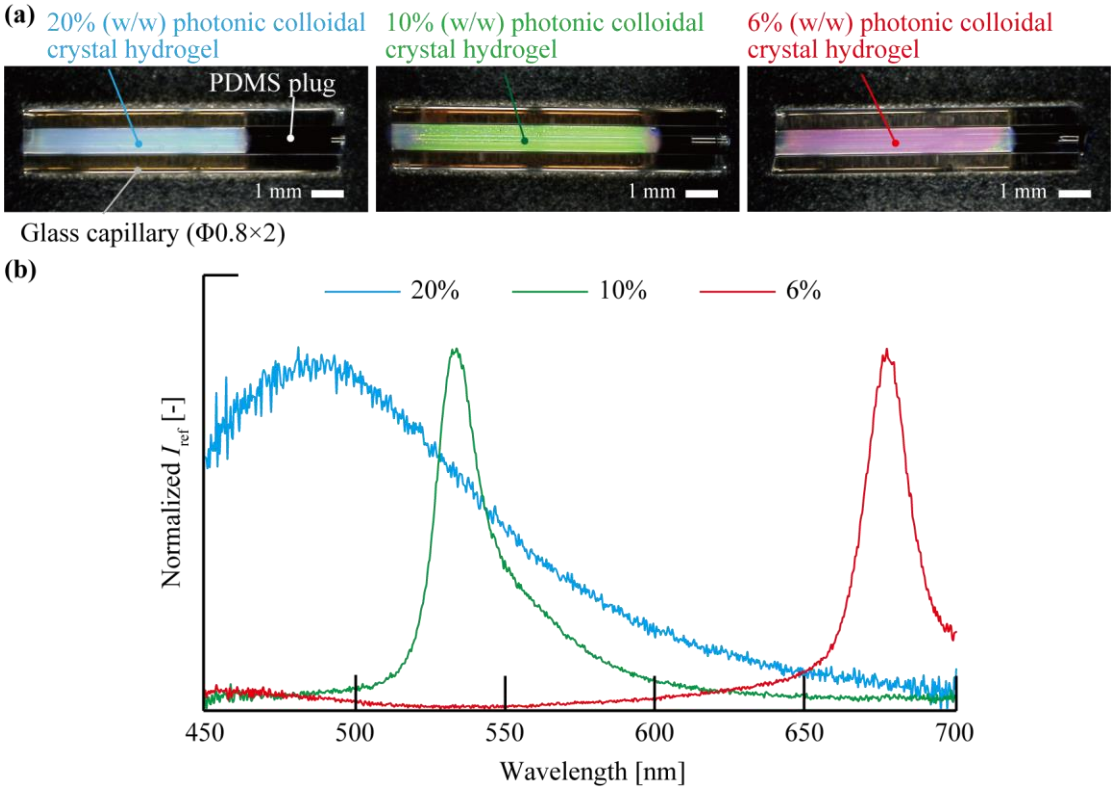

Figure 6.8 Fabricated tubular-shaped micro-robots with NIPAm. (a) The structural color of tubular-shaped micro-robot depend on the concentration of colloid particles. (b) The reflected wavelength.

visible colors correspond to the reflected wavelengths. These results showed that the structural color of micro-robots could be controlled by the concentration of the photonic colloidal crystal. By using the Equations (6.1), (6.3), and (6.4), the effective diameters of each concentration were 281 nm (6%), 224 nm (10%), and 202 nm (20%), where the angle of incident light θ is 90°, the refractive index of silica, n_p, is 1.5, and the refractive index of substances, n_a, is assumed to the refractive index of water (n_a = 1.33).

Next, the structural color change responding to applying stimuli was mentioned. All structural colors were changed to the white color responding to the applied thermal stimuli (Fig. 6.9 centre). The reason for color change to the white color is thought to be caused by the aggregation of polymer chains as the stimuli-responsive hydrogel largely shrunk. On the other hand, the volume changes were hardly observed. It is thought that the stimuli-

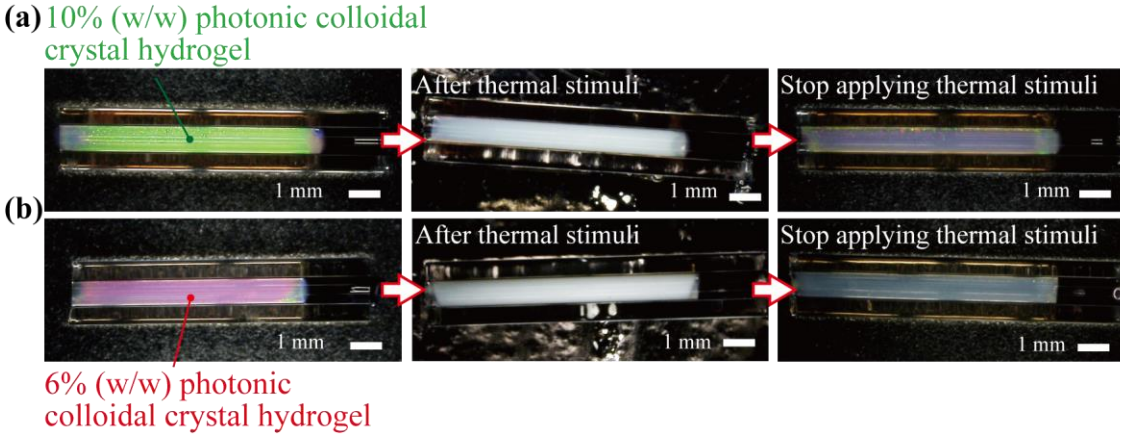

Figure 6.9 Structural color change of tubular-shaped micro-robots with NIPAm: (a) The green micro-robot (10% colloids) and (b) The red micro-robot (6% colloids).

responsive hydrogel adhered to the glass, that inhibits the volume change outside of stimuli-responsive hydrogel while the inner part was largely shrunk. Both structural colors of micro-robots exhibited the blue color as soon as stop applying the thermal stimuli (Fig. 6.9 right). By equation (6.1), the wavelength of the photonic colloidal crystal was shortened as the distance of colloidal particles decreasing. At the long wavelength (~700 nm), the color is red. On the other hand, the color is blue at the short-wavelength (~450 nm). It is considered that this color change was caused by the shrinking of photonic colloidal crystal hydrogel. Therefore, the micro-robots with the photonic colloidal crystal hydrogel could be sense the external stimuli, since the tendency of the results conformed to the theory.

6.5.6 Ethanol responsiveness of tubular-shaped micro-robots

By using NMAm, the micro-robots integrated photonic colloidal crystal hydrogel was also successfully fabricated (Fig. 6.10 (a)). The color of 6% photonic colloidal particles was also red color. When applying the ethanol with 10-60% (v/v) concentration, the color sifting did not exhibit. The peak wavelength of 10% (v/v) and 60% (v/v) were 643 nm and 654 nm, respectively. Moreover, it is observed that the end of photonic colloidal crystal hydrogel is swollen. In general, The NMAm hydrogel swollen after the cross-linking by absorbing the surrounded water and the NMAm hydrogel largely shrink when applied ethanol

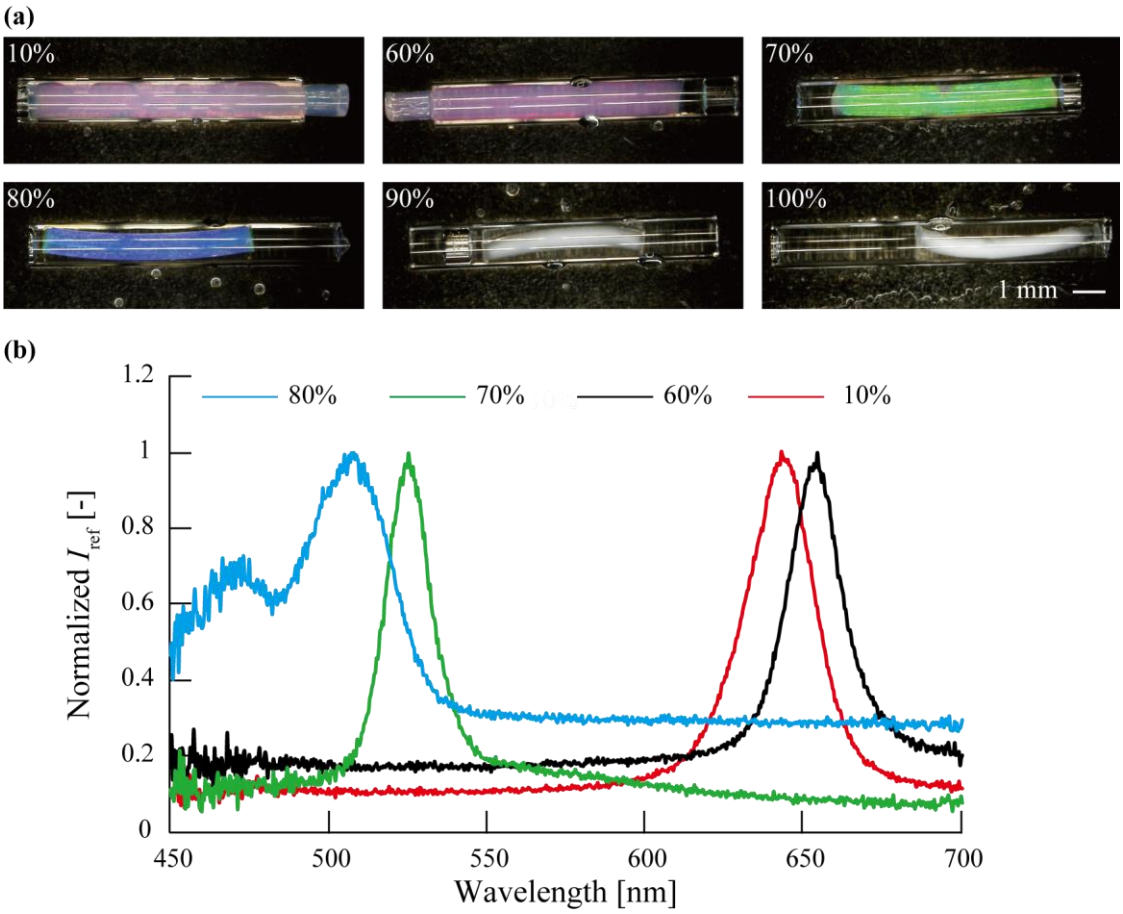

Figure 6.10 Structural color change of tubular-shaped micro-robots with NMAm: (a) The structural color was changed responding to the ethanol concentration and (b) The reflected wavelength.

with a concentration above 50%[103]. Thus, it is considered the swollen state was stable when applied 10-60% (v/v) ethanol.

On the other hand, the colors were successfully shifting to green and blue when applying the 70% (v/v) and 80% (v/v) ethanol, respectively. It was also confirmed that the hydrogel can shrank without adhering to the glass by the water repellent treatment. The peak wavelengths were 525 nm (70% (v/v)) and 508 nm (80% (v/v)) (Fig. 6.10 (b)). When applying 90% (v/v) and 100% (v/v), the color was changed to white. In addition, the peak

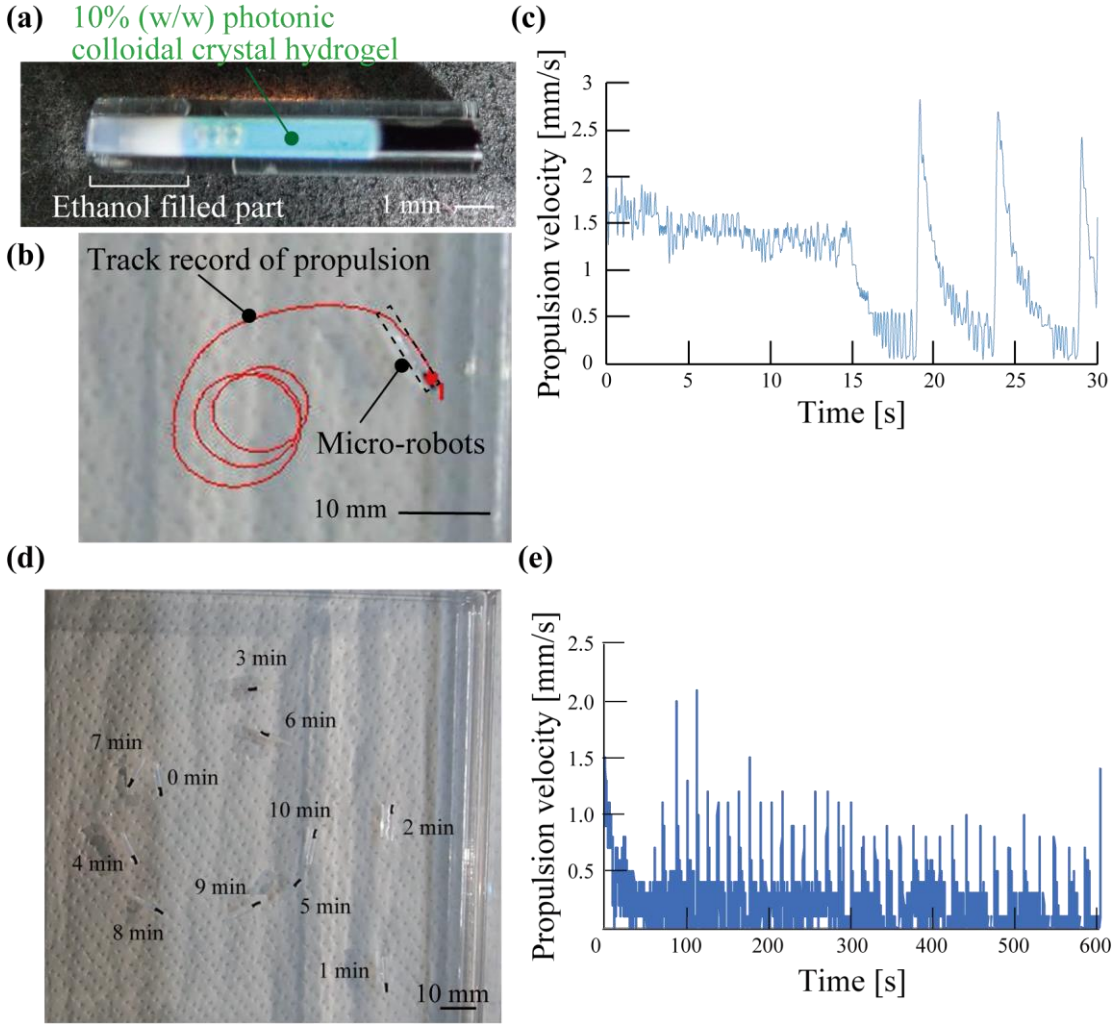

Figure 6.11 Propulsion of tubular-shaped micro-robots with NIPAm. (a) Micro-robots after soaking in ethanol. (b) Track record of propulsion. (c) Measurement of the propulsion velocity of micro-robots for 30s. (d) Brief track record of micro-robots for 10 min. (e) Measurement of the propulsion velocity for 10 min.

wavelength could not be observed. It is considered that the amount of shrinkage is so large that the peak wavelength is outside the visible light region, or that the polymer chain has aggregated that caused the color of hydrogel to change to white.

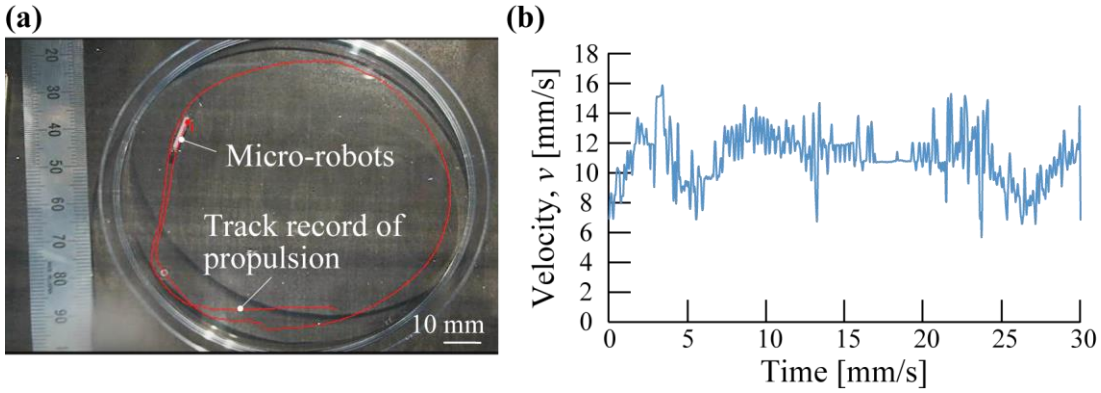

Figure 6.12 Propulsion of tubular-shaped micro-robots with NMAm. (a) Track record of propulsion. (c) Measurement of the propulsion velocity of micro-robots for 30s.

6.5.7 Propulsion of tubular-shaped micro-robots

After soaking in the 50% (v/v) ethanol, it was confirmed that the ethanol was filled in the micro-robots, because the part of the hydrogel shrunk and whiten (Fig. 6.11 (a)). The micro-robots successfully propelled on the pure water (Fig. 6.11 (b)). At first, the micro-robots continuously propelled at ~1.5 mm/s (Fig. 6.11 (c)). After 15 s, the micro-robots emerged in pulsatile motion. The pulsatile velocity was ~2.8 mm/s and the pulse period was ~5 s. The pulsatile motion of the ethanol-driven micro-robots was previously reported[30][104]. The propulsion of micro-robots is largely depending on the ethanol releasing rate that is decreased by the ethanol diffusion. The motion change was considered that the micro-robots were continuously propelled at a high ethanol releasing rate, besides the propulsion behavior, was changed from the continuous motion to the pulsatile motion by decreasing the ethanol releasing rate. In addition, the driving time of our micro-robots was over 10 minutes (Fig.6.11 (d)). During 100 s to 300s, the pulsatile velocity was ~1 mm/s. Over 300 s, the pulsatile velocity was slightly decreased to ~0.8 mm/s (Fig. 6.11 (e)). These results indicated that our proposed micro-robot could propel for the long term by the pulsatile motion.

Then, the propulsion of micro-robots with NMAm was mentioned. While the propulsion behavior of micro-robots with NIPAm was changed, the micro-robots with

NMAm continuously propelled within the 30s (Fig 6.12 (a)). The average propulsion velocity was 11 mm/s (Fig. 6.12 (b)), that was much larger than the micro-robots with NIPAm (~1.5 mm/s).

6.6 Rocket-shaped micro-robots

In this section, the ethanol-responsiveness and propulsion behavior of rocket-shaped micro-robots were mentioned.

6.6.1 Preparation of photonic colloidal crystal hydrogel

The preparation of NMAm with photonic colloidal was described. The ($Si0_2$ particle: 40 %, diameter: 130 nm) was also used for constructing photonic colloidal crystal. Before preparing the photonic colloidal crystal hydrogel, the silica sol was desalted by an ion exchange resin (~15% (w/w)) for ~5 min. And then, NMAm (Tokyo Chemical, M0574f), MBAA as a cross-linker (W_{NMAm} : W_{MBAA} = 50:1), 0.5 % (v/v) Irgacure1173, 10% or 15% silica colloidal particles (Diameter: 130 nm) were prepared for the photonic colloidal hydrogel. Before the gelation process, the pre-gel solution was also bubbled by N_2 gas.

6.6.2 Fabrication of rocket-shaped micro-robots

The rocket-shaped micro-robots were constructed in 4 parts; a PDMS body, a PDMS bottom part, a hydrogel for energy storage, and a photonic colloidal crystal hydrogel for the sensor. The PDMS body and bottom part were fabricated by a molding process. For fabricating each mold, an acryl board was processed through an acryl machining tool. The uncured PDMS was poured into these acryl molds, and then, cured by heating at 75ºC for 2 hours. The molded PDMS body and bottom part were bonded to each other by uncured PDMS (Fig. 6.13 (a)).

To bonding the photonic colloidal crystal hydrogel to the PDMS body, the PDMS body was treated with a benzophenone (B9300, Sigma-Aldrich) by followed process (Fig. 6.13 (b)). The PDMS body was cleaned with isopropanol and deionized water. To enhance

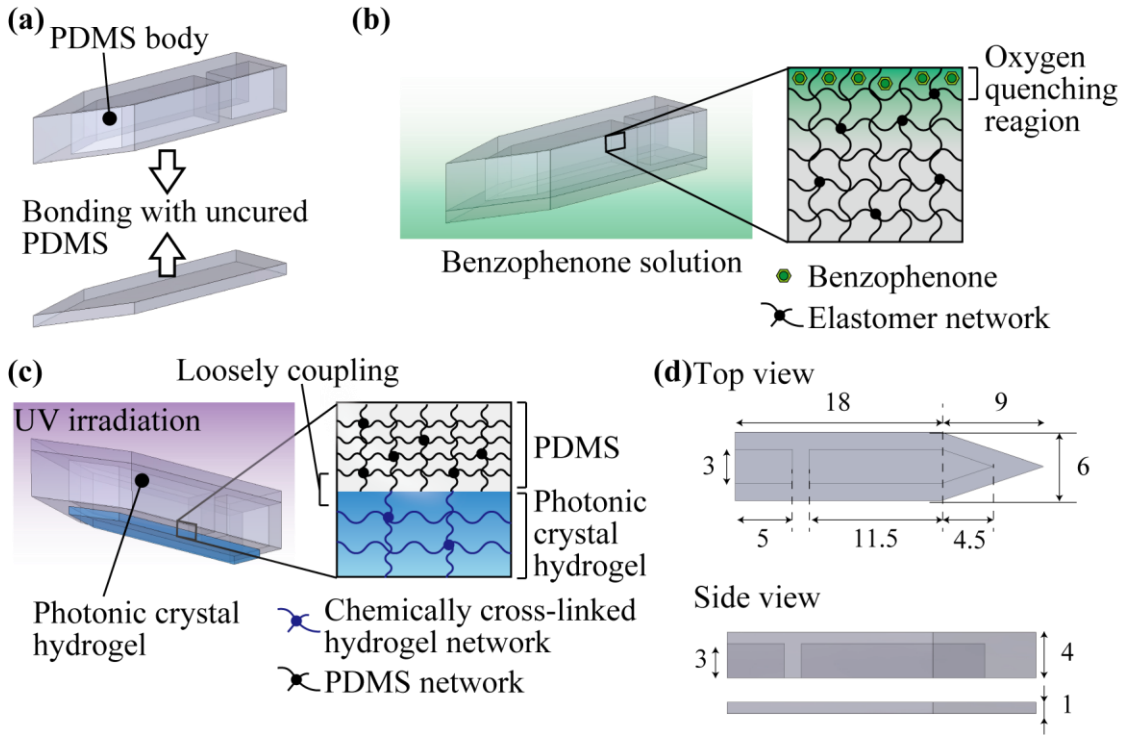

Figure 6.13 Fabrication of the rocket-shaped micro-robots. (a) PDMS body and bottom part was bonded by uncured PDMS. (b) The PDMS body was treated by benzophenone. (c) The photonic crystal hydrogel was cross-linked to the PDMS body by UV irradiation. (d) Scale of the micro-robot (unit is mm).

the wettability of the PDMS body, the PDMS body was treated by atmospheric plasma by a plasma etcher (SEDE-P, meiwafosis). The plasma-treated PDMS body was then immersed into a benzophenone solution (10% (w/w) in ethanol) for over 3 min.

The photonic colloidal crystal pre-gel solution was injected into the PDMS body. Then, the PDMS body was placed upside down into the chamber filled with the pre-gel solution. These phonic colloidal crystal pre-gel solutions were then gelled by UV irradiation for 3 min (Fig. 6.13 (C)). At the same time, the surface of the PDMS body and the photonic colloidal crystal hydrogel were loosely cross-linked. The fabricated micro-robots integrated with stimuli-responsive hydrogel were then immersed into pure water or 70% ethanol overnight.

The design of the micro-robot was shown in Fig. 6.13 (d). Based on chapter 6.4.2,

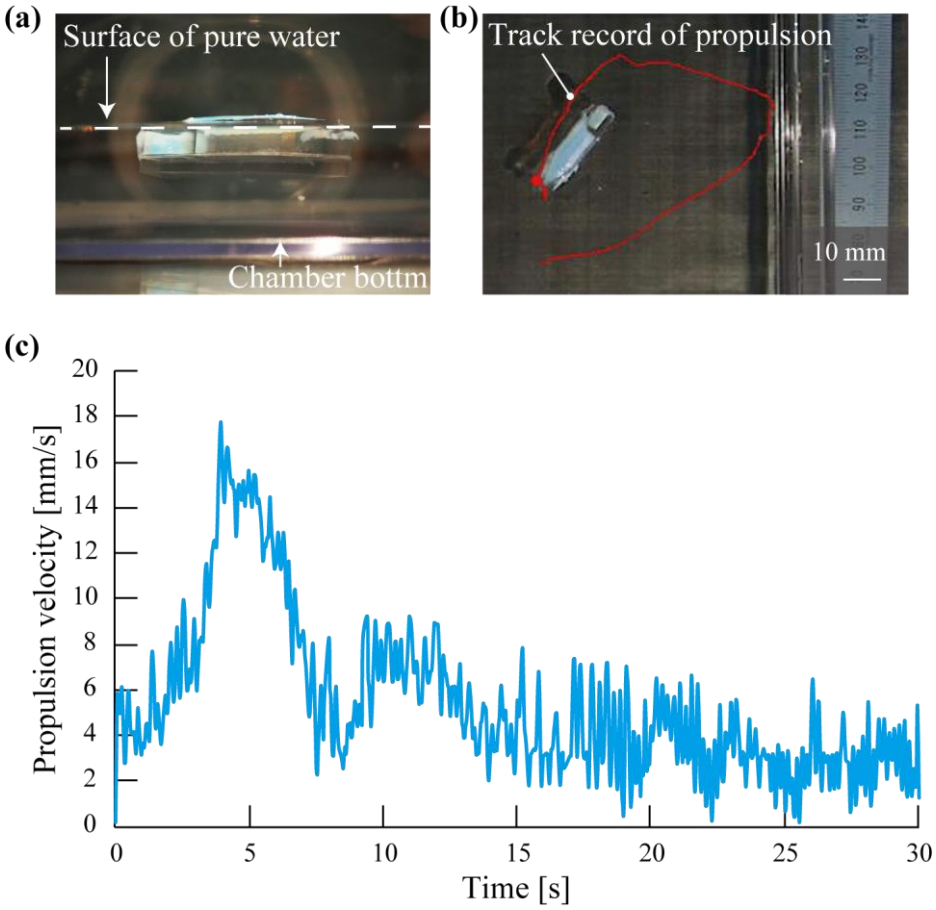

Figure 6.14 Propulsion of rocket-shaped micro-robots. (a) The rocket-shaped micro-robot can float on the water surface. (b) The track record of propulsion. (c) Propulsion velocity of rocket-shaped micro-robot.

the design was determined. In this design, the upward force was F_b-(F_p + F_{pg} + F_g + F_a) = 1.58 > 0, thus the micro-robots can float on the water surface. In this calculation, the densities of water, air, and PDMS were used 1 g/cm^3, 1.293×10^{-3} g/cm^3, and 0.965 g/cm^3, respectively. The thickness of hydrogel was estimated to 1 mm.

6.6.3 Propulsion setup for rocket-shaped micro-robots

For the driving energy source, 70% (v/v) ethanol was used. The rocket-shaped micro-robots were soaked in the 70 % (v/v) ethanol to filled the ethanol in the energy chamber overnight. A chamber for observing the rocket-shaped micro-robots was treated with water

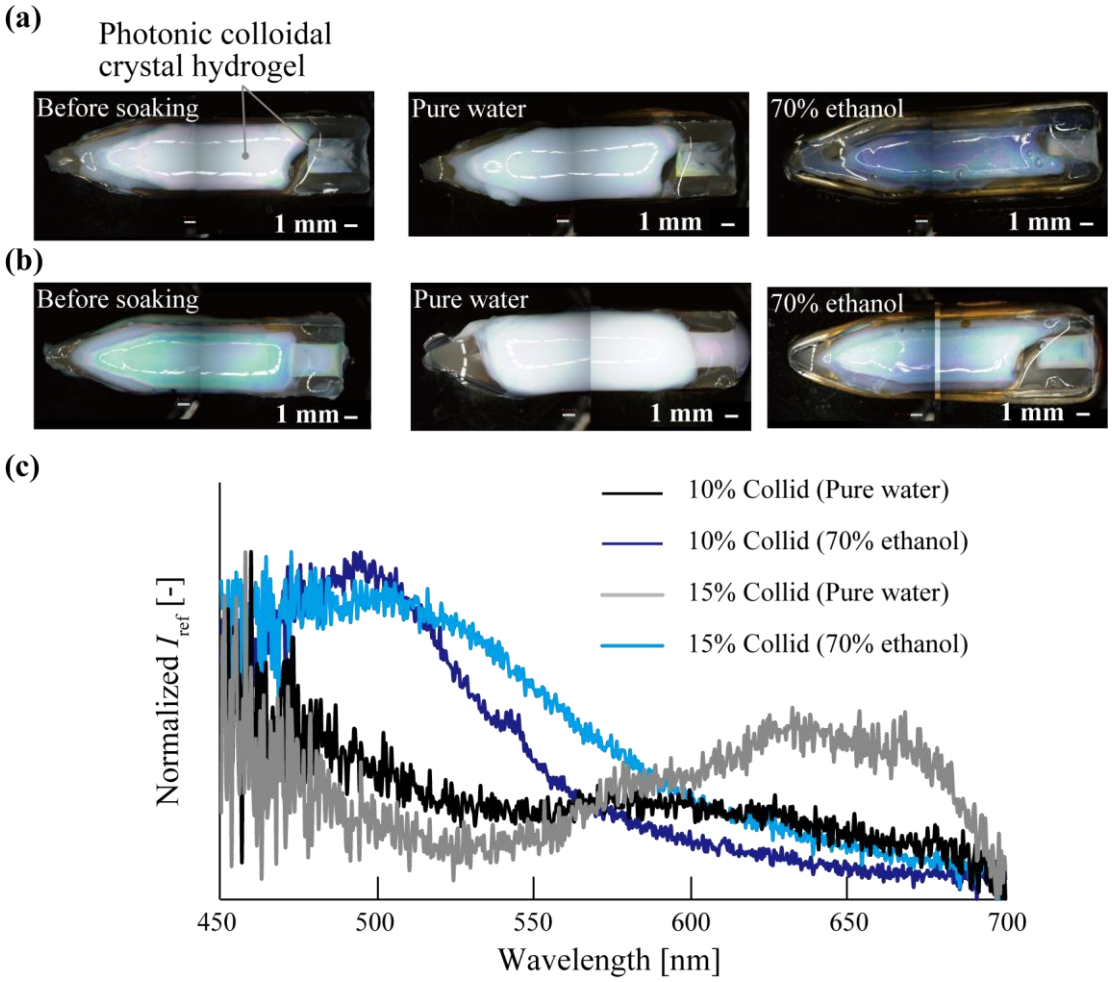

Figure 6.15 The structural color change of rocket-shaped micro-robots. (a) 10% colloidal particles. (b) 20% colloidal particles. (c) The reflected wavelength.

repellent for modifying the surface of the chamber to hydrophobic.

6.6.4 Experiments of color-change

Fabricated rocket-shaped micro-robots were immersed in pure water or 70% (v/v) ethanol overnight. The structural color of each rocket-shaped micro-robots was observed by the digital microscope.

6.6.5 Propulsion behavior of rocket-shaped micro-robots

The rocket-shaped micro-robots that soaked in 70% (v/v) ethanol were successfully floated on the surface of pure water (Fig. 6.14 (a)). The rocket-shaped micro-robots are continuously propelled by the Marangoni effect (Fig. 6.14 (b)). The rocket-shaped micro-robots once accelerated and thereafter the propulsion velocity was converged to 4 mm/s (average propulsion velocity of 10 to 30 s, Fig. 6.14 (c)).

6.6.6 Ethanol-responsiveness of rocket-shaped micro-robots

The micro-robots fabricated with 10% colloidal particles exhibited a slightly red color (Fig. 6.15 (a) left) and the micro-robots fabricated with 15% colloidal particles exhibited green color (Fig. 6.15 (b) left). Both micro-robots swelled when immersing the pure water (Fig. 6.15 (a) and (b) center). While the white color was observed at each micro-robot by using the digital microscope, the micro-robots with 15% colloidal particles reflected the longer wavelength (red color, Fig. 6.15 (c) gray bar). Regarding the micro-robot with 10% colloidal particles, it was observed that light in the entire visible light range was universally reflected. On the other hand, both micro-robots shrunk when immersing the 70% ethanol. Both colors were changed to blue color (Fig. 6.15 (c) blue and dark blue bar). Each peak wavelengths were 494 μm and 472 μm for 10% colloid particles and 15% colloid particles, respectively. These results showed that visible-light wavelength could be changed responding to the ethanol concentration.

6.7 Conclusion

It is proposed that micro-robot integrated with photonic colloidal crystal hydrogel for converting the temperature or ethanol concentration into visible-light wavelength change. The micro-robots can float on the pure water by the surface tension and the buoyancy force. By diffusing the ethanol from the inner body, the micro-robots were successfully propelled by the Marangoni effect. The tubular-shaped micro-robots with NIPAm hydrogel continuously propelled at ~1.5 mm/s. After 15 s, the tubular-shaped micro-robots exhibited

pulsatile motion. It is considered that propulsion behavior was changed by decreasing the ethanol concentration because the surface tension is depending on the concentration of ethanol. Moreover, the tubular-shaped micro-robots with NMAm and the rocket-shaped micro-robots continuously propelled within 30 s. The propulsion behavior differed from the tubular-shaped micro-robots with NIPAm hydrogel. Based on the previous research, the Marangoni propulsion is affected not only by the diffusing ethanol concentration but also by the friction of the sunken part of micro-robots and the depth of the water surface[105]. It is thought that the difference in propulsion behavior was caused by these factors.

Next, the results of photonic colloidal crystal hydrogel were concluded. It is showed that the structural color of the photonic colloidal crystal hydrogel in the tubular-shaped micro-robots was controlled by adjusting the concentration of the colloidal particles. By applying the thermal stimuli, the structural colors of tubular-shaped micro-robots were changed from green or red to a blue color when using the thermal-responsive hydrogel (NIPAm hydrogel). Furthermore, the reflected wavelength of tubular-shaped micro-robot was also sifted from the long-wavelength (red color) to a shorter wavelength (green and blue color) as the ethanol concentration increase when using the ethanol-responsive hydrogel (NAMm hydrogel).

Regarding the rocket-shaped micro-robots, the photonic colloidal crystal hydrogel swelled when immersing into pure water and the structural color did not observe. When applying the 70% ethanol, the structural color was exhibited. The reflected wavelength of rocket-shaped micro-robots has a broader range than that of tubular-shaped micro-robots. It is considered that the unevenness in the photonic colloidal crystals may have occurred during the preparation process.

Above these results, it is confirmed that proposed micro-robots could convert the external temperature or ethanol concentration into visible-light wavelength change. Based on the results, it is showed that information about the external environment can be presented through the micro-robot integrated with stimuli-responsive hydrogel. By using other stimuli-responsive hydrogels that respond to various stimuli such as pH and chemical compounds, it is expected that various types of sensing micro-robots could be realized.

Chapter 7
Conclusions

7.1 Conclusions

The objective of this dissertation is to develop untethered micro-robots integrated with stimuli-responsive hydrogel for sensing the external environment.

7.1.1 Autonomous propulsion velocity control

First, it was proposed that the spiral-shaped micro-swimmer for autonomous propulsion velocity control by sensing surrounding temperature. At first, the relationship between the geometry of the spiral-shaped micro-swimmer and the propulsion velocity was theoretically analyzed based on the fluid dynamics. The theoretical analysis revealed that the propulsion velocity of spiral-shaped micro-swimmers is largely depending on the pitch angle. Then, the spiral-shaped micro-swimmers with various pitch angles were successfully fabricated by the buoyancy-assisted anisotropic gelation method. It is experimentally confirmed that the propulsion velocity of spiral-shaped micro-swimmer was changed by their pitch angle.

Next, the deformation behavior of the spiral-shaped micro-swimmer was analyzed by the finite element simulation. It was revealed that the deformation behavior of spiral-shaped micro-swimmer was largely depending on the patterning direction of the stimuli-responsive hydrogel.

Finally, based on the simulation results, the double-layered spiral-shaped micro-swimmers were fabricated. The fabricated double-layered spiral-shaped micro-swimmer successfully deformed responding to the applied thermal stimuli. The acceleration and deceleration of spiral-shaped micro-swimmers were also achieved.

7.1.2 Autonomously converting information

The micro-robot integrated with photonic colloidal crystal hydrogel for converting the temperature and ethanol concentration into visible color sifting was proposed. In this dissertation, two brief concepts of micro-robot integrated with photonic colloidal crystal hydrogel were proposed: a tubular-shaped micro-robot and a rocket-shaped micro-robot. These micro-robots have ethanol storage that enables them to propel by the Marangoni effect. By using a thermal-responsive hydrogel and an ethanol-responsive hydrogel, the information of temperature and ethanol concentration was successfully converted to the visible color sifting.

7.2 Outlook

In this dissertation, enhancing the autonomy of untethered micro-robots through the integration with stimuli-responsive hydrogel was proposed. However, there remain challenges in terms of motility control, communication, and responsivity.

Motility controls especially propulsion direction control are required. The proposed spiral-shaped micro-swimmer propel responding to the magnetic fields, thus the posture of micro-robots was constrained by the direction of magnetic fields. Moreover, the micro-swimmer can only propel within the range where the magnetic fields can be applied. While the Marangoni propulsion is less constrained by the energy supply, the propulsion direction is hardly controlled because the Marangoni propulsion is caused by the diffusion of ethanol. Therefore, it is necessary to develop a novel propulsion system that is unconstrained and controllable. For example, it is considered that the autonomously rotating spiral-shaped actuator like flagella's specialized motor units was an attractive candidate[75]. Microorganisms can be driven by generating ATP, which has high energy density, from

surrounding sugars. Therefore, in addition to the driving method, a system that uses materials with high energy density as a drive source or a system that converts an external energy source is an important factor for realizing a highly functional micro-robot. In addition to the driving method and source, a novel patterning design not only a cross-sectional pattern but also an axial pattern is needed for a more complex deformation of spiral-shaped to realize the propulsion direction control[106][65].

Photonic colloidal crystal hydrogel can convert the temperature or ethanol concentration to the visible color change. However, the color information is not suitable for detecting the detail information and sensing in non-visible areas. To overcome this problem, it is expected to develop a new approach for converting the external environments to other information such as electrical signals. Wireless communications are also required for enhancing the ability of untethered micro-robots for detecting external environments.

In this dissertation, the autonomies of motility control and converting into other information were respectively achieved. These autonomies must be integrated into a single micro-robot. Although there remain many challenges, the achievements of this dissertation lead to an open new avenue of untethered micro-robots. In addition, the proposed micro-robots mainly consist of soft materials, thus the proposed design strategies are expected to use biochemical applications including the soft robot, bio-hybrid robotics, and medical devices.

In addition to the autonomy, the new strategy for developing an intelligent system was also proposed in this dissertation. Various types of stimuli-responsive actuators have been previously reported. For driving these stimuli-responsive actuators, the stimuli were artificially applied. In other words, previous researches have used stimuli as a driving source, and, to the best of my knowledge, there is no integrated system that could sense their surrounding environments and drive based on the information. In this study, it is proposed that the stimuli-responsive hydrogel was used for the soft actuator integrated with the sensing element. This new integrated system with the soft actuator and the sensing elements can realize the motility control with sensing external environments. It is believed that this concept of an integrated system of sensors and actuators using stimuli-responsive hydrogel will be

useful for creating new intelligent systems and new soft devices for robots.

Finally, it is believed that this research had a great impact on academic research in terms of the idea of using the volume change of stimuli-responsive hydrogel as a new generation of intelligences or smart components of robotics. Furthermore, it is thought that the processing of functional materials including stimuli-responsive hydrogel and the development of new generation systems will greatly contribute to the development of mechanical engineering, in particular robotics and intelligent system, and processing of soft materials.

References

[1] G. Z. Yang, J. Bellingham, P. E. Dupont, P. Fischer, L. Floridi, R. Full, N. Jacobstein, V. Kumar, M. McNutt, R. Merrifield, B. J. Nelson, B. Scassellati, M. Taddeo, R. Taylor, M. Veloso, Z. L. Wang, R. Wood, *Sci. Robot.* **2018**, *3*, DOI 10.1126/scirobotics.aar7650.

[2] L. Hines, K. Petersen, G. Z. Lum, M. Sitti, *Adv. Mater.* **2017**, *29*, DOI 10.1002/adma.201603483.

[3] S. I. Rich, R. J. Wood, C. Majidi, *Nat. Electron.* **2018**, *1*, 102.

[4] P. Won, K. K. Kim, H. Kim, J. J. Park, I. Ha, J. Shin, J. Jung, H. Cho, J. Kwon, H. Lee, S. H. Ko, *Adv. Mater.* **2020**, *2002397*, 1.

[5] X. Z. Chen, B. Jang, D. Ahmed, C. Hu, C. De Marco, M. Hoop, F. Mushtaq, B. J. Nelson, S. Pané, *Adv. Mater.* **2018**, *30*, 1.

[6] M. Z. Miskin, A. J. Cortese, K. Dorsey, E. P. Esposito, M. F. Reynolds, Q. Liu, M. Cao, D. A. Muller, P. L. McEuen, I. Cohen, *Nature* **2020**, *584*, 557.

[7] N. T. Jafferis, E. F. Helbling, M. Karpelson, R. J. Wood, *Nature* **2019**, *570*, 491.

[8] B. Kwak, J. Bae, *Bioinspiration and Biomimetics* **2018**, *13*, DOI 10.1088/1748-3190/aab460.

[9] H. W. Huang, M. S. Sakar, A. J. Petruska, S. Pané, B. J. Nelson, *Nat. Commun.* **2016**, *7*, 1.

[10] Y. Morimoto, H. Onoe, S. Takeuchi, *Sci. Robot.* **2018**, *3*, 1.

[11] C. Appiah, C. Arndt, K. Siemsen, A. Heitmann, A. Staubitz, C. Selhuber-Unkel, *Adv. Mater.* **2019**, *31*, DOI 10.1002/adma.201807747.

[12] L. Sun, Y. Yu, Z. Chen, F. Bian, F. Ye, L. Sun, Y. Zhao, *Chem. Soc. Rev.* **2020**, *49*, 4043.

[13] R. a Wickstrom, J. R. Davis, *IEEE Trans. Electron Devices* **1967**, *14*, 117.

[14] J. B. Angell, S. C. Terry, P. W. Barth, *Micromechanics MEMS Class. Semin. Pap. to 1990* **1997**, *248*, 38.

[15] R. Bruhwiler, B. Goldberg, N. Doshi, O. Ozcan, N. Jafferis, M. Karpelson, R. J. Wood, *IEEE Int. Conf. Intell. Robot. Syst.* **2015**, *2015-Decem*, 5727.

[16] F. Soto, J. Wang, R. Ahmed, U. Demirci, *Adv. Sci.* **2020**, *7*, 1.

[17] X. Yang, L. Chang, N. O. Pérez-Arancibia, *Sci. Robot.* **2020**, *5*, 1.

[18] A. T. Baisch, O. Ozcan, B. Goldberg, D. Ithier, R. J. Wood, *Int. J. Rob. Res.* **2014**, *33*,

1063.

[19] Y. Wu, J. K. Yim, J. Liang, Z. Shao, M. Qi, J. Zhong, Z. Luo, X. Yan, M. Zhang, X. Wang, R. S. Fearing, R. J. Full, L. Lin, *Sci. Robot.* **2019**, *4*, DOI 10.1126/scirobotics.aax1594.

[20] M. Buck, S. Razavi, R. Derose, T. Inoue, P. a Silver, P. Subsoontorn, D. Endy, Y. Gerchman, C. H. Collins, F. H. Arnold, R. Weiss, M. C. Jensen, C. D. Smolke, L. Wroblewska, L. Prochazka, Y. Benenson, J. J. Tabor, C. a Voigt, C. Lou, a Tamsir, B. C. Stanton, M. Wieland, M. Fussenegger, I. Deese, N. Publishing, G. New, S. K. Lee, J. D. Keasling, a P. Arkin, D. Del Vecchio, W. Brattain, *Science (80-.).* **2013**, 603.

[21] Q. Zhao, S. Liu, J. Chen, G. He, J. Di, L. Zhao, T. Su, M. Zhang, Z. Hou, *Rob. Auton. Syst.* **2021**, *140*, 103733.

[22] T. Ranzani, S. Russo, N. W. Bartlett, M. Wehner, R. J. Wood, *Adv. Mater.* **2018**, *30*, 1.

[23] C. M. Lewandowski, *Animal Locomotion Taylor*, **2015**.

[24] X. Ji, X. Liu, V. Cacucciolo, M. Imboden, Y. Civet, A. El Haitami, S. Cantin, Y. Perriard, H. Shea, *Sci. Robot.* **2019**, *4*, DOI 10.1126/scirobotics.aaz6451.

[25] P. Vartholomeos, E. Papadopoulos, *Proc. - IEEE Int. Conf. Robot. Autom.* **2006**, *2006*, 649.

[26] M. Rubenstein, A. Cornejo, R. Nagpal, *Science (80-.).* **2014**, *345*, 795.

[27] L. E. Scriven, C. V. Sternling, *Nature* **1960**, *187*, 186.

[28] J. W. M. Bush, D. L. Hu, *Annu. Rev. Fluid Mech.* **2006**, *38*, 339.

[29] L. J. Burton, N. Cheng, J. W. M. Bush, *Integr. Comp. Biol.* **2014**, *54*, 969.

[30] R. Sharma, S. T. Chang, O. D. Velev, *Langmuir* **2012**, *28*, 10128.

[31] J. C. Nawroth, H. Lee, A. W. Feinberg, C. M. Ripplinger, M. L. McCain, A. Grosberg, J. O. Dabiri, K. K. Parker, *Nat. Biotechnol.* **2012**, *30*, 792.

[32] S.-J. Park, M. Gazzola, K. S. Park, S. Park, V. Di Santo, E. L. Blevins, J. U. Lind, P. H. Campbell, S. Dauth, A. K. Capulli, F. S. Pasqualini, S. Ahn, A. Cho, H. Yuan, B. M. Maoz, R. Vijaykumar, J.-W. Choi, K. Deisseroth, G. V. Lauder, *Science (80-.).* **2016**, *353*.

[33] V. Magdanz, S. Sanchez, O. G. Schmidt, *Adv. Mater.* **2013**, *25*, 6581.

[34] M. Wehner, R. L. Truby, D. J. Fitzgerald, B. Mosadegh, G. M. Whitesides, J. A. Lewis, R. J. Wood, *Nature* **2016**, *536*, 451.

[35] B. Mosadegh, C. H. Kuo, Y. C. Tung, Y. S. Torisawa, T. Bersano-Begey, H. Tavana, S. Takayama, *Nat. Phys.* **2010**, *6*, 433.

[36] S. Hollar, A. Flynn, C. Bellew, K. S. J. Pister, *Proc. IEEE Micro Electro Mech. Syst.* **2003**, 706.

References

[37] J. James, V. Iyer, Y. Chukewad, S. Gollakota, S. B. Fuller, *Proc. - IEEE Int. Conf. Robot. Autom.* **2018**, 3587.

[38] X.-Z. Chen, M. Hoop, F. Mushtaq, E. Siringil, C. Hu, B. J. Nelson, S. Pané, *Appl. Mater. Today* **2017**, *9*, 37.

[39] K. E. Peyer, L. Zhang, B. J. Nelson, *Nanoscale* **2013**, *5*, 1259.

[40] S. Tottori, L. Zhang, F. Qiu, K. K. Krawczyk, A. Franco-Obregõn, B. J. Nelson, *Adv. Mater.* **2012**, *24*, 811.

[41] D. Walker, M. Kübler, K. I. Morozov, P. Fischer, A. M. Leshansky, *Nano Lett.* **2015**, *15*, 4412.

[42] W. Hu, G. Z. Lum, M. Mastrangeli, M. Sitti, *Nature* **2018**, *554*, 81.

[43] X. Du, H. Cui, T. Xu, C. Huang, Y. Wang, Q. Zhao, Y. Xu, X. Wu, *Adv. Funct. Mater.* **2020**, *30*, 1.

[44] N. Miki, I. Shimoyama, *J. Microelectromechanical Syst.* **2002**, *11*, 584.

[45] R. St Pierre, W. Gao, J. E. Clark, S. Bergbreiter, *Bioinspiration and Biomimetics* **2020**, *15*, DOI 10.1088/1748-3190/ab9fa9.

[46] X. Liu, J. Liu, S. Lin, X. Zhao, *Mater. Today* **2020**, *36*, 102.

[47] Y. Lee, W. J. Song, J. Y. Sun, *Mater. Today Phys.* **2020**, *15*, 100258.

[48] J. F. Mano, *Adv. Eng. Mater.* **2008**, *10*, 515.

[49] H. G. Schild, *Prog. Polym. Sci.* **1992**, *17*, 163.

[50] D. Morales, I. Podolsky, R. W. Mailen, T. Shay, M. D. Dickey, O. D. Velev, *Micromachines* **2016**, *7*, DOI 10.3390/mi7060098.

[51] Y. Takashima, S. Hatanaka, M. Otsubo, M. Nakahata, T. Kakuta, A. Hashidzume, H. Yamaguchi, A. Harada, *Nat. Commun.* **2012**, *3*, 1270.

[52] N. Bassik, B. T. Abebe, K. E. Laflin, D. H. Gracias, *Polymer (Guildf).* **2010**, *51*, 6093.

[53] G. Ye, X. Wang, *Biosens. Bioelectron.* **2010**, *26*, 772.

[54] Q. Zhao, J. W. C. Dunlop, X. Qiu, F. Huang, Z. Zhang, J. Heyda, J. Dzubiella, M. Antonietti, J. Yuan, *Nat. Commun.* **2014**, *5*, DOI 10.1038/ncomms5293.

[55] M. Tsuchiya, Y. Kurashina, H. Onoe, *Sci. Rep.* **2019**, *9*, 1.

[56] L. Ionov, *Adv. Funct. Mater.* **2013**, *23*, 4555.

[57] H. Cui, Q. Zhao, Y. Wang, X. Du, *Chem. - An Asian J.* **2019**, *14*, 2369.

[58] D. Buenger, F. Topuz, J. Groll, *Prog. Polym. Sci.* **2012**, *37*, 1678.

[59] A. Richter, G. Paschew, S. Klatt, J. Lienig, K.-F. Arndt, H.-J. P. Adler, *Sensors* **2008**, *8*, 561.

[60] K. Y. Lee, D. J. Mooney, *Prog. Polym. Sci.* **2012**, *37*, 106.

[61] S. N. Pawar, K. J. Edgar, *Biomaterials* **2012**, *33*, 3279.

[62] W. E. Hennink, C. F. van Nostrum, *Adv. Drug Deliv. Rev.* **2012**, *64*, 223.

[63] K. Yoshida, H. Onoe, *Sci. Rep.* **2017**, *7*, 1.

[64] S. Nakajima, R. Kawano, H. Onoe, *Soft Matter* **2017**, *13*, 3710.

[65] N. Takeuchi, S. Nakajima, K. Yoshida, R. Kawano, Y. Hori, H. Onoe, *Soft Robot.* **2020**, *00*, 1.

[66] S. J. Jeon, A. W. Hauser, R. C. Hayward, *Acc. Chem. Res.* **2017**, *50*, 161.

[67] B. Xu, X. Han, Y. Hu, Y. Luo, C. H. Chen, Z. Chen, P. Shi, *Small* **2019**, *15*, 1.

[68] R. T. Shafranek, S. C. Millik, P. T. Smith, C. U. Lee, A. J. Boydston, A. Nelson, *Prog. Polym. Sci.* **2019**, *93*, 36.

[69] H. Yuk, T. Zhang, S. Lin, G. A. Parada, X. Zhao, *Nat. Mater.* **2016**, *15*, 190.

[70] M. H. Schneider, Y. Tran, P. Tabeling, *Langmuir* **2011**, *27*, 1232.

[71] H. Yuk, T. Zhang, G. A. Parada, X. Liu, X. Zhao, *Nat. Commun.* **2016**, *7*, 1.

[72] D. Dendukuri, P. Panda, R. Haghgooie, J. M. Kim, T. A. Hatton, P. S. Doyle, *Macromolecules* **2008**, *41*, 8547.

[73] J. Zhou, A. V. Ellis, N. H. Voelcker, *Electrophoresis* **2010**, *31*, 2.

[74] 中野義夫, ゲルテクノロジーハンドブック 機能設計・評価・シミュレーションから製造プロセス・製品化まで, 株式会社エヌ・ティー・エス, **2014**.

[75] E. Lauga, *Annu. Rev. Fluid Mech.* **2016**, *48*, 105.

[76] L. J. Fauci, R. Dillon, *Annu. Rev. Fluid Mech.* **2006**, *38*, 371.

[77] S. E. Spagnolie, E. Lauga, *Phys. Rev. Lett.* **2011**, *106*, 1.

[78] H. C. Berg, *Annu. Rev. Biochem.* **2003**, *72*, 19.

[79] B. Christopher, H. Winet., *Annu. Rev. Fluid Mech.* **1977**, *9*, 339.

[80] J. Lighthill, *SIAM Rev.* **1976**, *18*, 161.

[81] C. R. Calldine, *J. Mol. Biol.* **1978**, *118*, 457.

[82] E. M. Purcell, *Am. J. Phys.* **1977**, *45*, 3.

[83] D. F. Blair, *Annu. Rev. Microbiol.* **1995**, *49*, 489.

[84] N. C. Darnton, H. C. Berg, *Biophys. J.* **2007**, *92*, 2230.

[85] L. Turner, W. S. Ryu, H. C. Berg, *J. Bacteriol.* **2000**, *182*, 2793.

References

[86] K. Shiba, S. A. Baba, T. Inoue, M. Yoshida, *Proc. Natl. Acad. Sci.* **2008**, *105*, 19312.

[87] K. E. Peyer, S. Tottori, F. Qiu, L. Zhang, B. J. Nelson, *Chem. - A Eur. J.* **2013**, *19*, 28.

[88] M. Zenobi-Wong, K. Sugihara, B. J. Nelson, L. Zhang, R. Mhanna, F. Qiu, Y. Ding, *Small* **2014**, *10*, 1953.

[89] K. Kobayashi, K. Ikuta, *Proc. IEEE Int. Conf. Micro Electro Mech. Syst.* **2009**, 11.

[90] L. Zhang, J. J. Abbott, L. Dong, B. E. Kratochvil, D. Bell, B. J. Nelson, *Appl. Phys. Lett.* **2009**, *94*, 2007.

[91] R. Grisch, B. J. Nelson, M. A. Zeeshan, K. M. Sivaraman, B. Özkale, K. E. Peyer, J. Sort, M. S. Sakar, E. Pellicer, S. Pané, *Small* **2013**, *10*, 1284.

[92] W. Gao, X. Feng, A. Pei, C. R. Kane, R. Tam, C. Hennessy, J. Wang, *Nano Lett.* **2014**, *14*, 305.

[93] S.-J. Shin, J.-Y. Park, J.-Y. Lee, H. Park, Y.-D. Park, K.-B. Lee, C.-M. Whang, S.-H. Lee, *Langmuir* **2007**, *1*, 9104.

[94] L. Zhang, J. J. Abbott, L. Dong, K. E. Peyer, B. E. Kratochvil, H. Zhang, C. Bergeles, B. J. Nelson, *Nano Lett.* **2009**, *9*, 3663.

[95] B. Y. S. Timoshenko, *J. Opt. Soc. Am.* **1925**, *11*, 233.

[96] N. Boon, P. Schurtenberger, *Phys. Chem. Chem. Phys.* **2017**, *19*, 23740.

[97] V. B. Nguyen, C. X. Wang, C. R. Thomas, Z. Zhang, *Chem. Eng. Sci.* **2009**, *64*, 821.

[98] C. Xin, L. Yang, J. Li, Y. Hu, D. Qian, S. Fan, K. Hu, Z. Cai, H. Wu, D. Wang, D. Wu, J. Chu, *Adv. Mater.* **2019**, *31*, 1.

[99] Y. Wang, W. Niu, S. Zhang, B. Ju, *J. Mater. Sci.* **2020**, *55*, 817.

[100] H. Saito, Y. Takeoka, M. Watanabe, *Chem. Commun.* **2003**, *3*, 2126.

[101] D. Nakayama, Y. Takeoka, M. Watanabe, K. Kataoka, *Angew. Chemie* **2003**, *115*, 4329.

[102] K. Suzuki, H. Takanobu, K. Noya, H. Koike, H. L. Miura, *IEEE Int. Conf. Intell. Robot. Syst.* **2007**, 590.

[103] Y. Naoi, H. Yano, T. Sawada, T. Kanai, *Kobunshi Ronbunshu* **2015**, *72*, 582.

[104] R. Tenno, Y. Gunjima, M. Yoshii, H. Kitahata, J. Gorecki, N. J. Suematsu, S. Nakata, *J. Phys. Chem. B* **2018**, *122*, 2610.

[105] Y. Matsuda, N. J. Suematsu, H. Kitahata, Y. S. Ikura, S. Nakata, *Chem. Phys. Lett.* **2016**, *654*, 92.

[106] E. Kang, G. S. Jeong, Y. Y. Choi, K. H. Lee, A. Khademhosseini, S. H. Lee, *Nat. Mater.* **2011**, *10*, 877.

[107] M. Sato, Y. Ishii, *J. Appl. Phys.* **1989**, *66*, 983.

Appendix A
Flows at low Reynolds number

Introduction

In this appendix, the general properties of flow at low Reynolds numbers are discussed[1]. At sufficiently small Reynolds numbers, it is generally agreed that the magnitude of the force on rigid particles of arbitrary shape in a streaming flow of viscous fluid is directly proportional to both the fluid viscosity and the magnitude of the free stream velocity. This result follows from an elementary dimensional analysis of the equations of motion and boundary conditions. But dimensional arguments provide no information as to the relation between the directions of the stream velocity vector, **U**, and hydrodynamic force vector, **F**. These vectors are not generally parallel since the body is subjected to not only drag forces, parallel to the stream velocity but to lift forces as well, at right angles to the stream.

Any general relationship connecting the vector velocity and vector force must consider an orientation of the body concerning either the stream velocity vector in a streaming flow or the gravity force vector in the case of a settling particle.

The rotational motion of a particle is more complicated. If the body has certain well-defined symmetry properties, it may have a center of hydrodynamic stress. In the absence of external torques, such a body will attain a steady terminal motion in which it merely translates, without rotating, as it settles. Certain particles of skew shape, typically propeller-like bodies, fail to have such a point and may rotate as they settle in a gravitational field. If such particles are subjected to lift forces as well, a spiral downward motion may result. When the spinning particle can change its orientation relative to the direction of gravity, a wobbling motion may also occur.

For cases where the quasi-static form of the creeping motion equations are applicable, the hydrodynamic force and torque (about any origin *O*) are applied on a rigid particle of arbitrary shape, translating and spinning in a fluid at rest at infinity, are dependent

upon three fundamental second-rank tensors (dyadic), which are intrinsic geometrical properties of the body. These are

(a) A translation tensor **K** (termed resistance tensor in Brenner's first paper[2]; but later, more appropriately, the term resistance is reserved for all modes of hydrodynamic interaction). This dyadic is symmetric.

(b) A rotational tensor $\mathbf{\Omega}_o$ which depends on the location of the origin *O*. This dyadic is symmetric.

(c) A coupling tensor $\mathbf{C}_o$ which depends on the location of the origin *O*, and represents a coupling of the translational and rotational motions. In general, this dyadic is not symmetric.

A unique point exists for all bodies at which the coupling tensor is symmetric. This point is termed the center of reaction, *R*. If $\mathbf{C}_R = \mathbf{O}$ the point *R* may be determined a center of hydrodynamic stress. If such the center exists, the body falling under the influence of gravity will reach a steady-state of motion in which it translates without rotation.

When a rigid particle of arbitrary shape translates and rotates in a fluid the motion is inherently unsteady. However, when both the translational and rotational Reynolds numbers

$$N_{Re}^{(t)} = \frac{cU_o\rho}{\mu}, N_{Re}^{(r)} = \frac{c^2\omega\rho}{\mu} \tag{A.1}$$

are small, it is permissible to adopt the quasi-state form of the creeping motion equations,

$$-\nabla \boldsymbol{p} + \eta\nabla^2\boldsymbol{v} = 0, \nabla\cdot\boldsymbol{v} = 0. \tag{A.2}$$

In equation (A.1), *c* is a characteristic particle dimension; U_o is the maximum speed with which any point in the particle moves; and ω is the magnitude of the spin.

As it is primarily interested in the forces and moments resulting from motion alone, the pressure *p* in equation (A. 2) will be regarded as the dynamic, rather than total pressure. The effects of hydrostatic pressure are thereby temporarily ignored.

Let *O* be any point rigidly affixed to the particle and mean by $\mathbf{U}_o$ the instantaneous velocity of this point and by $\boldsymbol{\omega}$ the instantaneous angular velocity of the particles. Since $\boldsymbol{\omega}$ is a free vector that is displaced parallel to itself, O doesn't need to lie on the instantaneous axis

of rotation of the particle. Given the no-slip condition at the surface S_p of the particle, the instantaneous boundary condition at the particle surface is

$$\mathbf{v} = U_o + \boldsymbol{\omega} \times \mathbf{r_o} \text{ on } S_p \tag{A.3}$$

where $\mathbf{r}_o$ is the position vector of a point relative to an origin at O. As the fluid is at rest at infinity the boundary condition, there is

$$\mathbf{v} \to \mathbf{0} \text{ as } r_o \to \infty \tag{A.4}$$

The linearity of the equations of motion and boundary conditions enables to write

$$\mathbf{v} = \bar{\boldsymbol{v}}_o + \bar{\bar{\boldsymbol{v}}}_o \tag{A.5a}$$

$$p = \bar{p}_o + \bar{\bar{p}}_o \tag{A.5b}$$

where the single and double overbars refer, respectively, to translational and rotational fields satisfying the following differential equations and boundary conditions:

$$\boldsymbol{\nabla}^2 \bar{\boldsymbol{v}}_o = \frac{1}{\mu} \boldsymbol{\nabla} \bar{\boldsymbol{p}}_o \tag{A.6a}$$

$$\boldsymbol{\nabla} \cdot \bar{\boldsymbol{v}}_o = 0 \tag{A.6b}$$

$$\bar{\boldsymbol{v}}_o = \boldsymbol{U_o} \text{ on } S_p \tag{A.6c}$$

$$\bar{\boldsymbol{v}}_o \to \mathbf{0} \text{ as } \boldsymbol{r_o} \to \infty \tag{A.6d}$$

and

$$\boldsymbol{\nabla}^2 \bar{\bar{\boldsymbol{v}}}_o = \frac{1}{\mu} \boldsymbol{\nabla} \bar{\bar{\boldsymbol{p}}}_o \tag{A.7a}$$

$$\boldsymbol{\nabla} \cdot \bar{\bar{\boldsymbol{v}}}_o = 0 \tag{A.7b}$$

$$\bar{\bar{\boldsymbol{v}}}_{\boldsymbol{o}} = \boldsymbol{\omega} \times \boldsymbol{r}_{\boldsymbol{o}} \text{ on } S_p \tag{A.7c}$$

$$\bar{\bar{\boldsymbol{v}}}_{\boldsymbol{o}} \to \mathbf{0} \ as \ \boldsymbol{r}_{\boldsymbol{o}} \to \infty. \tag{A.7d}$$

The subscripts *O* on the velocity and pressure fields serve to remind that the separate translational and rotational fields, of which **v** and p in equation (A.5) are comprised, both depend on the location of *O* through the dependence of $\mathbf{U}_o$ on *O*. The translational field $(\bar{\boldsymbol{v}}_o, \bar{p}_o)$ depends on the location of *O* through the dependence of $\mathbf{U}_o$ on *O*. On the other hand, the rotational field $(\bar{\bar{\boldsymbol{v}}}_o, \bar{\bar{p}}_o)$ depends on the choice of *O* through the dependence of $\mathbf{r}_o$ on *O*.

The hydrodynamic forces exerted by the fluid on the particle under the individual translational and rotational motions are, respectively,

$$\bar{\boldsymbol{F}}_o = \int_{S_p}^{1} d\boldsymbol{S} \cdot \bar{\boldsymbol{\Pi}}_o \tag{A.8}$$

and

$$\bar{\bar{\boldsymbol{F}}}_o = \int_{S_p}^{1} d\boldsymbol{S} \cdot \bar{\bar{\boldsymbol{\Pi}}}_o \tag{A.8}$$

where $d\mathbf{S}$ is directed into the fluid and $\mathbf{\Pi}$ is the pressure tensor. For an incompressible Newtonian fluid, the pressure tensor, $\mathbf{\Pi}$, is given by

$$\mathbf{\Pi} = -p\mathbf{I} + \kappa(\boldsymbol{\nabla} \cdot \boldsymbol{v})\mathbf{I} + 2\mu\Delta \tag{A.9}$$

where $\mathbf{I}$ is a unit tensor δ_{jk}, κ is a bulk or volume viscosity, $\mathbf{\Delta}$ is a rate of deformation tensor, defined as

$$\Delta = \frac{1}{2}[\boldsymbol{\nabla v} + (\boldsymbol{\nabla v})^t] - \frac{1}{3}\mathbf{I}(\boldsymbol{\nabla} \cdot \boldsymbol{v}) \tag{A.10}$$

where $(\boldsymbol{\nabla v})^t$ is the transpose or conjugate of $\boldsymbol{\nabla}\mathbf{v}$. By the Equations (A.9) and (A.10), the pressure tensor, $\mathbf{\Pi}$, can be rewritten as

$$\mathbf{\Pi} = -\mathbf{I}p + \mu[\boldsymbol{\nabla v} + (\boldsymbol{\nabla v})^t]. \tag{A.11}$$

The total force is subjected to the particle in consequence of its combined translational and

rotational motion is

$$\mathbf{F} = \bar{\mathbf{F}}_{\boldsymbol{o}} + \bar{\bar{\mathbf{F}}}_{\boldsymbol{o}}. \tag{A.12}$$

For a given rigid body motion, this force must be independent of the choice of *O*.

Similarly, the hydrodynamic torque about *O*, which the particle is subjected because of its individual translational and rotational motions, are, respectively,

$$\bar{\boldsymbol{T}}_o = \int_{S_p}^{1} \mathbf{r}_o \times (d\boldsymbol{S} \cdot \bar{\boldsymbol{\Pi}}_o) \tag{A.13}$$

and

$$\bar{\bar{\boldsymbol{T}}}_o = \int_{S_p}^{1} \mathbf{r}_{\boldsymbol{o}} \times \left(d\boldsymbol{S} \cdot \bar{\bar{\boldsymbol{\Pi}}}_o\right) \tag{A.14}$$

whereas the total torque about *O* is

$$\mathbf{T} = \bar{\mathbf{T}}_{\boldsymbol{o}} + \bar{\bar{\mathbf{T}}}_{\boldsymbol{o}}. \tag{A.15}$$

In contrast to **F**, this torque depends on the choice of *O*.

Translational motions

As results of the linearity of the translational equations of motion (A.6a-d), there exists a dyadic velocity field $\bar{\mathbf{V}} = \bar{\mathbf{V}}(\mathbf{r})$ (not symmetric in general) and a vector pressure field $\bar{\mathbf{P}} = \bar{\mathbf{P}}(\mathbf{r})$ concerning translational motions, it may be written

$$\bar{\boldsymbol{v}}_o = \bar{\mathbf{V}} \cdot \mathbf{U_o} \tag{A.16}$$

$$\bar{p}_o = \mu \bar{\mathbf{P}} \cdot \mathbf{U_o}. \tag{A.17}$$

At any point in the fluid, $(\bar{\mathbf{V}}, \bar{\mathbf{P}})$ are independent of the viscosity of the fluid, the location of *O*, and the magnitude and direction of $\mathbf{U}_o$. On the other hand, $(\bar{\mathbf{V}}, \bar{\mathbf{P}})$ depend only on the surface geometry of the particle and on the position vector of the fluid point under discussion relative to any origin fixed in the particle.

In addition, there exists a triadic stress field $\bar{\mathscr{P}} = \bar{\mathscr{P}}(\mathbf{r})$, defined by the relation

$$\bar{\bar{\mathbf{\Pi}}}_O = \mu \bar{\bar{\boldsymbol{p}}} \cdot \mathbf{U_o}. \tag{A.18}$$

This triadic field depends solely on the geometry of the particle. In consequence of equation (A.18), (A.8), and (A.13) may be written in the forms

$$\bar{\boldsymbol{F}}_o = \mu \int_{S_p}^{1} d\boldsymbol{S} \cdot \bar{\bar{\boldsymbol{p}}} \cdot \mathbf{U}_o \tag{A.19}$$

and

$$\bar{\boldsymbol{T}}_o = \mu \int_{S_p}^{1} \boldsymbol{r}_o \times (d\boldsymbol{S} \cdot \bar{\bar{\boldsymbol{p}}}) \cdot \mathbf{U}_{o.} \tag{A.20}$$

Thus, if the constant dyadic are defined as

$$\mathbf{K} = -\int_{S_p}^{1} d\boldsymbol{S} \cdot \bar{\bar{\boldsymbol{p}}} \tag{A.21}$$

and

$$\bar{\mathbf{C}}_o = -\int_{S_p}^{1} \boldsymbol{r}_o \times (d\boldsymbol{S} \cdot \bar{\bar{\boldsymbol{p}}}). \tag{A.22}$$

Equations (A.19) and (A.20) become

$$\bar{\boldsymbol{F}}_o = -\mu \mathbf{K} \cdot \mathbf{U_O} \tag{A.23}$$

and

$$\bar{\boldsymbol{T}}_o = -\mu \mathbf{C}_o \cdot \mathbf{U}_O. \tag{A.24}$$

It is reasonable to term **K** the translation tensor. It is an intrinsic geometric property of the body, dependent solely on its size and shape. In particular, it is independent of the orientation and velocity of the body and the fluid properties. It has the dimensions of length, and it uniquely characterizes the resistance of the body to translational motions at small Reynolds numbers.

Rotational motions

The rotational Stokes field, $(\bar{\bar{\boldsymbol{v}}}_o, \bar{\bar{p}}_o)$, satisfying Equations (A.7a-d), may be

expressed in the form

$$\bar{\bar{\boldsymbol{v}}}_o = \bar{\bar{\mathbf{V}}}_{\boldsymbol{o}} \cdot \boldsymbol{\omega} \tag{A.25}$$

$$\bar{\bar{p}}_o = \mu \bar{\bar{\mathbf{P}}}_{\boldsymbol{o}} \cdot \boldsymbol{\omega} \tag{A.26}$$

where the dyadic velocity field $\bar{\bar{\mathbf{V}}}_o = \bar{\bar{\mathbf{V}}}_o(\mathbf{r})$, and the vector pressure field $\bar{\bar{\mathbf{P}}}_o = \bar{\bar{\mathbf{P}}}_o(\mathbf{r})$ depend, at a given fluid point, only on the size and shape of the particle and the location of *O*.

It follows from equations (A. 11), (A.25), and (A.26) that the pressure tensor associated with the rotational motion can be expressed in the form

$$\bar{\bar{\mathbf{\Pi}}}_o = \mu \bar{\bar{\boldsymbol{\mathcal{P}}}}_{\boldsymbol{o}} \cdot \boldsymbol{\omega} \tag{A.27}$$

where, at a given fluid point, the stress triadic $\bar{\bar{\boldsymbol{\mathcal{P}}}}_o$ depends only on the geometry of the particle and the location of *O*. Hence, from equations (A.8) and (A.14), the force and torque on the particle arising from the rotational motion may be expressed in the forms

$$\bar{\bar{\mathbf{F}}}_o = -\mu \mathbf{D}_o \cdot \boldsymbol{\omega} \tag{A.28}$$

$$\bar{\bar{\mathbf{T}}}_o = -\mu \mathbf{\Omega}_{\boldsymbol{o}} \cdot \boldsymbol{\omega} \tag{A.29}$$

where

$$\mathbf{D}_o = -\int_{S_p}^{\mathbf{1}} d\mathbf{S} \cdot \bar{\bar{\boldsymbol{\mathcal{P}}}}_{\boldsymbol{o}} \tag{A.30}$$

$$\mathbf{\Omega}_o = -\int_{\boldsymbol{S_p}}^{\mathbf{1}} \mathbf{r}_{\boldsymbol{o}} \times (d\mathbf{S} \cdot \bar{\bar{\boldsymbol{\mathcal{P}}}}_{\boldsymbol{o}}). \tag{A.31}$$

The constant dyadic $\mathbf{D}_o$ and $\mathbf{\Omega}_o$ depend only on the size and shape of the particle and the location of *O*.

The dyadic $\mathbf{\Omega}_o$ is termed the rotation tensor at *O*. The dyadic $\mathbf{D}_o$ is equal to the transpose of the coupling tensor at *O*, and so is not an independent resistance parameter. The reciprocal theorem is applied in the form

$$\int_{S_p}^{1} \bar{\boldsymbol{v}}_o \cdot \bar{\bar{\boldsymbol{\Pi}}}_o \cdot d\mathbf{S} = \int_{S_p}^{1} \bar{\bar{\boldsymbol{v}}}_o \cdot \bar{\boldsymbol{\Pi}}_o \cdot d\mathbf{S}. \tag{A.32}$$

Given the boundary conditions (A.6c) and (A.7c), the symmetry of the pressure tensor, and the vector identity $\mathbf{a} \times \mathbf{b} \cdot \mathbf{c} = \mathbf{a} \cdot \mathbf{b} \times \mathbf{c}$, the equation (A.32) may be written in the form

$$\mathbf{U}_o \cdot \int_{S_p}^{1} d\mathbf{S} \cdot \bar{\bar{\boldsymbol{\Pi}}}_o = \boldsymbol{\omega} \cdot \int_{S_p}^{1} \mathbf{r}_o \times (d\mathbf{S} \cdot \bar{\boldsymbol{\Pi}}_0). \tag{A.33}$$

Utilizing equations (A.8) and (A.13) this becomes

$$\mathbf{U}_o \cdot \bar{\bar{\mathbf{F}}}_o = \boldsymbol{\omega} \cdot \bar{\mathbf{T}}_o. \tag{A.34}$$

Hence, substituting equations (A.28) and (A.24) into the preceding, the followed form is obtained

$$\mathbf{U}_o \cdot \mathbf{D}_o \cdot \boldsymbol{\omega} = \boldsymbol{\omega} \cdot \mathbf{C}_o \cdot \mathbf{U}_o. \tag{A.35}$$

However, from the definition of the transpose of a dyadic, it follows that

$$\boldsymbol{\omega} \cdot \mathbf{C}_o \cdot \mathbf{U}_o = \mathbf{U}_o \cdot \mathbf{C}_o^t \cdot \boldsymbol{\omega}. \tag{A.36}$$

By equations (A.35) and (A.36), the following relationship is obtained as

$$\mathbf{D}_o = \mathbf{C}_o^t. \tag{A.37}$$

Thus, from equation (A.28), the hydrodynamic force is subjected to a particle rotating about any axis through *O* is

$$\bar{\bar{\mathbf{F}}}_o = -\mu \mathbf{C}_o^t \cdot \boldsymbol{\omega}. \tag{A.38}$$

Combined Translation and Rotation

Return to the general case where the particle may simultaneously translate and rotate. In this case, the force on the body, given by equations (A.12), and the torque about *O*, given by equations (A.15), maybe written as

$$\mathbf{F} = -\mu \mathbf{K} \cdot \mathbf{U}_o - \mu \mathbf{C}_O^t \cdot \boldsymbol{\omega} \tag{A.39}$$

$$\mathbf{T} = -\mu \mathbf{C_o} \cdot \mathbf{U}_o - \mu \boldsymbol{\Omega}_o \cdot \boldsymbol{\omega} \tag{A.40}$$

Therefore, the equations (A.39) and (A.40) may be written in terms of partitioned matrices as follows:

$$\begin{pmatrix} (\mathbf{F}) \\ (\mathbf{T}_o) \end{pmatrix} = -\mu \begin{pmatrix} (\mathbf{K}) & (\mathbf{C}_o)^t \\ (\mathbf{C}_o) & (\boldsymbol{\Omega}_o) \end{pmatrix} \begin{pmatrix} (\mathbf{U}_o) \\ (\boldsymbol{\omega}) \end{pmatrix}. \tag{A.40}$$

Appendix B
Magnetic actuation principles

Characteristics of Superparamagnetic material

Superparamagnetic materials are ferromagnetic bodies in which the particle size is so small that only a single magnetic domain exists inside the particle and the internal magnetic dipole can be regarded as a single[3]. The magnetic fluid used in this study is a colloidal solution of dispersed nanoscale magnetic materials, which are considered superparamagnetic materials. When a magnetic field is applied externally to a superparamagnetic material, it is magnetized in the direction of the applied field. The superparamagnetic material magnetized by a magnetic field has no residual magnetization and no hysteresis when the magnetic field is removed. In the absence of the external magnetic field, the magnetic anisotropy energy gradually decreases as the size of the particles decreases. Eventually, the thermal energy within the particle overcomes the magnetic anisotropic energy, and the magnetic moment is free to change direction within the particle. This phenomenon is called Neel rotation. Therefore, the magnetization of the entire particle is zero on average under no magnetic field. The relaxation time of the particle due to Neel rotation, τ_N, is expressed as

$$\tau_N = f_0^{-1} exp\left(\frac{KV}{k_B T}\right), \tag{B.1}$$

where k_B is a Boltzmann constant, T is an absolute temperature, f_0 is a Larmor frequency, K is a Magnetic anisotropy constant, and V is an actual volume of particles without surface layers such as surfactants. The Lamor frequency, f_0, is approximately 10^9 1/s. The magnetic anisotropy constant of Fe, K, is 4.2×10^4 J/m^3, thus the relaxation time, τ_N, is calculated as 228×10^{-9} s when the diameter of particle is 10 nm at 293.15 K. This result suggests that the time required for the magnetic moment of the magnetic particles to orient to the magnetic field is also fast.

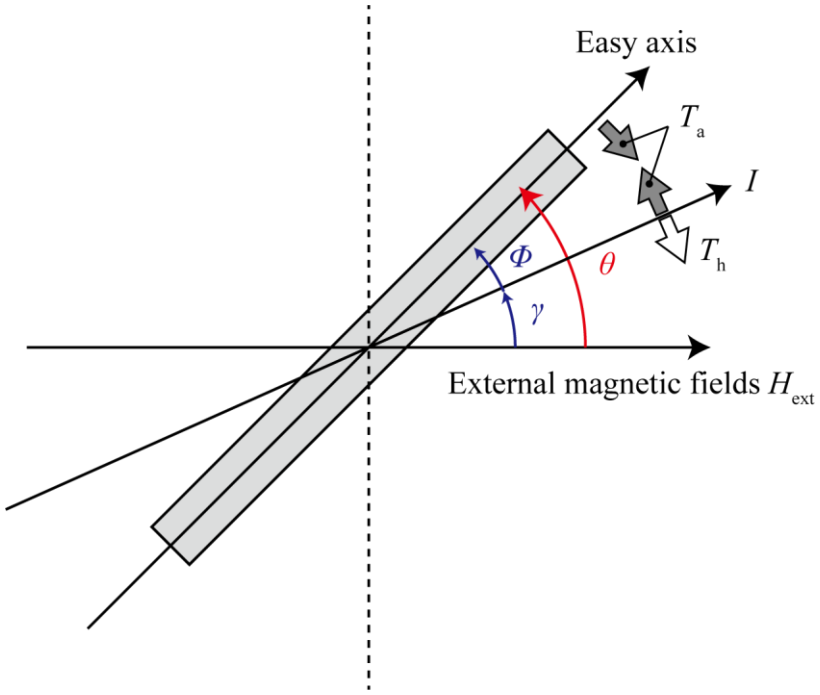

Figure B.1 Shape anisotropy of magnetic body.

Shape anisotropy

For considering the magnetic actuation principles, spiral-shaped micro-swimmers are assumed as a single soft magnetic body[4]. The magnetization changes during the rotation of the micro-swimmer, and the rotational torque changes accordingly. It is assumed that the magnetization of a magnetic body is proportional to the magnetic field and that the magnetization does not saturate. Based on the above assumption, the change in magnetization and the change in rotational torque are theoretically derived. The cylindrical element of a spiral micro-swimmer is considered. When an external magnetic field is applied to a magnetic body, magnetization I is generated inside the magnetic body. This magnetization generates an antimagnetic field H_d in the direction opposite to the external magnetic field. The antimagnetic field is written as

$$H_d = N\frac{1}{\mu_0} \tag{B.2}$$

where μ_0 is the permeability of the vacuum and N is a diamagnetic field coefficient which is dependent on the shape of the magnetic body. Magnetostatic energy is written as

$$U = \frac{1}{2\mu_0} N I^2 V_{mag} \tag{B.3}$$

where V_{mag} is the volume of the magnetic body. Thus, the magnetostatic energy is also dependent on the shape of the magnetic body and this tendency is called shape anisotropy. The demagnetizing factor is small in the longitudinal direction and large in the shortitudinal direction of the magnetic body. The magnetic field which is needed to magnetize the magnetic body is increased as the diamagnetic field increase. The longitudinal direction is called the easy magnetization axis, and the shortitudinal direction is called the hard magnetization axis. When the magnetization I deviate θ from the easy magnetization axis (Fig. B.1), the magnetostatic energy is changed as

$$U = \frac{1}{2\mu_0} I^2 V_{mag} \left(N_a \cos^2 \theta + N_b \sin^2 \theta \right) \tag{B.4}$$

where N_a and N_b are demagnetizing factors of the easy magnetization axis and hard magnetization axis, respectively. A magnetic anisotropy torque T_a works to align the magnetization direction of the magnetic material with the easy axis of magnetization in the form

$$T_a = -\frac{\partial U}{\partial \theta} = \frac{1}{2\mu_0} I^2 V_{mag} (N_b - N_a) \sin 2\theta. \tag{B.5}$$

Next, the demagnetizing factors of the cylindrical element are described based on the previous research[107]. The cylindrical element with radius r and length $2nr$ was considered. To obtain the demagnetizing factor of this cylindrical element, the cylindrical element is replaced by a rectangular rod with the area of cross-section equal to that of the cylindrical element. The demagnetizing factors of the rectangular rod are written as

$$N_a = N_b = \left(\frac{2n}{\sqrt{\pi}}\right) / \left[2\left(\frac{2n}{\sqrt{\pi}}\right) + 1\right]. \tag{B.6}$$

When the magnetization I is placed in an external magnetic field H_{ext}, a torque T_h is generated in the form

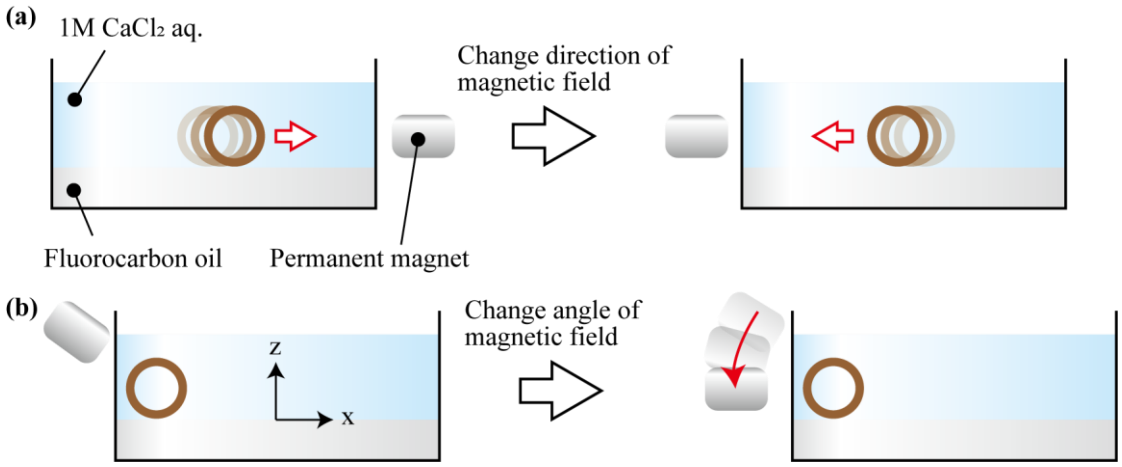

Figure B.2 Schematic images of applied magnetic fields. (a) Change direction. (b) Change angle.

$$T_h = V_{mag} I \times H_{ext} = V_{mag} I H_{ext} \sin\gamma. \quad \text{(B.7)}$$

The torque acting on the magnetization is balanced to the magnetic anisotropy torque such as

$$T_a = T_h. \quad \text{(B.8)}$$

It is assumed that the magnitude of the magnetization I is proportional to the magnetic field H, I is written as

$$I = \chi H \quad \text{(B.9)}$$

where χ is a magnetic susceptibility. In this Equation (B.9), H is the magnetic field penetrating the inside of the magnetic body, which is different from H_{ext}. It needs to consider the direction of the magnetic field and the diamagnetic field due to magnetization. Thus, H is written as

$$H = H_{ext} \cos\gamma - H_d. \quad \text{(B.10)}$$

The energy of the diamagnetic field is written as

Appendix B

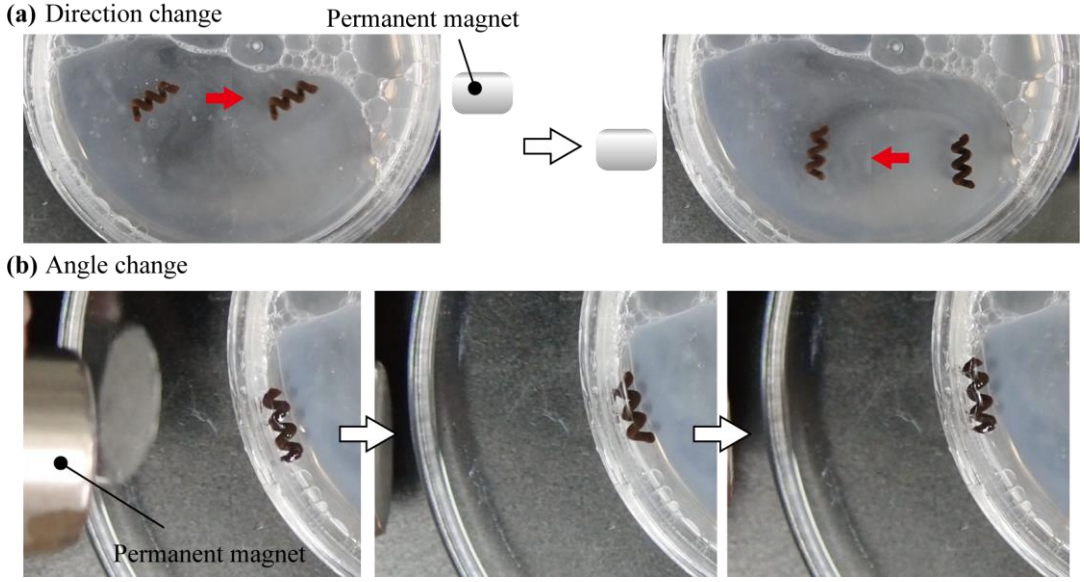

Figure B.3 Results of applied magnetic fields. (a) Change direction. (b) Change angle.

$$U = \frac{1}{2\mu_0} NI^2 = \frac{1}{2\mu_0} (N_b (I sin\phi)^2 + N_b (I cos\phi)^2), \tag{B.11}$$

and demagnetizing factor N is determined as

$$N = N_b sin^2\phi + N_a cos^2\phi. \tag{B.12}$$

Therefore, the magnetization I is written as

$$I = \frac{\chi\mu_0}{\mu_0 + \chi(N_b sin^2\phi + N_a cos^2\phi)} H_{ext} cos\gamma. \tag{B.13}$$

Experiments

To observe the shape anisotropy of micro-swimmers, the magnetic fields were applied in various directions and angles. To form the micro-swimmer, Magnetic nanoparticles (10.2% (v/v) encapsulated 2% (w/w) NaAlg. and 1 M $CaCl_2$ solution was used. The fabricated micro-swimmer was placed into the 1 M CaCl2 solution, and the fluorocarbon oil was used for decreasing friction with the bottom of the chamber. The magnetic field was applied by using the permanent magnet.

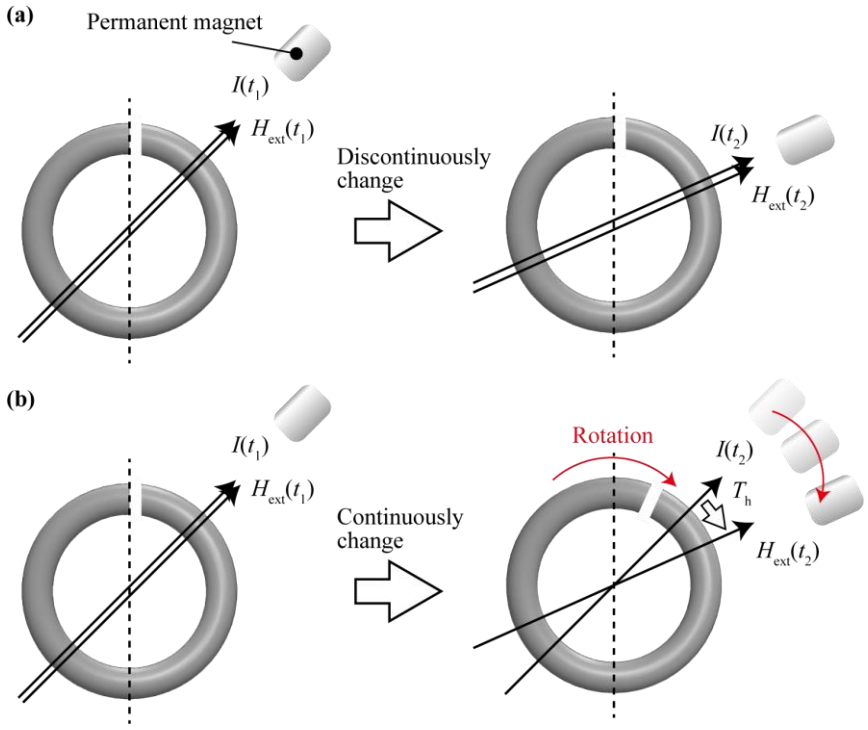

Figure B.4 Rotation mechanism of micro-swimmer. (a) discontinuously changed. (b) continuously changed.

Results and Discussion

When the magnetic field was applied from the right direction, the micro-swimmer was attracted to the permanent magnet without changing its posture (Fig. B.3 (a) left). The micro-swimmer was also attracted to the permanent magnet without changing its posture when the magnetic field was applied from the left direction (Fig. B.3 (a) right). In addition, when the posture of the micro-swimmer before the applying the magnetic field was changed, the micro-swimmer was attracted to the permanent magnet without changing its posture as well. These results indicated that the shape anisotropy of the micro-swimmer was not strong enough to rotate the micro-swimmer.

On the other hand, when rotating the magnetic field, the micro-swimmer rotated responding to the permanent magnet (Fig. B.3 (b)). This result shows that the torque expressed by the equation (B.7) was applied on the micro-swimmer.

Above these results, it is indicated that the torque caused by the magnetic field and magnetization was the main driving force of the micro-swimmer. Previous research was also considered only the torque as the driving force[39].

Based on the theories and results, the mechanism of the rotation of the micro-swimmer was discussed. The magnetic domains of the magnetic nanoparticles in the micro-swimmer are randomly oriented and cancel each other out when the magnetic field was not applied. When the magnetic field is applied, the magnetization of the micro-swimmer is directed in the direction of the applied magnetic field. When the magnetic field was removed, the magnetization was relaxed by the Neel rotation of magnetic nanoparticles. So, when the direction of the applied magnetic field was discontinuously changed, the direction of magnetization is also discontinuously changed to the direction of the applied magnetic field, and no torque is generated (Fig. B.4 (a)). When the magnetic field was continuously applied, the magnetization of micro-swimmer was also continuously changed (Fig. B.4 (b)). However, the magnetization changes in response to the changing of the magnetic field, so a time difference is slightly expected to occur. It is believed that this time difference will always generate torque in the micro-swimmer, which will propel it to rotate.

Appendix C
Frequency-dependent behavior

Principle

At a given magnetic field strength, the velocity of the spiral-shaped micro-swimmer is a function of frequency of the applied fields (see equation (3.6)). The linear relationship between velocity u and the frequency ω in equation (3.6) is only valid while the magnetic torque is large enough to sustain the rotation of the micro-swimmer at the frequency ω[5]. The drag on the micro-swimmer increase with ω and the maximum frequency referred to as step-out frequency is given by the maximum magnetic torque:

$$\omega_{max} = \frac{a}{ac - b^2} T_{max}. \qquad \text{(C.1)}$$

If the magnetic field is rotated at a frequency higher than ω_m, the micro-swimmer cannot more in-sync with the field anymore and the velocity drops. From equation (B.7) it is clear that the maximum T_{max} is a function of the applied magnetic field strength, the magnetization, and the size of the magnetic material on the swimmer.

Experiment

For determining the frequency of applied rotational magnetic fields f_{mag}, the frequency-dependent behavior of micro-swimmers was observed (f_{mag} = 1, 5, 7.5, 10 Hz). For comparing the behavior of micro-swimmer applied magnetic fields, the average rotational speed ω and the average frequency of micro-swimmer f_{swim} were measured. In addition, the following rate $\varepsilon = f_{swim}/f_{mag}$ is calculated.

When applying the rotational magnetic fields with f_{mag} = 5 Hz, the results of Chapter 3.4 were used. When applied f_{mag} = 1 Hz, the strength of magnetic fields is 20 mT. The 1M CaCl2 + 0.75 % (w/w) PGAlg. Was used for surrounding environments. The inside pattern spiral-shaped micro-swimmer was used. To form the inside pattern spiral-shaped micro-

Table C.1 Comparing the frequencies.

	Frequency of applied magnetic field f_{mag} [Hz]			
	1	5	7.5	10
ω [rad/s]	1.30 (Discontinuous)	7.17	0.71	0.82
f_{swim} [Hz]	0.21 (Discontinuous)	1.14	0.11	0.13
ε [-]	0.21	0.23	0.01	0.01

swimmer, 4.5% (w/w) magnetic nanoparticles encapsulated 2.6%(w/w) p(NIPAM-co-AAc) + 0.4% (w/w) NaAlg as a stimuli-responsive layer, and 3% (v/v) fluorescent microbeads encapsulated 1.0% (w/w) NaAlg + 1.0% (w/w) PGAlg as a non-responsive layer were used. When applied f_{mag} = 7.5 Hz, the strength of magnetic fields is 16 mT. The 1M $CaCl_2$ + 1 g/mL sucrose solution was used for surrounding environments. To form the spiral-shaped micro-swimmer, 8.0 % (v/v) magnetic nanoparticles encapsulated 3% (w/w) NaAlg. and 2 M $CaCl_2$ solution were used. When applied f_{mag} = 10 Hz, the strength of magnetic fields is 12 mT. The 1M $CaCl_2$ + 1 g/mL sucrose solution was used for surrounding environments. To form the spiral-shaped micro-swimmer, 5.3 % (v/v) magnetic nanoparticles encapsulated 3% (w/w) NaAlg. and 2 M $CaCl_2$ solution were used.

Results and discussion

The measured rotational speeds and the frequencies micro-swimmer were summarized in Table C.1. The micro-swimmer could not follow any frequency of rotational magnetic fields. These results showed that the applied torque is very small. It is considered that the magnetization of micro-swimmer is much smaller than the previous research because the previous research used the permanent magnet or deposited metals.

When applied rotational magnetic fields with f_{mag} = 5, 7.5, 10 Hz, the micro-swimmer was continuously rotated. On the other hand, the micro-swimmer was discontinuously rotated when applied rotational magnetic fields with f_{mag} = 1 Hz. The following rate of 1 Hz was similar to the following rate of 5 Hz, thus it is considered that the

discontinuous motion is due to slow rotation speed and stalling. When the frequencies were 7.5 and 10 Hz, the following rates were very small (ε = 0.01). This tendency of decreasing the following rate is similar to the previous work[39].

Above these results, it is revealed that the spiral-shaped micro-swimmer could not follow the applied rotational magnetic fields with 1-10 Hz. It is estimated that the applied torque was very weak because the magnetization of magnetic nanoparticles was much smaller than the previous research (permanent magnet or deposited metal). In this study, 5 Hz was used because of the continuous motion with a high follow rate.

Appendix D
Detail analysis of deformation

In this appendix, the deformation of spiral-shaped micro-swimmer with different initial pith angles and the patterning angle was described. The initial pitch angle, α_i, and the patterning angle, θ, was changed for analyzing the deformation behavior (α_i = 20-70º, θ = 0-330º).

First, it is mentioned that the deformation behavior when changing the patterning angle, θ (Fig. D.1 (a)). The expansion behavior was observed between θ = 120º and θ = 240º. When the patterning angle, θ = 0, 30, 60, 300, 330º, the amount of deformation was limited

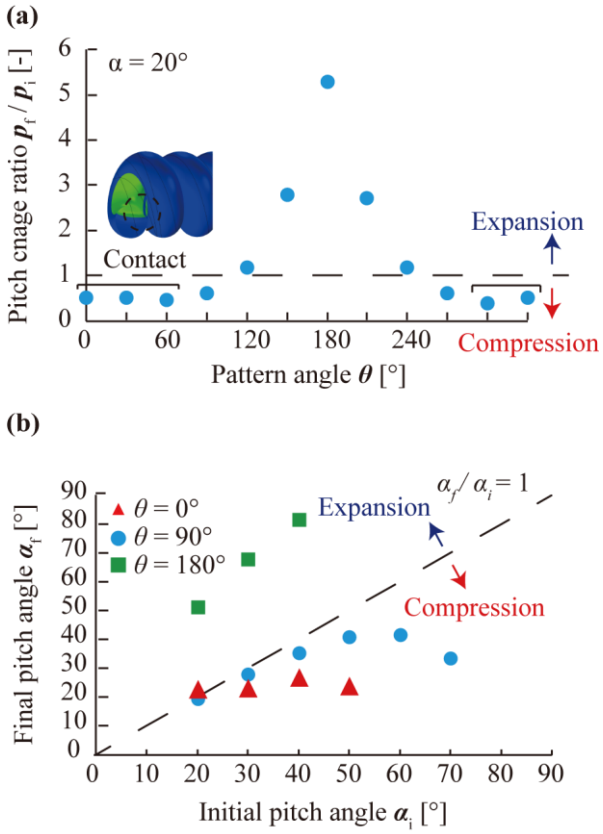

Figure D.1 Detail simulations. (a) the patterning angle. (b) Initial pitch angle.

by the contact of the hydrogel. These simulation results show that the deformation behavior and the amount of deformation were depending on the patterning angle, θ.

Then, the influence of the pitch angle, α, was mentioned (Fig. D.1 (b)). When the patterning angle, $\theta = 0^{o}$, the final pitch angle, α_f, was nearly the same value ($\alpha_f = 20^{o}$), because the amount of deformation was limited by the contact of the hydrogel. When the patterning angle, $\theta = 90^{o}$, the amount of deformation was increased as increasing the initial pitch angle, α_i. On the other hand, when the patterning angle, $\theta = 180^{o}$, the double-layered spiral-shaped hydrogel was only expanded, and the amount of deformation was also increased as increasing the initial pitch angle, α_i. These results indicated that the amount of deformation was increased as the initial pitch angle, α_i if the deformation is not inhibited by contacting the hydrogel. Moreover, it is indicated that the direction of deformation is not depending on the initial pitch angle, α_i.

Appendix E
Response speed of stimuli-responsive hydrogel

Experiments

In this Appendix, a response speed of single-layered spiral-shaped hydrogel and a vertical pattern spiral-shaped hydrogel were compared. To form the single-layered spiral-shaped hydrogel, 2.6%(w/w) p(NIPAm-co-AAc) + 0.4%(w/w) NaAlg was extruded at constant flow (4.72×10^{-3} m/s) into a 1 M $CaCl_2$ solution via the bevel-tip capillary (300 μm, 20°). To form the vertical patterned spiral-shaped hydrogel, a double-layer laminar flow by using 2.6 %(w/w) p(NIPAm-co-AAc) + 0.4 %(w/w) NaAlg as a stimuli-responsive layer, and 1.5% (w/w) NaAlg + 1.5% (w/w) PGAlg as a non-responsive layer was extruded into a 1 M $CaCl_2$ solution via the bevel-tip capillary (200 μm, 20°).

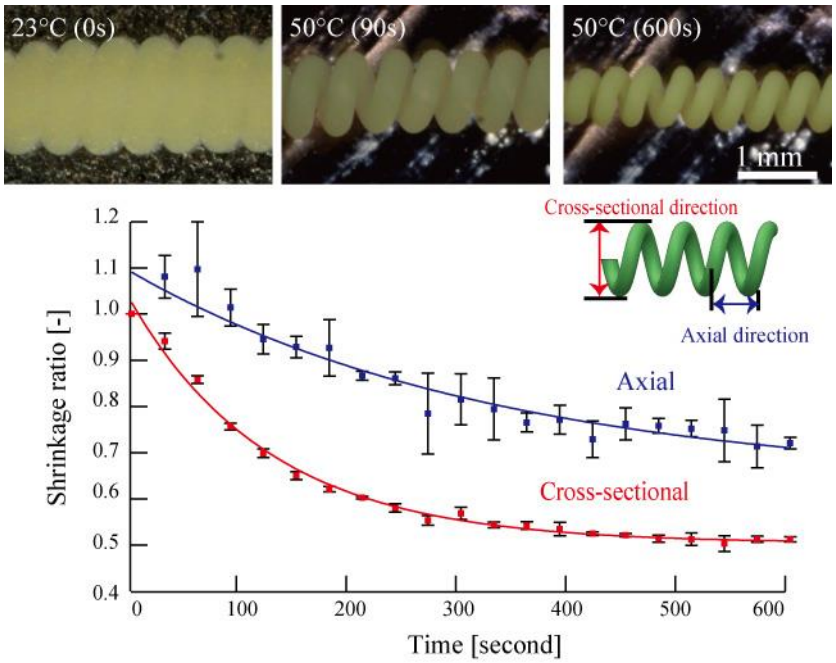

Figure E.1 Thermal responsiveness of single-layered spiral-shaped hydrogel.

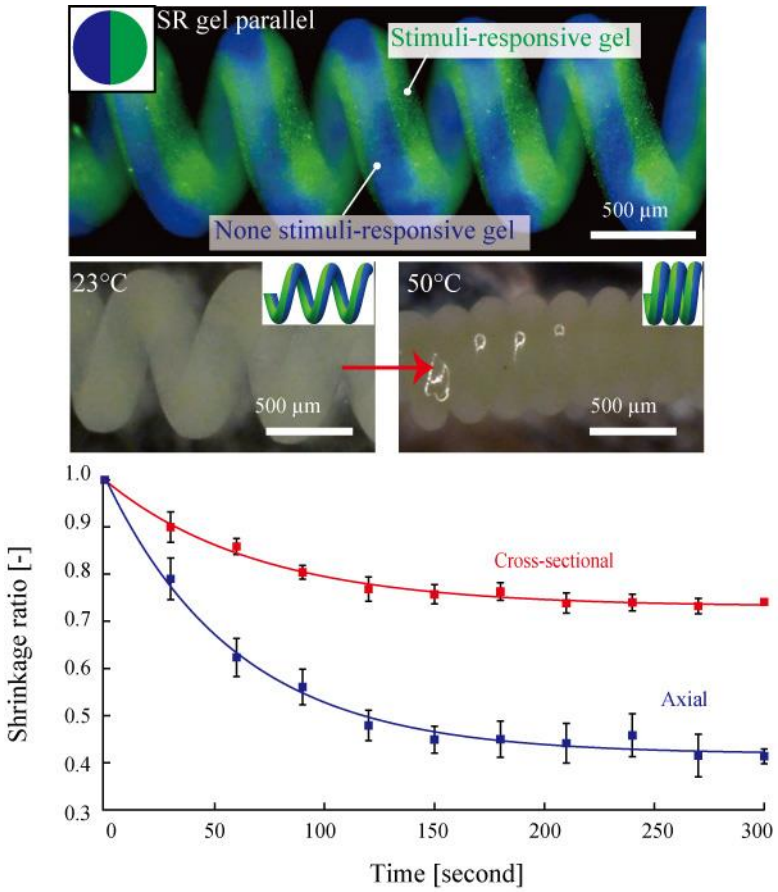

Figure E.2 Thermal responsiveness of vertical patterned spiral-shaped hydrogel.

The fabricated spiral-shaped hydrogels were heated by 50°C 1M $CaCl_2$ solution. The shrinking ratio of axial direction r_{axis} and cross-sectional direction r_{cross} were measured every 30 seconds for 600 seconds. Based on the measured shrinking ratio, a time constant was calculated by using analyzing software (IGOR Pro, WaveMatrics).

Results and discussions

The shrinking of single-layered spiral-shaped hydrogel was converged in about 300 s (Fig. E.1). The shrinking ratio of each direction were $r_{axis} = 0.5$ and $r_{cross} = 0.7$, respectively. The time constants were $\tau_{axis} = 339$ and $\tau_{cross} = 329$. These results showed that the stimuli-responsive hydrogel was isotropically shrunk regardless of their shape.

On the other hand, the shrinking of vertical patterned spiral-shaped hydrogels was converged in about 150 s (Fig. E.2). These results showed that the response speed depends on the diameter of stimuli-responsive hydrogels, and this tendency is similar to the equation (2.22). The shrinking ratio of each direction were $r_{axis} = 0.8$ and $r_{cross} = 0.4$, respectively. The time constants were $\tau_{axis} = 60$ and $\tau_{cross} = 58$. These results indicated that the response time of spiral-shaped hydrogel is not affected by compartmentalization.

Above those results, the miniaturized spiral-shaped hydrogel is effective for realizing high-speed soft actuators and the compartmentalization of spiral-shaped hydrogel does not need to be considered to improve response time at scale.

Appendix F
Electric double layer

Introduction

In this Appendix, an electric double layer of silica particle is described[6]. Hydrogen ions dissociate from the SiO_2 surface, and the surface becomes negatively charged. When the infinity point of the bulk solution is the reference point of the potential, the potential at the surface is called the surface potential and is denoted by φ_0. It is considered that the case where ions on the surface of a particle are charged by reaching an equilibrium state with ions in the solution. The followed reaction is occurred by hydration of SiO_2 surface with water:

$$Si\text{-}OH + OH^- \rightarrow Si\text{-}O^- + H_2O. \quad (F.1)$$

Although the surface potential φ_0 can be calculated by theoretically determining the dissociation constant of ions from the surface of a material, in practice it is difficult to accurately determine φ_0 due to the various ions and molecules attached to the surface. Therefore, it is common in the field of interfacial electrochemistry and colloid chemistry to measure the surface potential and calculate it as the potential of the surface. This measured value is called the zeta potential and is denoted by ξ (Fig. F.1 (a)). The surface potential φ_0 and the zeta potential ξ can be regarded as almost the same value and distinguished in the sense of a conceptual value and a measured value. The zeta potential depends on the concentration C_d of the potential-determining ions in the solution. In the case of SiO_2 surface, it depends on the concentration of H^+, according to the above chemical equation (F.1). When the charged surface is in a solution, oppositely charged ions gather near the surface to form an ionic layer. This layer is called an electric double layer. Since the zeta potential is determined by the equilibrium reaction of ions between the surface and the solution, it is determined only by the potential-determining ions that react with the surface (H^+ ions in the case of SiO_2). However, the electric double layer involves all ions of opposite sign to the

Appendix F

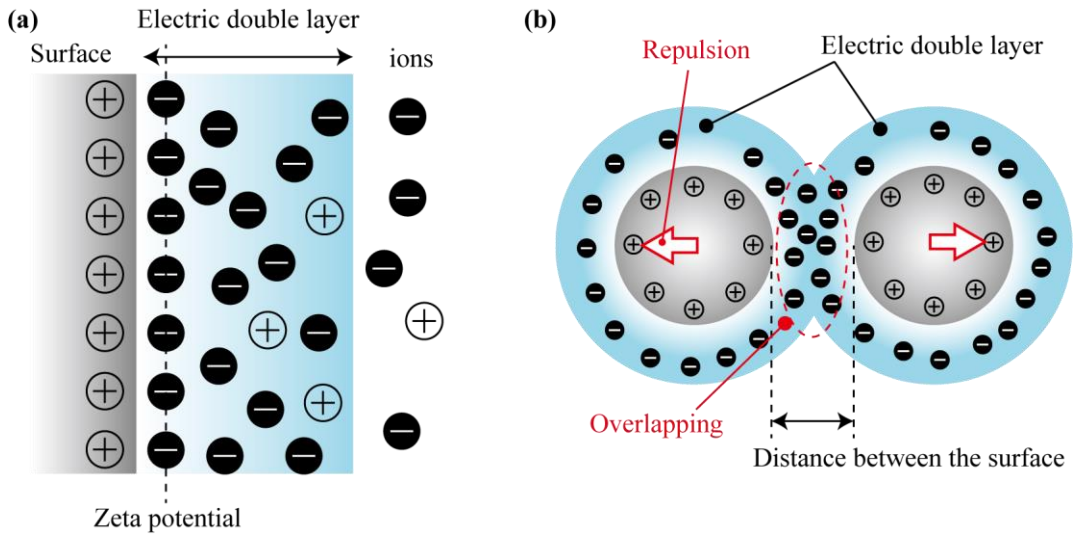

Figure F.1 (a) The schematic image of zeta potential. (b) The schematic image of electric repulsion.

surface charge. These oppositely charged ions are called counterions and denote their concentration by *C*. The ion distribution in the electric double layer can be derived from the chemical potential and the Poisson-Boltzmann (PB) equation as

$$\rho_x = \rho_0 e^{\left(-\frac{ze\varphi}{kT}\right)} = \frac{\rho_0}{(cosKx)^2} \tag{F.2}$$

where

$$K^2 = \frac{(ze)^2 \rho_0}{2\varepsilon\varepsilon_0 kT}, \tag{F.3}$$

and φ is the electric potential and ρ is the number density of ions of valence z at any point x between the two surfaces[7]. x = 0 is the midpoint between the surfaces. K is Boltzmann's constant, T is the absolute temperature, e is the elementary charge, ε_0 is the dielectric constant of the vacuum, and ε is the relative dielectric constant.

Interaction between the surfaces

Next, it is described how to calculate the interaction between the surfaces. In solutions, interactions such as electrostatic interaction, Van der Waals (VDW) interaction, structural force, depletion interaction, rigid sphere repulsion, and hydrophobic interaction

occur between surfaces and particles in a complex manner depending on the surface condition and the nature of the solution. Some of them are described in the form of potentials, which allow us to theoretically calculate the interaction between surfaces in solutions. For example, there is the Lennard-Joes potential, which deals with intermolecular interactions and rigid sphere repulsion, and the Derjaguin-Landau-Verwey-Overbeek (DLVO) potential, which deals with electrostatic interactions and van der Waals interactions. In this study, the potential interactions related to the interaction between micro-particles are electrostatic and van der Waals, from the point of view of micro-scale.

Van der Waals interaction

There are three types of van der Waals forces (VDW forces): dispersion forces, orientation forces, and induced forces. Dispersion forces are mainly dominant for bulk individuals such as between particles or planes. The VDW force acts as an attractive force, and its strength is determined by the Hamaker constant *A*, which is a material-specific eigenvalue. When the two surfaces are considered as parallel plates, the VDW potential is determined as

$$V_A = -\frac{A}{48\pi d^2} \tag{F.4}$$

where *d* is the distance between the surface. By differentiating with distance*d*, a force FA due to VDW interaction acting between surfaces is calculated as

$$F_A = \frac{dV_A}{dd} = \frac{A}{24\pi d^2}. \tag{F.5}$$

Electric double layer repulsion

When surfaces covered with the electric double layer approach each other, electrostatic interactions act between the surfaces (Fig. F.1 (b)). Especially in the case of electric double layers of the same charge, electrostatic repulsion is generated, which is called electric double layer repulsion. This repulsive force is expressed in terms of the potential V_R as a function of the distance d between the surfaces as

$$V_R = \frac{0.048\sqrt{C}}{z}\gamma^2 e^{-2\kappa d} \tag{F.6}$$

where

$$\gamma = \frac{e^{ze\xi/2kT} - 1}{e^{ze\xi/2kT} + 1} \tag{F.7}$$

$$\kappa = \left(\frac{2000z^2e^2CN_A}{\varepsilon_r\varepsilon_0 kT}\right)^{\frac{1}{2}}. \tag{F.8}$$

The counterion concentration is C [mol/L], the distance between the surfaces is d [m], the valence is z, the zeta potential is ξ [mV], and the temperature is T [K]. The potential V_R due to electric double layer repulsion depends on the zeta potential ξ of the particle surface and the counterion concentration C. The force F_R per unit area due to the electric double layer is obtained by differentiating this potential by the distance d in the form

$$F_R = \frac{dV_R}{dd} = \frac{-0.096\sqrt{C}}{z}\gamma^2\kappa e^{-2\kappa d}. \tag{F.9}$$

Derjaguin-Landau-Verwey-Overbeek potential

The Derjaguin-Landau-Verwey-Overbeek (DLVO) potential is a combined potential of the VDW potential and the electric double layer repulsion potential, which is used to describe the dispersion and aggregation of colloidal particles. When the VDW force acts as an attraction and the electric double layer acts as repulsion between colloidal particles, the balance between these two potentials can describe the state of dispersion and aggregation of colloidal particles. The DLVO potential V_{DLVO} is expressed as the sum of the VDW potential V_A and the electric double layer potential V_R in the form

$$V_{DLVO} = V_A + V_R. \tag{F.10}$$

Although the VDW potential V_A is constant depending on the substance, whether the DLVO potential V_{DLVO} becomes attractive or repulsive is determined by the ion concentration because the electric double layer potential V_R changes depending on the ion concentration of the solution.

The expansion of the electric double layer

Next, the expansion of the electric double layer by desalting is mentioned[8]. When an ion exchange resin is added to a colloidal solution for desalting the solution, the electric double layer formed by the particles expands. The thickness of the electric double layer is given by κ^{-1}. The repulsion due to the superposition of the electric double works, so that the particle of diameter D behaves as if it were a sphere of effective diameter $D_{eff}=D+2\kappa^{-1}$. An ion-exchange resin before use absorbs H^+ and OH^-. When the resin is dispersed in the colloidal solution, the resin adsorbs the ions dispersed in the solution and releases the H^+ and OH^- that were originally adsorbed. Since the released H^+ and OH^- combine to form H_2O, the concentration of ions in the colloidal solution decreases. In a well-desalted system, there is only $[H^+]=[OH^-]=10^{-7}$ mol/L due to water ionization, so the thickness of the electric double-layered is determined by the Equation (F.8) as κ^{-1}~955 nm (z =1, e = 1.60×10^{-19} C, C = 10^{-7} mol/L, N_A = 6.02×10^{23} 1/mol, ε_r = 78.5 (water, 25°C), ε_0 = 8.85×10^{-12} F/m, k = 1.38×10^{-23} J/K, T = 293.15 K (25°C)). Therefore, a silica particle with a diameter of 130 nm can theoretically expand its effective diameter to 2040 nm.

Appendix G
Summary of license numbers

The license numbers for the figures in this paper were summarized in Table G.1.

Table G.1 Summary of license numbers

Figure number	License numbers
Figure 1.2 (I-i)	5046231510871
Figure 1.2 (I-ii)	1111077
Figure 1.2 (I-iii)	5046260130014
Figure 1.2 (II-i)	5046260434274
Figure 1.2 (II-ii) left	Permission is not required
Figure 1.2 (II-ii) right	5046260960022

Appendix H
References of Appendix

[1] J. Happel, H. Brenner, “Low Reynolds number hydrodynamics”, Noordhoff International Publishing, Leyden 1983.

[2] H. Brenner, *Chem. Eng. Sci.* **1963**, *18*, 1.

[3] 山口博司, “磁性流体”, 森北出版株式会社, 2011.

[4] 近角聡信, “強磁性体の物理　下”, 裳華房, 1978.

[5] K. E. Peyer, L. Zhang, B. J. Nelson, Nanoscale 2013, 5, 1259.

[6] 北原文雄, 古澤邦夫, 尾崎正孝, 大島広行, “ゼータ電位 第 3 版”, サイエンティスト社, 2012.

[7] J. N. イスラエルアチヴィリ, “分子間力と表面力 第 3 版”, 朝倉出版, 2013.

[8] 北原文雄, 古澤邦夫, 金子克美, “コロイド科学 I”, 東京化学同人, 1995.